DEVELOPMENT OF THE POLARIZED MONTE CARLO THREE DIMENSIONAL RADIATIVE TRANSFER MODEL I3RC-POL

BY

ALLISON NICOLE HOUGHTON

THESIS

Submitted in partial fulfillment of the requirements
for the degree of Master of Science in Atmospheric Sciences
in the Graduate College of the
University of Illinois at Urbana-Champaign, 2014

Urbana, Illinois

Adviser:

Professor Larry Di Girolamo

Abstract

To understand and resolve uncertainties regarding climate change, accurate observations must be utilized. Satellite remote sensing provides the best way to obtain global observations, yet the assumptions required to convert measured properties of the radiation field to geophysical information yield accuracy levels outside of the necessary range. By using all electromagnetic properties such as spatial, spectral, angular, and polarization these accuracy levels may increase. The National Research Council recognizes this need and states the future of remote sensing observations lie in the development of multi-angle, multi-wavelength, high resolution, polarized retrievals. To meet this need the Jet Propulsion Laboratory in conjunction with the University of Arizona have developed the Multiangle SpectroPolarimetric Imager (MSPI). In order to accurately interpret the data from MSPI, polarized radiative transfer models must be used and currently only one dimension versions are available. When emphasizing the need for accurate observations, using assumptions that introduce error to retrievals, such as the plane parallel assumption need to be avoided. Therefore analysis of MSPI data must be performed by polarized models that can incorporate complex three dimensional domains. Although the number of three dimensional polarized models have been developed, currently none are accessible to the public.

This thesis introduces the development of the Polarized Intercomparison of 3D radiation Codes (I3RC-POL); the first publicly available three dimensional, polarized radiative transfer model. Implementation of this model required the modification of many modules and techniques within the original unpolarized I3RC including the extension of the phase function to a 4x4 phase matrix, the representation of a photon as the polarized Stokes vector,

and the selection of scattering angles using the rejection method. Current benchmarking results have found that the I3RC-POL yields results within 1% error for unpolarized intensities compared to the original benchmarked I3RC. Polarized benchmark comparisons have also been performed with the I3RC-POL returning results within 3% error for the intensity component of the Stokes vector. Although initial benchmarking results are promising, some uncertainties must still be resolved in both the unpolarized and polarized results. Once fully benchmarked, the hope is that the open source framework of the I3RC-POL may provide a tool that will be shared and developed further by the remote sensing community.

For my family and friends

Acknowledgments

I would like to first and foremost thank my advisor, Larry Di Girolamo, for his guidance and expertise in the pursuit of this Masters degree. Without his support and patience, I would have never been able to tackle this challenging project. I would also like to acknowledge Maxwell Smith for his extensive assistance in the programming and conceptual challenges I encountered. This research was partially supported through the MISR project through the Jet Propulsion Laboratory of the California Institute of Technology under Subcontract No. 1474871 and through a NASA grant under Agreement No. NNX13AL96G.

I would like to acknowledge the Department of Atmospheric Science and the University of Illinois for my acceptance into this outstanding university and also for my teaching assistant appointment. Through this experiences I was not only given funding towards my degree, but I had the opportunity to discover my true passion of teaching. I would like to also thank my fellow group members and office mates for their constant support, positive attitudes, and willingness to help. Finally, a special thanks to my friends and family. Without their support and unwavering confidence, I would never have completed this research.

Table of Contents

Chapter 1

Introduction

A substantial contribute to the uncertainties in climate change can directly be attributed to uncertainties in aerosols and cloud radiative interactions (*IPCC*, 2007). Due to the complexity of these processes, discussed in more detail in Sections 1.1 and 1.2, current global climate models struggle to advance understanding and consistent results. Improvements must be made in these models by validating against observations but advancements in observational accuracy is also needed. In doing so, the future of remote sensing lies in the use of multi-angle, multi-wavelength, polarized, high resolution retrievals. In order to further understanding and development of this method, tools such as three dimensional radiative transfer models must be available thus the I3RC-POL was developed. This chapter will discuss in further detail the struggles that models and observations have in quantifying cloud and aerosol radiative forcing, followed by the advancement in remote sensing necessary, and the motivation behind the I3RC-POL.

1.1 Uncertainty in Radiative Forcing Due to Clouds

The uncertainty due to clouds and their representation in climate models provides the largest source of uncertainty in climate change even without considering aerosol interactions (*Bony et al.*, 2006). Clouds cover about two thirds of the atmosphere (*Boucher et al.*, 2013) and can have large impacts on the radiation in several ways. The atmosphere warms as water vapor condenses into clouds. Clouds may then influence the flow of incoming solar radiation and outgoing thermal radiation, which directly impacts the Earth's radiation budget. Finally,

clouds contain strong updrafts that act to distribute energy, moisture, and aerosols throughout the atmosphere. Combining these impacts, cloud's influence on the climate is large but the climate can in turn feedback on the clouds. As the climate changes cloud characteristics such as cloud amount, cloud top height, and cloud reflectivity may also change (*Boucher et al.*, 2013). Combining these multiple influences on the climate and the lack of understanding of cloud feedback processes, uncertainty due to cloud radiative forcing becomes considerable.

In order to better resolve these uncertainties, clouds must be better represented in climate models yet the lack of accurate representation and consistency between models becomes a dominant source of radiative forcing uncertainty. Several difficulties are present in the modeling of cloud dynamics and radiative forcing. First the spatial distribution of clouds is large and the vertical variation of different types of clouds vertically must be resolved using different grid sizes and often high resolution models (*Boucher et al.*, 2013). In addition, the parameterization of cloud microphysics and the interaction between clouds and aerosols, to be discussed in Section 1.2, is not represented accurately. The result is a lack of agreement in model radiative forcing output, often with a magnitude of about 10W m^{-2} (*Bony and Dufresne*, 2005). When models are inconsistent, the understanding of clouds and their radiative forcing becomes limited. One possible method in improving these model includes their validation again observational data which may also be improved as seen in Section 1.3.

1.2 Uncertainty in Radiative Forcing Due to Aerosols

The complexity of aerosols and their interaction with clouds and radiation supplies an additional source of radiative forcing uncertainty (*Boucher et al.*, 2013). Aerosols may directly influence radiation by scattering and absorption, known as the direct effect. Additionally, aerosols can act as cloud condensation nuclei (CCN) which alters cloud microphysics and their radiative properties. For example, when increasing the number of CCN, cloud droplet

size may decrease which in turn increases the albedo of the cloud (*Twomey*, 1977) or the lifetime of the cloud. Considering clouds already have such an influential forcing on radiation, the introduction of aerosols can only further their impact. Finally, adding to the uncertainty is the spatial and temporal distribution of different aerosol types (*Myhre et al.*, 2013). Varying aerosol species each have their own microphysics along with unique lifetimes and location in the atmosphere which may impact the radiative forcing in different ways.

In order to understand the influence of aerosols on the climate, models must be able to simulate this intricate process. Current representation of these interactions remain primitive (*Boucher et al.*, 2013). These processes that occur at such a small scale can not be accurately represented over large scale fields (*Boucher et al.*, 2013). In addition, parameterization of aerosols and their species remain variable between different models. This lack of consistent parameterization along with the complexity in simulations fuels the inability of models to produce uniform radiative forcing results (*Boucher et al.*, 2013). Similar to clouds in climate models, observational studies may be used to resolve the uncertainties in aerosols in climate models by providing a valid tool for comparison.

1.3 Observational Inaccuracies

1.3.1 Current State of Observational Studies

As specified in Sections 1.1 and 1.2, observations may provide the tools necessary to increase model accuracy. The following questions must be asked, how accurate do observations need to be and do current techniques meet these accuracies? The National Institute of Standards and Technology (NIST), the National Polar-orbiting operational Environmental Polar-orbiting Operational Environmental Satellite System (NPOESS) Integrated Program Office (IPO), the National Oceanic and Atmospheric Administration (NOAA), and the National Aeronautics and Space Administration (NASA) organized a workshop of 75 remote sensing scientists to address these questions. The overall consensus was that cloud and aerosol re-

trievals do not maintain the accuracies necessary (*Ohring et al.*, 2005). For example, cloud effective radius must be measured within 0.5 μm but current retrievals only measure effective radius within 2 - 17 μm. These inaccuracies can be directly attributed to assumptions made in algorithms and inadequate technology in which both need improvements.

1.3.2 Plane Parallel Assumption

An example of an assumption used in remote sensing and models that induces error is the plane parallel assumption. In order to improve computational efficiency, the plane parallel assumption considers changes in the vertical while ignoring horizontal heterogeneity. In doing so, three dimensional characteristics of clouds such as shadowing and side illumination are not considered. Several studies have shown that retrieval biases arise from ignoring such three dimensional characteristics. Di Girolamo found that the spherical albedo, reflectance, and optical thickness of retrieved clouds is indistinguishable from plane-parellel clouds only 24% of the time (*Di Girolamo et al.*, 2010). Marshak et al (2006) also showed that ignoring shadowing causes an overestimation of effective radius. In order to retrieve the most accurate results possible, three dimensional effects must be considered.

1.3.3 Observational Assumptions

As seen in Section 1.3.2, adding an assumptions into remote sensing techniques can increase retrieval error. The plane parallel assumption is not the only assumption used in remote sensing. Additional assumptions include assumed microphysics such as cloud drop size and type, assumed surface properties such as land or vegetation or water, assumed vertical heterogeneity including cloud cover, and finally the lack of sub pixel heterogeneity. Each assumption creates a more idealized, less realistic atmosphere. In order to increase observational accuracy and detail, these assumptions must be avoided or resolved technologically as seen in Section 1.3.4.

1.3.4 Improving Observations

Technological advances must be made in order to address these inaccurate assumptions and the errors they induce. This can be accomplished by increasing the amount of information gathered in retrievals. There are four different electromagnetic properties that remote sensing uses to retrieve information about the atmosphere; spatial, spectral, angular, and polarization. Different imagers use a combination of these four properties. The Moderate Resolution Imaging Spectroradiometer (MODIS) uses the spatial and spectral properties (*Justice et al.*, 1998). The Multi-Angle Imaging Spectroradiometer (MISR) added angular information retrievals (*Diner et al.*, 1998). The Polarization and Directionality of the Earth's Reflectances (POLDER) instrument included polarized information (*Deschamps et al.*, 1994). Although POLDER included information retrieval capabilities of all four electromagnetic properties, its resolution, 6 km, needed to be improved upon. This leads directly to the future of remote sensing. In order to improve observational retrievals, multi-angle, multi-wavelength, polarized, high resolution imagers must be used. The need for such technology has been sighted in both the National Research Council's National Imperatives for the Next Decade and Beyond (2007) and NASA's Space Technology Roadmap (2013) as one of the necessary imagers for the future of scientific research.

1.4 Multi-Angle, Multi-Wavelength, Polarized Remote Sensing Tools

The inclusion of the polarized property of the electromagnetic wave provides a powerful tool in the advancement of aerosol and cloud retrievals. Due to it's high sensitivity of particle microphysics, polarization has the ability to not only extract a wide range of aerosol information but is also able to distinguish between cloud and aerosol particles (*Boucher et al.*, 2013). In addition, the use of polarization can ease the difficult problem of retrieving

aerosols over land surfaces (*Deuzé et al.*, 1993). Polarized retrievals of cloud properties are based upon the analysis of rainbow or cloud bow feature between the scattering angles of 140° and 170°. Within these angles, the polarized phase function experiences a maximum and minimum. Due to polarized reflectance values dependency on the polarized phase function, interpretations of cloud and aerosol size and distribution may be made using these features (*Bréon and Goloub*, 1998). This alternative method to reflected radiance retrievals may provide additional valuable information on aerosol and cloud microphysics.

1.4.1 POLDER

As discussed in Section 1.3.3, remote sensing imagers have been developed to take advantage of polarization's ability to retrieve aerosol and cloud properties. POLDER (Polarization and Directionality of the Earth's Reflectance) launched on the ADEOS platform in 1996, provided valuable information on polarized retrievals (*Bréon and Goloub*, 1998). POLDER was the first imager to provide spatial, spectral, multi-directional, and polarized measurements (*Alexandrov et al.*, 2012) Some of the questions that POLDER tried to address included but were not limited to: the use of polarized reflectance to characterize atmospheric aerosols optical properties and polarization's simplification of aerosol retrievals over complicated surface such as land (*Deuzé et al.*, 1993). Unfortunately, the advancements in observational accuracy by POLDER could not meet the accuracy needs due to it's very coarse resolution of 6 km. In order for observational studies to improve, not only does polarization need to be considered but it also must be used at a high resolution.

1.4.2 MSPI

The development of the Mulitangle SpectroPolarimetric Imager (MSPI) by the Jet Propulsion Laboratory (JPL) improves on the POLDER instrument by increasing resolution from 6 km in POLDER to 25 - 250 m (*Diner et al.*, 2013). MSPI is an eight-band imager (355,

380, 445, 470*, 550, 660*, 865*, 935 nm) where * indicates the bands in which polarization is included (*Diner et al.*, 2013). In addition to improving POLDER's resolution, MSPI also includes improvements of the current multi angular imager MISR by the inclusion of polarization, ultraviolet and IR bands, and a wider field of view (*Diner et al.*, 2013). Three versions of MSPI have been developed with the most current version, AirMSPI mounted on the NASA ER-2 Plane. Test flights over California and the Pacific Ocean have demonstrated the capabilities of the AirMSPI camera. Such retrievals include cloud droplet size, aerosol size, cloud top, and cloud base heights (*Diner et al.*, 2013). In order to understand these retrievals, a 3D polarized model must be used.

1.5 I3RC-POL Motivation

A three dimensional polarized radiative transfer model provides a necessary tools to understand MSPI retrievals. While there are many available one dimensional polarized radiative transfer codes, the three dimensional radiative transfer models that have been developed are not available to the public. This need leads directly to the motivation of this thesis. Through the development of the three dimensional polarized radiative transfer model, I3RC-POL, we aim to provide the available, necessary tool to analyze and model observation studies using imagers such as AirMSPI. Through these analysis, an improvement and better understanding of aerosol and cloud microphysics may be gained in hopes of reducing aerosol and cloud climatological uncertainties.

Chapter 2

Polarization

The purpose of this section is to provide a broad overview of the polarization concepts necessary for polarized radiative transfer. While this chapter is limited to a small discussion on polarization, there are several resources available for a wide range of polarized material from author's such as Chandrasekhar (1960), Van de Hulst (1957), Mishchenko (2002), and Liou (2002).

2.1 Polarized Representation

2.1.1 Vector Wave Solution of Maxwell's Equation

Electromagnetic waves may be used to represent light and its propagation. As a disturbance occurs in an electric or magnetic field, an additional disturbance is also initiated in the other respective field. The result is a propagating wave with both an electric and magnetic component. The basis of any electromagnetic wave derivation begins with Maxwell's equation (*Liou*, 2002):

$$\nabla \times \mathbf{H} = \frac{1}{c}\frac{\partial \mathbf{D}}{\partial t} + \frac{4\pi}{c}\mathbf{J} \tag{2.1}$$

$$\nabla \times \mathbf{E} = -\frac{1}{c}\frac{\partial \mathbf{B}}{\partial t} \tag{2.2}$$

$$\nabla \cdot \mathbf{D} = 4\pi\rho \tag{2.3}$$

$$\nabla \cdot \mathbf{B} = 0 \tag{2.4}$$

Where $\mathbf{D}$ is the electric displacement vector, $\mathbf{E}$ is the electric field vector, $\mathbf{B}$ is the magnetic induction vector, $\mathbf{H}$ is the magnetic field vector, ρ is the electric charge density, $\mathbf{J}$ is the electric current vector, c is the velocity of light, and t is time. The following assumptions are also often used in studying solutions to describe Maxwell's equations (*Liou*, 2002):

$$\mathbf{J} = \sigma\mathbf{E} \tag{2.5}$$

$$\mathbf{B} = \mu\mathbf{H} \tag{2.6}$$

$$\mathbf{D} = \varepsilon\mathbf{E} \tag{2.7}$$

where μ represents the magnetic permeability, σ represents the conductivity of the medium, and ε is the permittivity (*Liou*, 2002). When the medium has no charge, $\rho = 0$ and $\mathbf{J} = 0$, and is homogenous making ε and μ constants, Maxwell's equations reduce to:

$$\nabla \times \mathbf{H} = \frac{\varepsilon}{c}\frac{\partial \mathbf{E}}{\partial t} \tag{2.8}$$

$$\nabla \times \mathbf{E} = -\frac{\mu}{c}\frac{\partial \mathbf{H}}{\partial t} \tag{2.9}$$

$$\nabla \cdot \mathbf{H} = 0 \tag{2.10}$$

$$\nabla \cdot \mathbf{E} = 0 \tag{2.11}$$

Finally, solutions to Maxwell's equations may be expressed in terms of the plane wave equation. Consider a plane electromagnetic wave with a circular frequency (ω), the electric and magnetic vectors become:

$$\mathbf{E} = \mathbf{E}e^{it\omega} \tag{2.12}$$

$$\mathbf{H} = \mathbf{H}e^{it\omega} \tag{2.13}$$

Using these equations, Maxwell's Equations' alternate form becomes:

$$\nabla \times \mathbf{H} = \frac{\varepsilon}{c}\frac{\partial \mathbf{E}\mathbf{e}^{\mathbf{it}\omega}}{\partial t} \tag{2.14}$$

$$\nabla \times \mathbf{E} = -\frac{\mu}{c}\frac{\partial \mathbf{H}\mathbf{e}^{\mathbf{it}\omega}}{\partial t} \tag{2.15}$$

$$\nabla \cdot \mathbf{H} = 0 \tag{2.16}$$

$$\nabla \cdot \mathbf{E} = 0 \tag{2.17}$$

Completing the time derivative, equations 2.14 and 2.15 can be expressed as:

$$\nabla \times \mathbf{H} = \frac{\omega\varepsilon i}{c}\mathbf{E}e^{it\omega} \tag{2.18}$$

$$\nabla \times \mathbf{E} = -\frac{\omega\mu i}{c}\mathbf{H}e^{it\omega} \tag{2.19}$$

Using the wavenumber ($k = \frac{\omega}{c}$), the complex refractive index of the medium ($m = \sqrt{\epsilon}$), and the permeability of air ($\mu \approx 1$), Maxwell's equations for a plane electromagnetic wave becomes:

$$\nabla \times \mathbf{H} = ikm^2\mathbf{E} \tag{2.20}$$

$$\nabla \times \mathbf{E} = -ik\mathbf{H} \tag{2.21}$$

$$\nabla \cdot \mathbf{H} = 0 \tag{2.22}$$

$$\nabla \cdot \mathbf{E} = 0 \tag{2.23}$$

From this form of Maxwell's equation, the vector wave equation in a homogeneous

medium may be derived. Taking the curl of equation 2.21, the wave equation for the electric component of the electromagnetic wave becomes (*Liou*, 2002):

$$\nabla \times \nabla \times E = ik(\nabla \times \mathbf{H}) \tag{2.24}$$

To simplify this curl operation, the following equations may be used:

$$\nabla \times \nabla \times \mathbf{E} = \nabla(\nabla \cdot \mathbf{E}) - \nabla^2\mathbf{E} \tag{2.25}$$

$$\nabla \cdot \mathbf{E} = 0 \tag{2.26}$$

$$\nabla \times \mathbf{H} = ikm^2\mathbf{E} \tag{2.27}$$

Giving the final form of the electric component's vector wave equation:

$$\nabla^2\mathbf{E} = -k^2m^2\mathbf{E} \tag{2.28}$$

This process may also be performed for the magnetic vector component of the electromagnetic wave. Taking the curl of equation 2.20, the vector wave equation can be derived.

$$\nabla \times \nabla \times \mathbf{H} = ikm^2(\nabla \times \mathbf{E}) \tag{2.29}$$

This derivation uses the following equations:

$$\nabla \times \nabla \times \mathbf{H} = \nabla(\nabla \cdot \mathbf{H}) - \nabla^2\mathbf{H} \tag{2.30}$$

$$\nabla \cdot \mathbf{H} = 0 \tag{2.31}$$

$$\nabla \times \mathbf{E} = -ik\mathbf{H} \tag{2.32}$$

The final form of the magnetic vector wave equation becomes:

$$\nabla^2 \mathbf{H} = -k^2 m^2 \mathbf{H} \tag{2.33}$$

2.1.2 Stokes Vector

While Maxwell's equations can describe the relationship between the electric and magnetic field in the form of a vector wave equation, it is necessary to analyze the components of the electric field so that not only a description of it's orientation may be formed but can also be measured by instruments. The real portion of the transverse electric field vector may be decomposed into a parallel ($\vec{l}$) and perpendicular ($\vec{r}$) components relative to a reference plane within a 3D reference frame:

$$\mathbf{E} = Re[E_l \vec{l} + E_r \vec{r}] \tag{2.34}$$

where $\vec{r}$ is the is the unit vector along the normal of the meridian plane and $\vec{l}$ is the unit vector in the meridian plane and is perpendicular to the direction of propagation. This reference frame in which the Stokes vector is defined is the the meridian plane which is based upon the direction of propagation and the Z axis, shown in Figure 2.1.

The electric field is complex and oscillating making the parallel and perpendicular components seen in equation 2.34:

$$E_l = a_l exp(-i(\xi + \delta_l)) \tag{2.35}$$

$$E_r = a_r exp(-i(\xi + \delta_r)) \tag{2.36}$$

where a_l and a_r are the amplitudes, δ_l and δ_r are the phases, and $\xi = kz - (\omega)t$ where k is the wavenumber and ω is the frequency of the wave (*Liou*, 2002). It is important to

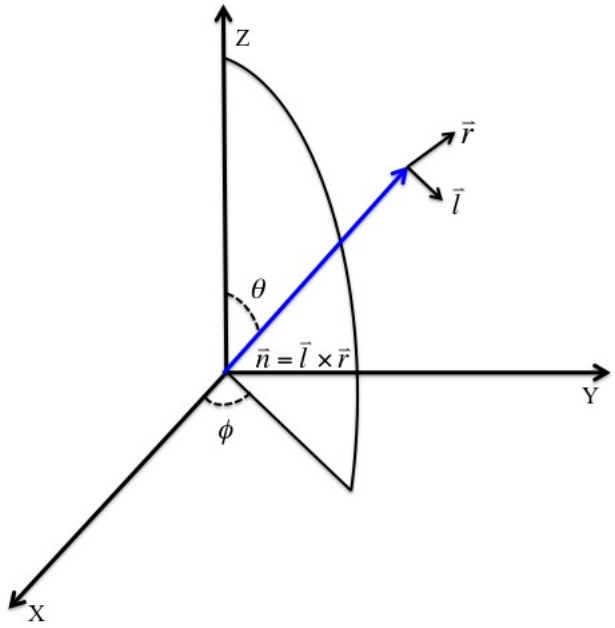

Figure 2.1: Coordinate system for the derivation of the Stokes vector. The electric field vector is shown in blue and is decomposed into it's parallel ($\vec{l}$) and perpendicular ($\vec{r}$) components. We may also define the unit vector, ($\vec{n}$) as the direction of propagation where $\vec{n} = \vec{l} \times \vec{r}$ (*Liou*, 2002) Finally, the meridian plane in which the Stokes vector will be defined can be seen in black

.

note that these quantities of a wave can not be measured by most polarmetric instruments (*Mishchenko et al.*, 2002). In order for optical instruments to measure radiative quantities from the electromagnetic wave, these components of the electric field may be used to express real, time averaged, energy flux values. This need for measurable quantities lead to the creation of the Stokes vector. Through a series of experiments, four measurable parameters with the same units as intensity were introduced. Ignoring a constant of proportionality, these Stokes vectors may be defined as (*Liou*, 2002):

$$\mathbf{I} = \begin{pmatrix} I \\ Q \\ U \\ V \end{pmatrix} = \begin{pmatrix} E_l E_l^* + E_r E_r^* \\ E_l E_l^* - E_r E_r^* \\ E_l E_r^* + E_r E_l^* \\ -i(E_r E_l^* - E_l E_r^*) \end{pmatrix} \tag{2.37}$$

As another example of the Stokes vector representation, an alternative form is derived using the amplitude and phase difference of the wave. This version of the Stokes vector may be more intuitive because it uses understandable characteristics of the electromagnetic wave. Using equations 2.35, 2.36, 2.37 and assuming the wavenumber k and the angular frequency ω are prescribed (*Van de Hulst*, 1957), the Stokes vector becomes:

$$\mathbf{I} = \begin{pmatrix} I \\ Q \\ U \\ V \end{pmatrix} = \begin{pmatrix} E_l E_l^* + E_r E_r^* \\ E_l E_l^* + E_r E_r^* \\ E_l E_r^* + E_r E_l^* \\ -i(E_r E_l^* - E_r E_l^*) \end{pmatrix}$$

$$= \begin{pmatrix} a_l exp(-i\delta_l) a_l exp(i\delta_l) * + a_r exp(-i\delta_r) a_r exp(i\delta_r) * \\ a_l exp(-i\delta_l) a_l exp(i\delta_l) * - a_r exp(-i\delta_r) a_r exp(i\delta_r) * \\ a_l exp(-i\delta_l) a_r exp(i\delta_r) * + a_r exp(-i\delta_r) a_l exp(i\delta_l) * \\ -i(a_r exp(-i\delta_r) a_l exp(i\delta_l) * - a_r exp(-i\delta_r) a_l exp(i\delta_l) *) \end{pmatrix} \quad (2.38)$$

where $exp(-i\delta)^* = exp(i\delta)$. This equation can be simplified further using $\delta = \delta_r - \delta_l$ and Euler's formula $exp(i\delta)$ becomes $\cos(\delta) + i\sin(\delta)$ where the real portion is equivalent to $\cos(\delta)$ and the imaginary portion is represented by $\sin(\delta)$. Utilizing these equations, the Stokes vector becomes (*Liou*, 2002):

$$\mathbf{I} = \begin{pmatrix} I \\ Q \\ U \\ V \end{pmatrix} = \begin{pmatrix} a_l^2 + a_r^2 \\ a_l^2 - E_r^2 \\ 2a_l a_r \cos(\delta) \\ 2a_l a_r \sin(\delta) \end{pmatrix} \quad (2.39)$$

Physical Meaning

Each component of the Stokes vector describes a certain characteristic of the propagating wave. The I component of the Stokes vector is equivalent to the sum of the squared amplitudes of the electric field components which represents the full intensity of the wave. Regardless of if the electromagnetic wave is fully polarized, partially polarized, or unpolarized, the intensity of the wave will always be represented by this component. The Q, U, and V components all help to describe how much of the Stokes vector is polarized and its orientation. Keeping in mind the three different degrees of polarization, the intensity relationship between the four different components become:

$$I = Q + U + V \tag{2.40}$$

If the wave is partially polarized:

$$I \geq Q + U + V \tag{2.41}$$

If the electromagnetic wave is unpolarized, as is solar radiation, there will be no Q, U, and V values of the Stokes vector. The Stokes vector of unpolarized light becomes:

$$\begin{pmatrix} I \\ Q \\ U \\ V \end{pmatrix} = \begin{pmatrix} I \\ 0 \\ 0 \\ 0 \end{pmatrix} \tag{2.42}$$

$$\tag{2.43}$$

The Q, U, and V components describe not only the amount of polarization but also the type. The Q and U components can be used to quantify the linear polarization while the V component describes the amount of circular polarization that is present within the

electromagnetic wave. Finally by combining the Q, U, and V components, an elliptically polarized electromagnetic wave may also be represented (Figure 2.2).

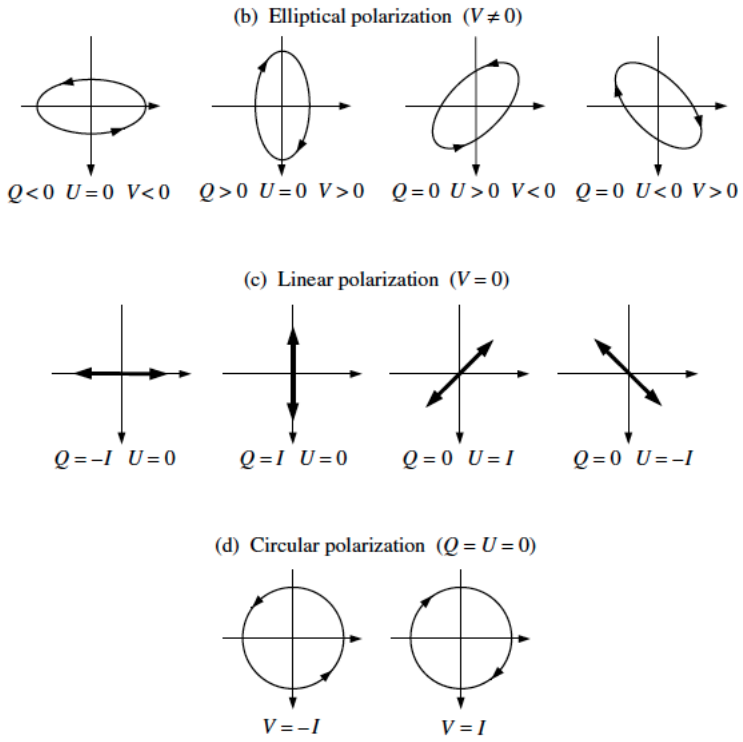

Figure 2.2: Different combinations of the Stokes vector components and their resulting types of polarization (*Mishchenko et al.*, 2002)

By using these relationships, it is possible to use the Stokes vector to describe the degree of polarization, linear polarization, and circular polarization as followed:

$$P_{polarization} = \frac{\sqrt{(Q+U+V)^2}}{I} \qquad P_{linear} = \frac{\sqrt{(Q+U)^2}}{I} \qquad P_{circular} = \frac{(V)}{I} \tag{2.44}$$

The Stokes vector's ability to be measured and its ability to represent the magnitude and orientation of the electromagnetic wave makes this representation common when performing polarized radiative transfer computations.

2.2 Polarized Radiative Transfer

As this electromagnetic wave propagates through the atmosphere, it will encounter different particles and the surface. In doing so, some of this radiance along the path may be lost due to extinction or gained due to emission and/or diffuse scattering. In order to describe the amount of change, the polarized radiative transfer equation is used. While similar to the scalar radiative transfer equation, the polarized radiative transfer equation must treat radiance as the Stokes vector and scattering phase function in more detail by using a phase matrix. This matrix will be discussed in detail in Section 2.3. Due to the complexity of these computations, this equation is often simplified to a plane-parallel, monochromatic atmosphere with randomly oriented particles (*Evans and Stephens*, 1991). The complete polarized radiative transfer equation becomes:

$$\mu \frac{d\mathbf{I}(\tau,\theta,\phi)}{d\tau} = \underbrace{-\mathbf{I}(\tau,\theta,\phi)}_{\text{Extinction Term}} + \underbrace{\frac{\omega_0}{4\pi}\int_0^{2\pi}\int_{-1}^{1} Z(\mu,\phi;\mu',\phi')\mathbf{I}(\tau,\theta',\phi')\,d\mu'\,d\phi'}_{\text{Diffuse Scattering}} + \underbrace{(1-\omega_0)B(T)\begin{pmatrix}1\\0\\0\\0\end{pmatrix}}_{\text{Thermal Emission}} \tag{2.45}$$

where μ is the cosine of the zenith angle (θ), (μ',ϕ') represents the initial direction, (μ,ϕ) represents the scattered direction, τ is the optical path, ϕ is the azimuth angle, $\mathbf{I}(\tau,\theta,\phi)$ is the Stokes vector, ω_0 is the single scattering albedo, and $Z(\mu,\phi;\mu',\phi')$ is the scattering matrix.

2.2.1 Extinction Term

$$\text{Radiance Extinction} = -\mathbf{I}(\tau, \theta, \phi) \tag{2.46}$$

This expression represents the amount of radiance attenuated over a certain optical path through a medium. The loss of radiance is caused by the interaction with particles leading to scattering or absorption. Scattering refers to the redirection of radiation out of the original path, while absorption is the conversion of radiant energy into an alternate form of energy such as kinetic, vibrational, heat or chemical energy. The amount of extinction that occurs may be quantified using the volume extinction coefficient (β_e) and Beer's law. An alternative description of extinction is to use the extinction matrix along a certain path length. This method is described in detail by Mischencko (2002).

2.2.2 Diffuse Scattering

$$\text{Diffuse Scattering} = \frac{\omega_0}{4\pi} \int_0^{2\pi} \int_{-1}^{1} Z(\mu, \phi; \mu' \phi') \mathbf{I}(\tau, \theta', \phi') \, d\mu' \, d\phi' \tag{2.47}$$

The diffuse scattering source term takes into consideration the amount of radiance and the resulting change of polarization into the specified direction of propagation. This term is dependent on the single scattering albedo (ω_0), the Stokes vector $\mathbf{I}(\tau, \theta', \phi')$, and the phase matrix $Z(\mu, \phi; \mu', \phi')$. In addition, the incoming (μ', ϕ') and outgoing (μ, ϕ) directions must be considered. The single scattering albedo characterizes the amount of scattering that occurs by the medium relative to total extinction and the 4π represents the normalization so that the scattered radiance will fall within the solid angle of 4π steradians.

The integral portion of this expression describes the amount of scattering that occurs from an alternate direction into the direction of propagation. In the unpolarized, scalar, radiative transfer equation this process is modeled using the scalar phase function. Since polarization describes not only the radiance amount but also the orientation, the Stokes Vector is used to describe the radiance. This is done using the normalized, 4x4 phase matrix. The phase

matrix is a complicated feature of the polarized radiative transfer equation. For further explanation, Section 2.3 provides a detailed derivation

2.2.3 Thermal Emission

$$\text{Thermal Emission} = (1-\omega_0)B(T)\begin{pmatrix}1\\0\\0\\0\end{pmatrix} \tag{2.48}$$

The thermal emission source term takes into consideration the amount of radiance emitted. Note, thermal emission is unpolarized. The amount of emission that will occur is based upon Kirchoff's law, which states that the emissivity is equal to absorptivity. Using the single scattering albedo (ω_0) which quantifies how much of the extinction is due to scattering, the amount of absorption can be considered by $(1-\omega_0)$. Finally, the amount of emission is directly related to Planck's Function $B(T)$, which describes the intensity emitted by a blackbody emitted at a particular wavelength, with units $Wm^{-2}sr^{-1}um^{-1}$ (*Liou*, 2002):

$$B_\lambda(T,\lambda) = \frac{2hc^2}{\lambda^5[e^{\frac{hc}{KT\lambda}}-1]} \tag{2.49}$$

where K is the Boltzmann's constant equal to 1.3806×10^{-23} J deg^{-1}, c is the velocity of light, T is the absolute temperature, λ is the wavelength, and h is the Planck constant equal to 6.626×10^{-34} J sec.

2.3 Phase Matrix Derivation

Scattering in the scalar version of the radiative transfer equation is represented using a scalar phase function. When considering polarization, this phase function can no longer be used. Instead, due to the vector nature of polarization and the dependence on a specific reference frame, the phase matrix is used instead of a phase function.

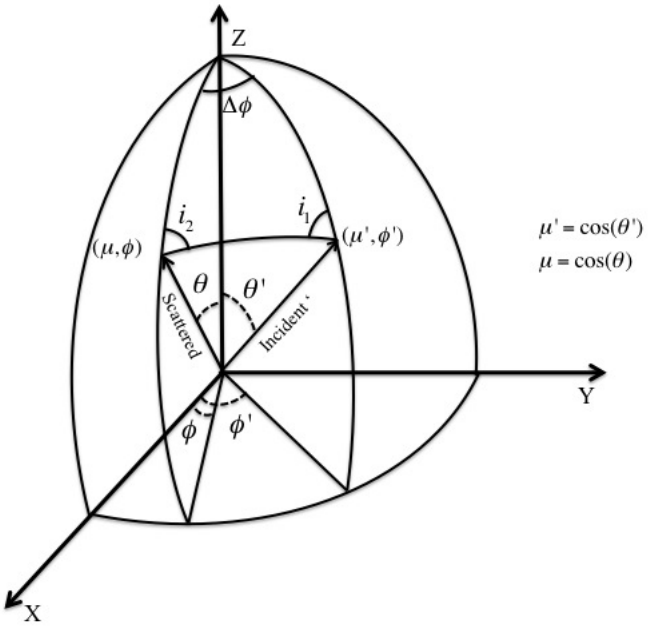

Figure 2.3: Geometry of the scattering event between an electromagnetic wave with direction (μ', ϕ') into the scattered direction of (μ, ϕ)

As seen in Section 2.2.1, the Stokes vector reference frame is conventionally defined using the meridian plane, which is defined using the z-axis and the direction of propagation. When the electromagnetic wave is scattered, it propagates in a new direction with a new the meridian plane and the Stokes vector must also be defined within this new meridian plane. This requires a series of rotations of the Stokes vector represented by three matrices. The relationships between the directions of propagations and planes can be seen in Figure 2.3. In order to represent the rotations and scattering of the Stokes vector, the phase matrix is defined as:(*Liou*, 2002):

$$Z(\theta, \phi : \theta', \phi') = L(\pi - i_2)P(\Theta)L(-i_1) \tag{2.50}$$

where:

$$\cos(i_1) = \frac{\mu - \mu' \cos(\Theta)}{\pm\sqrt{1-\mu^2}\sqrt{1-cos(\Theta)^2}} \tag{2.51}$$

$$\cos(i_2) = \frac{\mu' - \mu\cos(\Theta)}{\pm\sqrt{1-\mu'^2}\sqrt{1-cos(\Theta)^2}} \tag{2.52}$$

$$cos(\Theta) = \mu\mu' + \sqrt{(1-\mu^2)}\sqrt{(1-\mu')}cos(\phi - \phi') \tag{2.53}$$

Physically, this phase matrix can be though of as a series of rotations and a scattering event. Initially, the Stokes vector is referenced within the meridian plane, defined using the incoming direction of propagation and the z axis. In order to be scattered, the Stokes vector must lie in the scattering plane defined by the incoming and outgoing directions. A rotation between the initial meridian plane into the scattering plane must occur using the rotation matrix (L) and the rotation angle (i_1). Note that the rotation angle is negative representing a counterclockwise rotation. When the Stokes vector is defined within the correct scattering plane, it may be scattered from the incident to the new direction of propagation using the scattering phase matrix $P(\Theta)$ and the scattering angle (Θ). Once the Stokes vector is scattered into a new direction, it must again be defined within the correct meridian plane using the new direction of propagation. This final step, rotating the Stokes vector out of the scattering plane into its newly defined meridian plane, is accomplished using $L(\pi - i_2)$. The rotation matrix (L) rotates the Stokes vector clockwise by an angle combination ($\pi - i_2$). The final resulting Stokes vector is defined in a new meridian plane propagating in a new direction. The following section describes in detail the scattering phase matrix $P(\Theta)$, rotation matrix $L(i)$, and angles necessary for this complicated scattering process and the formation of the phase matrix $Z(\mu, \phi; \mu', \phi')$.

2.3.1 Rotation Matrix

The rotation matrix $L(i)$ is used to rotate the Stokes vector between intersecting reference planes having an angle (i) between them. This rotation occurs in the clockwise direction from the meridian plane.

$$L(i) = \begin{pmatrix} 1 & 0 & 0 & 0 \\ 0 & \cos(2i) & \sin(2i) & 0 \\ 0 & -\sin(2i) & \cos(2i) & 0 \\ 0 & 0 & 0 & 1 \end{pmatrix} \tag{2.54}$$

A rotation in the counterclockwise direction can also be achieved by using an opposites sign of $\sin(2i)$. This may be done by using an alternative rotation matrix or by changing the sign of the rotation angle (i).

Rotation Matrix Derivation

Any rotation of the Stokes vector can be represented by a generic rotation matrix. This section aims to derive the elements of this matrix given a clockwise rotation:

$$\mathbf{I} = L(i)\mathbf{I}' \tag{2.55}$$

$$L(i) = \begin{pmatrix} L_{11} & L_{12} & L_{13} & L_{14} \\ L_{21} & L_{22} & L_{23} & L_{24} \\ L_{31} & L_{32} & L_{33} & L_{34} \\ L_{41} & L_{42} & L_{43} & L_{44} \end{pmatrix} \tag{2.56}$$

where:

$$I = L_{11}I' + L_{12}Q' + L_{12}U' + L_{14}V' \tag{2.57}$$

$$Q = L_{21}I' + L_{22}Q' + L_{22}U' + L_{24}V' \tag{2.58}$$

$$U = L_{31}I' + L_{32}Q' + L_{32}U' + L_{34}V' \tag{2.59}$$

$$V = L_{41}I' + L_{42}Q' + L_{42}U' + L_{44}V' \tag{2.60}$$

To derive the rotation matrix, consider an initial electromagnetic wave A, with electric field components $E_l = a_l$ and $E_r = a_r$. This wave is rotated in a clockwise direction by an angle (i) creating a new electromagnetic wave (B) where the rotated components, using trigonometry, may be represented in terms of the initial components and the rotation angle. (*McMaster*, 1961):

$$b_l = a_l \cos(i) + a_r \sin(i) \tag{2.61}$$

$$b_r = -a_l \sin(i) + a_r \cos(i) \tag{2.62}$$

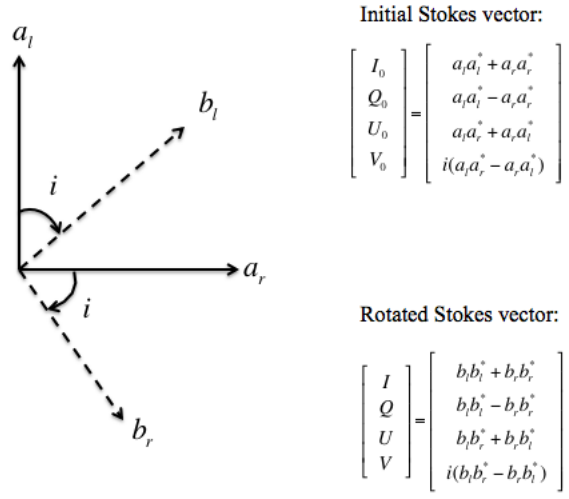

Figure 2.4: Rotation of an initial Stokes vector in the clockwise direction by an angle of (i)

Given the definition of the Stokes vector in Figure 2.4 and equations 2.37, 2.61, and 2.62, the Stokes vector of the rotated electromagnetic wave becomes (*McMaster*, 1961):

$$\begin{pmatrix} I \\ Q \\ U \\ V \end{pmatrix} = \begin{pmatrix} b_l b_l^* + b_r b_r^* \\ b_l b_l^* - b_r b_r^* \\ b_l b_r^* + b_r b_l^* \\ i(b_l b_r^* - b_r b_l^*) \end{pmatrix}$$

$$= \begin{pmatrix} (a_l\cos(i) + a_r\sin(i))(a_l\cos(i) + a_r\sin(i))^* \\ \qquad + (-a_l\sin(i) + a_r\cos(i))(-a_l\sin(i) + a_r\cos(i))^* \\ (a_l\cos(i) + a_r\sin(i))(a_l\cos(i) + a_r\sin(i))^* \\ \qquad - (-a_l\sin(i) + a_r\cos(i))(-a_l\sin(i) + a_r\cos(i))^* \\ (a_l\cos(i) + a_r\sin(i))(-a_l\sin(i) + a_r\cos(i))^* \\ \qquad + (-a_l\sin(i) + a_r\cos(i))(a_l\cos(i) + a_r\sin(i))^* \\ i((a_l\cos(i) + a_r\sin(i))(-a_l\sin(i) + a_r\cos(i))^* \\ \qquad - (-a_l\sin(i) + a_r\cos(i))(a_l\cos(i) + a_r\sin(i))^*) \end{pmatrix} \tag{2.63}$$

By using this definition of the Stokes vector and comparing to equations 2.57-2.60 and 2.63, the missing terms of the generic rotation matrix can be derived. The I component of the rotated Stokes Vector can be related to the first row of the rotation matrix.

$$\begin{aligned} I = {} & (a_l\cos(i) + a_r\sin(i))(a_l\cos(i) + a_r\sin(i))^* \\ & + (-a_l\sin(i) + a_r\cos(i))(-a_l\sin(i) + a_r\cos(i))^* \end{aligned} \tag{2.64}$$

$$I = \underbrace{(a_l a_l^* + a_r a_r^*)}_{I'} \underbrace{(\cos^2(\theta) + \sin^2(\theta))}_{1} \tag{2.65}$$

$$I = \underbrace{L_{11}}_{1} I' + 0Q' + 0U' + 0V' \tag{2.66}$$

This may also be completed for the Q component and the results 2nd row of the generic

rotation matrix:

$$\begin{aligned} Q = &(a_l\cos(i) + a_r\sin(i))(a_l\cos(i) - a_r\sin(i))^* \\ &+ (-a_l\sin(i) + a_r\cos(i))(-a_l\sin(i) + a_r\cos(i))^* \end{aligned} \tag{2.67}$$

$$Q = \underbrace{(a_l a_l^* - a_r a_r^*)}_{Q'}(\cos(2i)) + \underbrace{(a_l a_r^* + a_r a_l^*)}_{U'}(\sin(2i)) \tag{2.68}$$

$$Q = 0I' + \underbrace{L_{22}}_{\cos(2i)} Q' + \underbrace{L_{23}}_{\sin(2i)} U' + 0V' \tag{2.69}$$

Comparing to equation 2.59, the U component may be used to derive the third row of the rotation matrix:

$$\begin{aligned} U = &(a_l\cos(i) + a_r\sin(i))(-a_l\cos(i) - a_r\sin(i))^* \\ &+ (-a_l\sin(i) + a_r\cos(i))(a_l\cos(i) + a_r\sin(i))^* \end{aligned} \tag{2.70}$$

$$U = \underbrace{(a_l a_l^* - a_r a_r^*)}_{Q'}(-2\sin(i)\cos(i)) + \underbrace{(a_l a_r^* + a_r a_l^*)}_{U'}(\cos^2(i) - \sin^2(i)) \tag{2.71}$$

$$U = 0I' + \underbrace{L_{33}}_{-\sin(2i)} Q' + \underbrace{L_{34}}_{\cos(2i)} U' + 0V' \tag{2.72}$$

Finally, the V component may also be used to determine the final row of the rotation matrix:

$$\begin{aligned} V = &i((a_l\cos(i) + a_r\sin(i))(-a_l\sin(i) + a_r\cos(i))^* \\ &- (-a_l\sin(i) + a_r\cos(i))(a_l\cos(i) + a_r\sin(i))^*) \end{aligned} \tag{2.73}$$

$$V = \underbrace{i(a_l a_r^* - a_r a_l^*)}_{V'}\underbrace{(\cos^2(\theta) + \sin^2(\theta))}_{1} \tag{2.74}$$

$$V = 0I' + 0Q' + 0U' + \underbrace{L_{44}}_{1} V' \tag{2.75}$$

All the elements of the rotation matrix have been derived, making the final rotation matrix

in the clockwise direction:

$$L(i) = \begin{pmatrix} 1 & 0 & 0 & 0 \\ 0 & \cos(2i) & \sin(2i) & 0 \\ 0 & -\sin(2i) & \cos(2i) & 0 \\ 0 & 0 & 0 & 1 \end{pmatrix} \tag{2.76}$$

2.3.2 Rotation Angles

The angles in which the Stokes vector are rotated are labeled i_1 and i_2 within Figure 2.3. The first angle (i_1) rotates the Stokes vector from the meridional plane of the incident direction into the scattering plane. The second angle (i_2) rotates the Stokes vector from the scattering plane into the meridian plane defined by the new direction of propagation. These angles can be represented by when $\mu = +\cos(\theta)$:

$$\cos(i_1) = \frac{\mu - \mu' \cos(\Theta)}{\pm\sqrt{1-\mu^2}\sqrt{1-cos(\Theta)^2}} \tag{2.77}$$

$$\cos(i_2) = \frac{\mu' - \mu \cos(\Theta)}{\pm\sqrt{1-\mu'^2}\sqrt{1-cos(\Theta)^2}} \tag{2.78}$$

Rotation Angle Derivation

The spherical law of cosines, which relates the sides and angles of a spherical triangle, is used to derive the rotation angles. An example spherical triangle and its corresponding spherical law of cosine is given in equation 2.79 and Figure 2.5.

$$\cos(c) = \cos(a)\cos(b) + \sin(a)\sin(b)\cos(C) \tag{2.79}$$

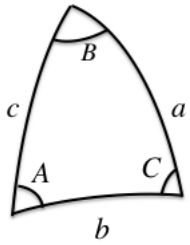

Figure 2.5: Sample spherical triangle used in the law of cosines

It is possible to relate this formulation directly to Figure 2.3. The spherical triangle defined by the Z axis and the directions of propagation, becomes:

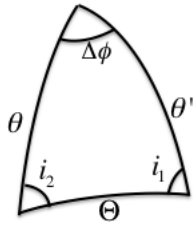

Figure 2.6: Spherical triangle defined in Figure 2.3

Using the same law of cosines in terms of Figure 2.6, equation 2.79 becomes:

$$\cos(\theta) = \cos(\theta')\cos(\Theta) + \sin(\theta')\sin(\Theta)\cos(i_1) \tag{2.80}$$

$$\cos(\theta') = \cos(\theta)\cos(\Theta) + \sin(\theta)\sin(\Theta)\cos(i_2) \tag{2.81}$$

By rearranging these equations, the rotation angles are defined as follows:

$$\cos(i_1) = \frac{\cos(\theta) - \cos(\theta')\cos(\Theta)}{\pm\sin(\theta')\sin(\Theta)} \tag{2.82}$$

$$\cos(i_2) = \frac{\cos(\theta') - \cos(\theta)\cos(\Theta)}{\pm\sin(\theta)\sin(\Theta)} \tag{2.83}$$

Finally these angles may be defined in terms of μ instead of cosines where $\mu = \cos(\theta)$. If the $\mu = -\cos(\theta)$ the sign of the rotation angle will be opposite. The plus or minus sign is dependent upon the difference between azimuth angles. The denominator is positive when $\pi < \phi - \phi' < 2\pi$ and negative when $0 < \phi - \phi' < \pi$

$$\cos(i_1) = \frac{\mu - \mu'\cos(\Theta)}{\pm\sqrt{1-\mu^2}\sqrt{1-\cos(\Theta)^2}} \tag{2.84}$$

$$\cos(i_2) = \frac{\mu' - \mu\cos(\Theta)}{\pm\sqrt{1-\mu'^2}\sqrt{1-\cos(\Theta)^2}} \tag{2.85}$$

2.3.3 Scattering Angle

As seen in the introduction of Sections 2.3 and 2.3.2, the rotation angle and the scattering of the stokes vector is dependent on the scattering angle (Θ), which is the angle between the incident and outgoing directions of propagation. This angle can be easily derived using cartesian vectors describing these directions. Given an initial direction vector $v' = (v'_x, v'_y, v'_z)$, the different cartesian coordinates may be expressed as spherical coordinate system quantities (μ', ϕ'):

$$v'_x = \sin\theta'\cos(\phi') \tag{2.86}$$

$$v'_y = \sin\theta'\sin(\phi') \tag{2.87}$$

$$v'_z = \cos(\theta') \tag{2.88}$$

This expression may also be used for an outgoing direction vector $v = (v_x.v_y, v_z)$:

$$v_x = \sin\theta\cos(\phi) \tag{2.89}$$

$$v_y = \sin\theta\sin(\phi) \tag{2.90}$$

$$v_z = \cos(\theta) \tag{2.91}$$

By taking the dot product of these two direction vectors, which represents the projection of one vector into the other, the expression for the scattering angle may be derived:

$$\cos(\Theta) = v \cdot v' = v_x v'_x + v_y v'_y + v_z v'_z \tag{2.92}$$

Using the spherical representation of each component, equation 2.92 becomes:

$$\cos(\Theta) = v \cdot v' = \sin\theta\cos(\phi)\sin\theta'\cos(\phi') + \sin\theta\sin(\phi)\sin\theta'\sin(\phi') + \cos(\theta)\cos(\theta)' \tag{2.93}$$

where:

$$\cos(\Theta) = \sin\theta\sin\theta'[\cos(\phi)\cos(\phi') + \sin(\phi)\sin(\phi')] + \cos(\theta)\cos(\theta)' \tag{2.94}$$

Using the trigonometric identity $\cos(\phi' - \phi) = \cos(\phi')\cos(\phi) + \sin(\phi')\sin(\phi)$, equation 2.94 becomes:

$$\cos(\Theta) = \cos(\theta)\cos(\theta') + \sin(\theta)\sin(\theta')\cos(\phi - \phi') \tag{2.95}$$

Finally, the scattering angle may be defined using μ:

$$cos(\Theta) = \mu\mu' + \sqrt{(1-\mu^2)}\sqrt{(1-\mu')}cos(\phi - \phi') \tag{2.96}$$

2.3.4 Scattering Phase Matrix

The scattering phase matrix is a 4x4 matrix that describes the scattering of the Stokes vector of the incident wave into the new direction. This scattering phase matrix is made up of 16 unique elements that are derived using the amplitude scattering matrix (*Mishchenko et al.*, 2002). By using the scattering phase matrix, the amount of radiance redirected and the resulting polarization can be described. The scattering phase matrix is dependent on the incoming and outgoing direction of the wave but this relation is often written in terms of the scattering angle (Θ).

$$P(\Theta) = \begin{pmatrix} P_{11}(\Theta) & P_{12}(\Theta) & P_{13}(\Theta) & P_{14}(\Theta) \\ P_{21}(\Theta) & P_{22}(\Theta) & P_{23}(\Theta) & P_{24}(\Theta) \\ P_{31}(\Theta) & P_{32}(\Theta) & P_{33}(\Theta) & P_{34}(\Theta) \\ P_{41}(\Theta) & P_{42}(\Theta) & P_{43}(\Theta) & P_{44}(\Theta) \end{pmatrix} \tag{2.97}$$

Similar to the phase function where $d\omega$ represents the steradian, the scattering phase matrix is normalized (*Hovenier and Van der Mee*, 1983):

$$\frac{1}{4\pi} \int_{4\pi} P_{11}(\Theta)\, d\omega = 1 \tag{2.98}$$

When scattering occurs via randomly oriented particles with a plane of symmetry, the scattering phase matrix simplifies to matrix with only eight elements. If the particles are spherical, as used in the I3RC-POL, the phase matrix simplifies further where only four of these elements are unique:

$$P(\Theta) = \begin{pmatrix} P_{11}(\Theta) & P_{12}(\Theta) & 0 & 0 \\ P_{12}(\Theta) & P_{11}(\Theta) & 0 & 0 \\ 0 & 0 & P_{33}(\Theta) & P_{34}(\Theta) \\ 0 & 0 & -P_{34}(\Theta) & P_{33}(\Theta) \end{pmatrix} \tag{2.99}$$

Some physical insight may be gained from this interpretation of the phase matrix. $P_{11}(\Theta)$ is equivalent to the phase function used in the unpolarized radiative transfer equation. This parameter describes the redistribution of radiance from one direction to the next. Unlike the other terms of the scattering phase matrix, this value can never equal zero. The remaining elements help to describe the resulting polarization. When simulating unpolarized radiance, the scattering phase matrix can still be used by setting all elements to zero besides $P_{11}(\Theta)$.

This scattering phase matrix is in a generic form, meaning the P values coincide to any type of scattering for randomly oriented spherical particles including Mie or Rayleigh. Rayleigh scattering though has an exact form of the phase matrix:

$$P(\Theta)_{rayleigh} = \frac{3}{4}\begin{pmatrix} 1+\cos(\Theta)^2 & 1-\cos(\Theta)^2 & 0 & 0 \\ 1-\cos(\Theta)^2 & 1+\cos(\Theta)^2 & 0 & 0 \\ 0 & 0 & 2\cos(\Theta) & 0 \\ 0 & 0 & 0 & 2\cos(\Theta) \end{pmatrix} \tag{2.100}$$

It is important to note that the scattering phase matrix is highly dependent on incoming and outgoing directions. Changing the orientation of these incoming and outgoing directions may also change the sign of the scattering phase matrix. There are apparent symmetries though that form when considering randomly oriented particles. These relationships are derived in detail by Hovenier (1969) and Mishchenko (2002).

Chapter 3

Current Polarized Models

Prior to developing our own polarized three dimensional radiative transfer model, it was important to consider all models developed. There are currently several different types of radiative transfer model techniques including Monte Carlo, discrete ordinance, successive orders of scattering, and doubling-adding. Each has its own advantage and disadvantages. One major differentiation between all the models are the dimensions and availability. Most of the models currently available to the public are one dimensional. While this simplification still provides accurate results in some situations, it is often necessary to consider a more complex environment. In doing so, an available three dimensional polarized radiative transfer model is necessary, yet very few are developed and none have been made available to the public. This chapter will give an overview of some of the many plane parallel and three dimensional models. For additional information, refer to Kokhanovsy (2009) which also provides some code inter comparison results.

3.1 One Dimensional Polarized Models

3.1.1 POLRADTRAN

Developed by Frank Evans in 1991, POLRADTRAN is a plane-parallel, monochromatic, fully polarized radiative transfer model (*Evans and Stephens*, 1991). The environment in which calculations can occur is vertically inhomogeneous with randomly oriented particles. To describe polarization, this model uses the vector representation of polarization and the

legendre series version of the phase matrix which is reduced to four unique elements based on the assumption of randomly oriented particles. This model utilizes the doubling and adding technique for its calculations. Fully benchmarked using Coulson and Grant/Siewert's model, this method provides a reliable plane-parallel polarized model that is available for public use vie the libradtran package which is a collection of C and fortran radiative codes (*Mayer et al.*, 2005)

3.1.2 SCIATRAN

SCIATRAN is a plane-parallel, fully polarized radiative transfer model that utilizes the discrete ordinate method (*Rozanov et al.*, 2014).This model has an environment that varies in the vertical and also includes a built in HITRAN database for the different gaseous absorption. It also contains information on cloud, surface (including the ocean), and aerosol characteristics. Polarized additions include a normalized Stokes vector represented by a fourier series and a phase matrix represented using generalized spherical functions. SCIATRAN is available for public use.

3.1.3 SOSVRT

Made in 2009 by Duan Minzheng, the SOSVRT model is a plane parallel, fully polarized radiative transfer model (*Min et al.*, 2010). This model is based on the successive order of scattering technique and is able to compute polarization within a vertically inhomogeneous environment. To include polarization, SOSVRT utilizes the Stokes vector and the Fourier decomposition version of the phase matrix. In order to reduce the computation of not only the successive order of scattering technique, but also the inclusion of polarization several additional techniques were used within this model. These techniques include the truncation of the scattering order and the processing of angle interpolation. These additions have created a model that is highly accurate, especially in optically thin atmospheres (*Kokhanovsky*

et al., 2009). SOSVRT is not available to the public.

3.2 Three Dimensional Polarized Models

3.2.1 3DMCPOL

3DMCPOL is a three dimensional, monochromatic, fully polarized radiative transfer model (*Cornet et al.*, 2010). This model utilizes the forward Monte Carlo method with such techniques as the local estimator to maximize computational efficiency. Due to its three dimensional nature, 3DMCPOL is able to compute flux, and polarized radiance values for complex environments that include three dimensional clouds and a complex array of aerosols and molecules. In order to include polarization, 3DMCPOL included results for the vector representation of polarization, included a full phase matrix in computations and altered the selection of scattering and rotation angles. Due to the lack of polarized three dimensional radiative transfer solutions, 3DMCPOL was benchmarked using an adding and doubling model for plane parallel calculations and reflectance values (*Kokhanovsky et al.*, 2009). 3DMCPOL is currently not available for public use.

3.2.2 MYSTIC

MYSTIC (Monte-Carlo code for the phSYicaly correct tracing of photons in the Cloudy atmosphere) is one of the more well known and versatile radiative transfer models. Based on the forward Monte Carlo method, additions to this model have made it a very versatile polarized radiative transfer option. The flexibility of this model allows the user to choose between 1D, 2D, or 3D environments with scalar or vector computations. Also the model has been extended to a fully spherical geometry and it now even includes backward tracing (*Emde et al.*, 2010). Also, MYSTIC is able to handle a complex environment. This may include 3D clouds and inhomogenous surfaces with topography and unique albedos. Consid-

ering polarization, MYSTIC strives to reduce computational expense that is associated with polarization. Several different techniques are used to increase accuracy and computation time such as the local estimated and variance reduction technique for strongly peaked phase functions. The availability of this model has changed over time. MYSTIC is now included within the libRadtran package but the polarized radiative transfer model is limited to only the one dimensional version (*Mayer et al.*, 2011).

Chapter 4

Model Description - I3RC

4.1 Intercomparison of Three Dimensional Radiation Community Monte Carlo Model

4.1.1 Model Introduction and Motivation

Written by Robert Pincus with funding from the Department of Energy Atmospheric Radiation Measurement Program and NASA, the I3RC (Intercomparison of Three Dimensional Radiation Community Monte Carlo Model) provides an ideal base for the development of this polarized radiative transfer model. The I3RC is an open source, three dimensional, forward Monte Carlo model. Computed radiative quantities include upward flux at the top of the domain, downward flux at the bottom of the domain, radiance values leaving the top of the domain, domain average absorption profiles, residual flux absorbed in the domain, and the 3D distribution of flux divergence. All of these calculations may be performed over a wide range of environments created by the user. The versatility and flexibility of this model is directly related to the primary goals of the development of the I3RC. While much of the motivation of the I3RC is rooted in the comparison and benchmark of 3D radiative transfer codes, one of the main purposes was to provide a community model that can be used for atmospheric education and as a starting point for the creation of different radiative transfer tools (*Cahalan et al.*, 2005); (*Pincus and Evans*, 2009). This mentality can be seen as current alterations of the I3RC included the development of a broadband version, the addition of a BRDF surface, and our own polarized extension.

4.1.2 I3RC Programming Style

The style and framework of the I3RC allows for easy modifications and additions to this radiative transfer model. The I3RC is written in Fortran 95 using object oriented programming. Object oriented program splits up and assigns different parts of the program to an object. Development of new I3RC versions are easier due to the object oriented program's ability to create objects that are reusable within the model (*Pincus and Evans*, 2009). This concept of reusability can be seen when modifications need only to add to the definition of objects instead of creating brand new objects. For example, when modifying the scatteringPhaseFunction module the scattering phase matrix needed to be represented instead of the scattering phase function. Instead of creating a brand new object thus altering a larger amount of the program, the phase function object was extended to including the scattering phase matrix.

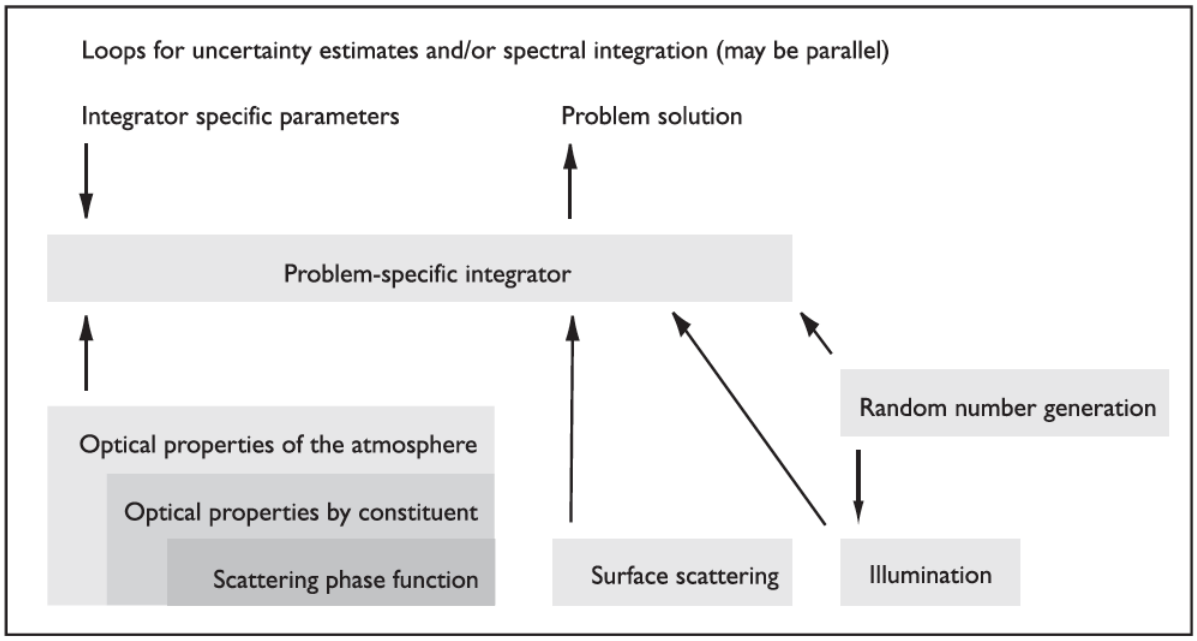

Figure 4.1: Demonstration of the interconnectiveness of each module within the I3RC (*Pincus and Evans*, 2009)

One of the most useful aspects of the I3RC's framework, is the dependency on separate modules. Instead of having one single program organizing, initiating, and calculating all

simulations, the I3RC is broken up into several different sections or modules each with its own individual role as seen in Figure 4.1(*Pincus and Evans*, 2009). Some module functions include the storage of optical properties including the phase function, the illumination of new photons, the selection of random numbers, and the performance of photon calculations. Many modules are dependent on additional modules to perform their respective tasks. This method not only provides an organized model, but it also allows modifications to be made by just updating and interchanging different modules.

4.1.3 User Defined Inputs

Domain files

Before simulations, the environment and initial settings is determined in the creation of a domain by the user. The domain is a three dimensional rectangular grid where the number of cells are determined by the users when creating the *domain*. Optical properties such as single scattering albedo, amount of extinction, and phase function are defined uniformly within each grid cell with in the domain.

Name List

The *name list* provides the user control over simulations calculated within the I3RC. Within the *name list*, different variables necessary for computation are supplied such as solar flux, incoming direction of solar radiation, surface albedo, and directions in which radiance calculations occur. The *name list* also prescribes necessary variables for the Monte Carlo simulations including seed number, the number of photons per batch, and finally the number of batches to be performed. The seed number is used in the module *RandomNumbers* to generate the random numbers selected within the Monte Carlo technique. The number of photons per batches and number of batches dictate the amount of photons used in simulations and the way in which they are distributed over different processors. Algorithm choices

and variance reduction techniques are also selected within the *name list*. Such options include photon tracing or the max cross section technique, the use of russian roulette, hybrid phase functions, and intensity contribution settings (*Pincus*, 2009), (*Pincus and Evans*, 2009). Finally, the user must supply the necessary input, domain files, and output path and names such as domain and output types. Once all settings have been made, the I3RC can begin its simulations.

I3RC Reference Frame

When creating the *name list*, the user must keep in mind the solar and view geometry reference frame that the I3RC utilizes. The zenith angle is defined from an upward normal, making the μ positive when traveling toward the top of the domain and negative when approaching the surface. The azimuth angle is also defined as clockwise when looking down.

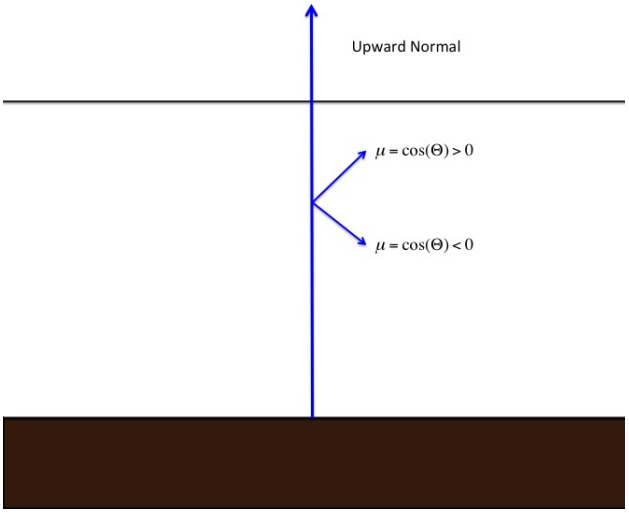

Figure 4.2: Zenith geometry

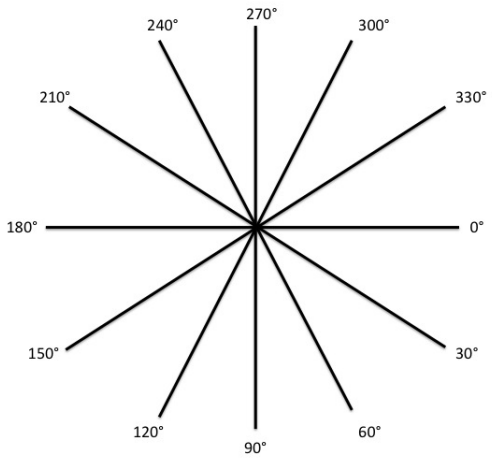

Figure 4.3: Azimuth geometry

4.2 Monte Carlo Radiative Transfer

4.2.1 Monte Carlo Basics

When deciding on whether to use a Monte Carlo model or when comparing results to other models, it is important to understand how this technique works. The Monte Carlo method is rooted in statistical processes such as probability and random numbers. This technique relies on algorithms that use random sampling to simulate results in calculations that are difficult to compute. In order to represent a numerical calculation, the Monte Carlo must:

1. Set a domain
2. Randomly select samples from a probability density function
3. Compare the random sample to a rule
4. Collect results

For an example of these steps, the computation of pi will be modeled using the Monte Carlo method:

1. Draw a circle within a square. Keep in mind that the ratio of these areas are $\frac{\pi}{4}$
2. Sprinkle grains of sand over the circle and square.
3. Does the grain fall within the circle or outside of it?
4. Based on ratio of the areas, π can be estimated by $\frac{4*(grains_{circle})}{(grains_{total})}$

The first step is to set up a domain in which calculations are simulated. This is accomplished when a circle is drawn within a square. Not only does this domain create an environment for calculations, but it also provided useful information. The ratio of area between a circle and square is $\frac{\pi}{4}$. This information can be used when collecting results. Next, samples must be selected from a probability density function. This is represented when sprinkling grains of sand over the domain. Since every grain of sand has the same probability of landing anywhere within the domain, this idea models sampling from a uniform distribution. Next, the grain must be compared to a rule set up by the user, for example counting

how many grains fell within the circle compared to outside the circle. This information is used when collecting results. By comparing the ratio of the areas, the number of grains that fell within the circle, and the number of grains used, π can then be approximated. A sample simulation of 3000 grains yields $\pi = 3.16667$. After 30,000 grains $\pi = 3.1436$. Notice that the more samples, the higher the accuracy. An approximation for this relationship was shown by Mayer (2009):

$$\sigma \approx \mu \frac{1}{N_s} \tag{4.1}$$

where σ is the standard deviation or error, μ is the mean simulated value, and N_s is the number of samples contributing to the solution. It is easy to see that the standard error is inversely proportional to the square root of the number of samples used. Therefore as error decreases as number of samples increases. Using this equation, the number of samples required for a certain accuracy can then be determined.

4.2.2 Monte Carlo Radiative Transfer

The Monte Carlo method utilizes the tracing of photons to calculate different radiative quantities. Strongly based on probability, each photon travels through the domain and encounters extinction via scattering and absorption. Flux, radiance, and absorption quantities are determined by adding the contributions of all photons propagating through the domain. The following section shows this process by explaining the propagation of a single unpolarized photon. For additional information on the Monte Carlo process and the I3RC, see the I3RC Programmer's guide (*Pincus*, 2009) and Mayer's paper (2009).

Photon Initiation

All photons are initialized as coming from the sun. There is no thermal emissions within the I3RC therefore all photons must start at the top of the domain. Each photon is assigned an initial direction according to the solar position in terms of azimuth and zenith angles. All

photons will have the same solar direction as specified by the user. The photon though will start at a different randomly chosen location at the top of the domain and given a weight of 1. As shown in the following sections, the weight is crucial to determine the photon's extinction.

The photon traveling

While the direction in which a photon will travel is known by either the specification of the solar angles or the random selection of the scattered angles, the distance the photon travels must be determined. This distance, initially represented by an optical depth, is selected randomly using a cumulative probability density functions based upon Beer's law. By selecting a random number (ρ), the optical depth ($\tau_{totravel}$) in which the photon will travel is expressed as:

$$\rho_{survival}(\tau) = exp(-\tau) \tag{4.2}$$

Since extinction and transmission are directly related, this law can help to explain how much extinction the photon encounters. This relationship between extinction and survival can be shown by using beer's law to examine the amount extinction that occurs through a certain optical depth. The survival of extinction has an equivalent form to the probability of extinction expressed as:

$$p_{extinction} = p_{survival}(\tau) - p_{survival}(\tau + d\tau) = -\frac{dp_{sur}}{d\tau}\, d\tau \tag{4.3}$$

$$p_{extinction} = exp(-\tau) \tag{4.4}$$

Next, random samples must be drawn. If these random samples were to be repeated over a wide range of times, the histogram of drawn optical thicknesses will equal the probability

density function. This method may be done by using the Von Neumann's Golden Rule of Sampling (*Mayer*, 2009). The result is a cumulative probability density function for the extinction of the photon seen in equation 4.5.

$$P_{extinction}(\tau) = \int_0^{\tau} p_{extinction}(\tau')\, d\tau' = 1 - exp(-\tau) \tag{4.5}$$

Finally by inverting the expression to be equal to optical depth, a random number, (ρ), can be used to calculate a random optical depth, ($\tau_{totravel}$), in which the photon will travel.

$$P_{extinction}(\tau) = \int_0^{\tau} p_{extinction}(\tau')\, d\tau' = 1 - \exp(-\tau) \tag{4.6}$$

$$\tau_{totravel} = P^{-1}_{extinction}(\rho) = -\ln(1-\rho) \tag{4.7}$$

The optical depth, ($\tau_{totravel}$), is used when physically moving the photon through the domain. As a photon travels in the specified direction, one cell at a time, the optical depth, ($\tau_{accumulated}$), accumulated will be added. Once the optical depth, ($\tau_{accumulated}$), added through the photon's movement within the domain equals the optical depth randomly selected, ($\tau_{totravel}$), propagation will stop. This is the location of the next scattering event.

Scattering and Absorption

A photon can experience extinction within the I3RC from scattering or absorption. The photon's weight, ranging from $[0-1]$, helps to represent the percent of the photon's energy not yet absorbed. This absorption is represented by multiplying the weight of the photon by the single scattering albedo at each scattering event. If the photon weight does not have a very small value, representing complete absorption, the photon will be then be scattered and will continue propagating.

Extinction may occur at both the surface and by particles within the domain. Currently

the I3RC only treats the surface as a Lambertian surface. When interacting with the surface, a photon may be scattered or absorbed. In order to represent what remains after absorption of the photon at the surface, the photon weight is simply multiplied by the surface albedo which is supplied by the user within the *name list*. Each absorption contribution to the surface flux is incremented by $(1 - A) *$ photon weight. Scattering also occurs at the surface. The photon contribution to intensity must be added as discussed in the following section. The photon is then scattered back into the upwelling direction of the domain. This direction is determined randomly due to the nature of a Lambertian surface.

Scattering may also occur due to interaction with particles in the atmosphere. Depending on the user's preferences, there may be several different particle types within the domain. The particle that does the scattering is calculated randomly based on the fraction contribution to the total extinction and the appropriate absorption and scattering will occur. Absorption is considered using the photon weight, this time using the single scattering albedo instead of the surface albedo. Also at the scattering event, intensity contributions are added for all angles specified. This process is described in detail in the following section.

If the photon still has a large enough weight value, then it will continue propagating throughout the atmosphere. It's new direction is determined using the inverse phase function and random numbers. This process will continue until the photon is absorbed completely, the photon weight is below some threshold, or the photon is scattered out of the domain. Once the photon leaves the top of the domain, upwelling flux contributions are incremented and if all photons have not been simulated, the next photon will be launched to experience the same absorption and scattering process.

Radiance and the Local Estimator

The calculation of radiance requires a photon to travel into an exact direction specified by the user in the *name list*. The manner in which many models using the Monte Carlo technique calculates radiance is by cone sampling. A cone that represents the direction in

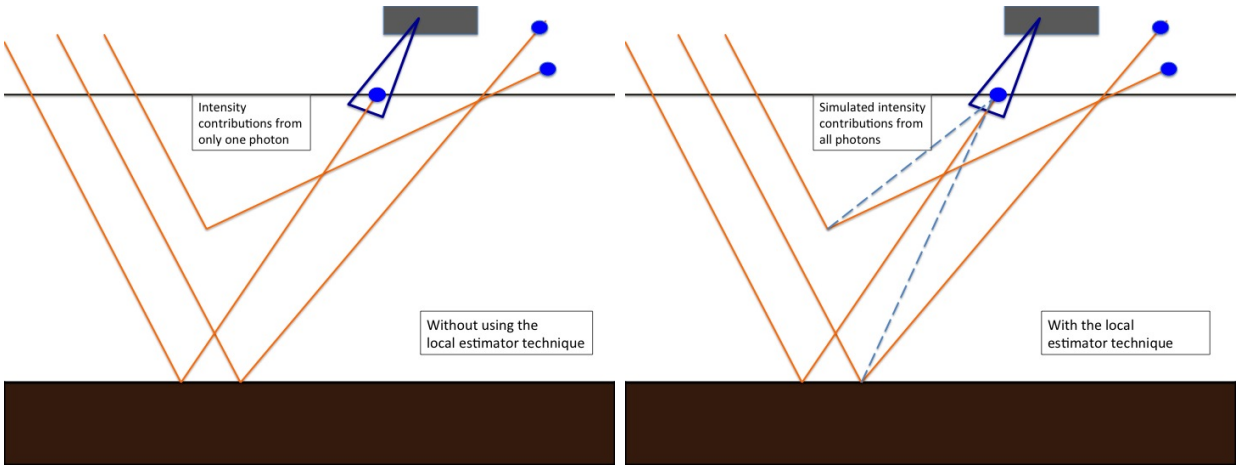

(a) Without Local Estimator (b) With Local Estimator

Figure 4.4: Different methods in simulating radiance values using the Monte Carlo technique.

which radiance will be calculated is added to the simulation. If a photon randomly scatters into this cone or "direction", the photon's contribution will be added to simulate the radiance values (Figure 4.4 a). This method though is not very computationally efficient. The chance that a photon will fall into the specific cone is small and therefore a large number of photons must be sampled in order to simulate radiance values.

In order to improve this computationally expensive method, the "local estimator" technique can be used. Instead of counting only a select few photons that fall within the specified cone, this variance reduction technique adds the contribution of each photon as if it were to hypothetically travel into the desired direction or cone (Figure **??**). This will decrease the amount of photons required for accurate results. Contributions from every photon at every scattering event can be added to represent the statistical estimation of radiance in a specific direction.

The representation and validity of this technique is rooted in the use of Nuemann Series which is derived in full by Marshak (1980). Mathematically, this process can be expressed by:

$$C(\mu,\phi) \approx \frac{1}{N}\sum_{k=1}^{N}\sum_{l=1}^{m}\omega_{kl}\frac{P(\Theta_{kl})}{4\pi\mu_{kl}}exp(-\tau_{kl}) \tag{4.8}$$

where $C(\mu, \phi)$ represents the fractional contribution of intensity. The contribution of a single photon at a single scattering event is based on several different components. The photon weight (ω) which represents the amount of energy the photon still has after previous extinction. The transmission ($exp(-\tau)$) takes into account the optical depth and amount of extinction that occurs between the location of the photon and the detector at the top of the atmosphere. The final component of the contribution is the normalized phase function ($\frac{P(\Theta)}{4\pi\mu}$), which represents the probability that the photon actually scattered into the direction of the detector where μ is the zenith angle of the detector. This contribution must then be summed over each scattering event *(M)* and each photon *(N)*. Finally, the contributions are normalized using the number of photons *(N)*. When multiplied by the solar flux, seen in Section 4.3.2, will represent the intensity in a certain direction with units of $\mathrm{Wm}^{-2}\mathrm{sr}^{-1}$.

4.2.3 Radiance and Irradiance Outputs

The final step in a Monte Carlo radiative transfer model is to compile the contributions of different outputs and apply physical meaning. Radiance and irradiance values are calculated by adding the contribution of each photon traveling through the domain. Flux calculations include upwelling, downwelling, and absorbed fluxes either domain averaged, column by column, or even pixel by pixel.

As the photon travels through the domain and encounters extinction, its contributions are collected for each photon and then added to the rest of the photons. The I3RC distributes photons over batches and processors, therefore the final summation must include all photons from every simulation. The total number of contributions is divided by the number of photons per column over all batches and processors, giving the representation of a fractional radiative value. Finally, each value must be multiplied by the solar flux to give the radiative value the correct physical units. For example, the mathematical representation of intensity becomes:

$$I(\mu,\phi) \approx \frac{1}{S}\frac{1}{R}\frac{1}{N}\sum_{i=1}^{S}\sum_{j=1}^{R}\sum_{k=1}^{N}\sum_{l=1}^{m}\omega_{ijkl}\frac{P(\Theta_{ijkl})}{4\pi\mu_{ijkl}}exp(-\tau_{ijkl}) * F_0 \tag{4.9}$$

where the summation over S represents the addition due to the different processors, R is the summation over batches, N is the summation of the photons per batch, and m is the summation over all scattering events per photon. Compared to equation 4.8, the only change is the total number of photons is not represent by a single total (N) but instead distributed over different processors *(S)* and batches *(R)*. Finally the contributions are multiplied by solar flux F_0 to give the radiance value units of $\mathrm{Wm^{-2}sr^{-1}}$.

The I3RC-POL also outputs statistical information such as standard error for each output. The mathematical representation of standard error within the I3RC can be expressed as follows (*Barker et al.*, 2003):

$$\sigma = \sqrt{\frac{\frac{1}{R}\sum_{r=1}^{R}(\rho_r^2) - (\frac{1}{R}\sum_{r=1}^{R}(\rho_r)^2)}{R}} \tag{4.10}$$

where σ is the standard error, R is the total number of batches, r represents a single batch, and ρ_r is the radiance estimates for batch number r. This output of the standard error provides valuable information on the validity of simulations and must be considered in all calculations.

Chapter 5

Polarized Model Implementation

Implementation of the I3RC-POL requires the alteration and or addition to many modules and subroutines within the original I3RC. The following describes the function and changes to each module. The I3RC-POL is currently stored on the Department of Atmospheric Science's Keeling cluster within the I3RC/POLARIZED folder. The specific directory in which the I3RC-POL may be found is /data/gdi/a/common/keeling. For further questions regarding modules not discussed in this section, refer to the I3RC's Programmers guide (*Pincus*, 2009).

5.1 Module *ScatteringPhaseFunction*

The module *scatteringPhaseFunction* is used to store the components necessary for a single scattering calculation including the scattering phase function, single scattering albedo, and extinction. The user via the domain file, must supply each component to be stored for different particle composition and sizes. There can be a wide range of values depending on the complexity and heterogeneity of the domain.

A majority of the module's role is to calculate and store the scattering phase function. The scattering phase function used in unpolarized simulations, can be supplied as values

corresponding to a certain scattering angle or as orthogonal Legendre polynomials. Users must choose which representation to allocate within the corresponding domain file. If requiring the value representation, users will supply each scattering angle and the associated scattering phase function. The module can then represent all scattering angles and phase function values by linearly interpolating between user supplied values. The Legendre polynomials $P_l(\cos\Theta)$, which is specified by the user within the domain files are then expressed as the following Legendre expansion (*Pincus*, 2009):

$$P_l(\cos\Theta) = \sum_{l=0}^{L}(2l+1)\chi_l P_l(\cos\Theta) \tag{5.1}$$

After the correct normalization, the phase function may be thought of as a probability of light being scattered into a given direction. The phase function normalization given the scattering angle (Θ) is:

$$\int_{-1}^{1} P(\cos\Theta)\, d\cos\Theta = 1 \tag{5.2}$$

Resulting phase functions are saved within the scattering table to be used in the netcdf domain file, having a size equivalent to the number of scattering angles and the number of different particles. The module also provides several tools that allows the user to utilize information from the table. Such features include copying the table, extracting information such as number of phase functions and descriptions of the table, or retrieving specific values of corresponding characteristics such as extinction or single scattering albedo. All of these tools are used within the integrator to complete the scattering of each photon. Again, it is important to note that the description of the phase function thus far does not consider polarization. In polarized calculations, the phase function is no longer treated as a single value. Instead, polarization utilizes the scattering phase matrix which considers both the energy and polarization of a wave. This implementation requires that all scalar values must be treated as a 4x4 array.

The initial change is the addition of variables within the type *phaseFunction*. The option of storing the phase function in a single array or Legendre coefficients are extended to storing information in four new arrays corresponding to each unique element of the scattering phase matrix. This allows the treatment of the object phaseFunction to be used in both the polarized or scalar version. Once initiated, the user may specify whether their scattering phase function will be scalar values, Legendre polynomials, or the full matrix values. In doing so, module *scatteringPhaseFunctions* will follow a set flow of subroutines. These additional subroutines now reflect the polarized extension. Treatment of the single scattering albedo and extinction remain unchanged.

Within the file that creates the domain, the user must now specify the scattering angles and tabular value of $P_{11}(\Theta)$, $P_{12}(\Theta)$, $P_{33}(\Theta)$, and $P_{34}(\Theta)$ portions of the scattering phase matrix. The polarized table will be stored in the domain and utilized by the integrator when calculating the full vector representation.

The following subroutines and functions were added to the module *scatteringPhaseFunctions*. Note that these description use the term phase function object and table. This is the arbitrary title of the objects within the module. Again, the objects and tables have been extended to include the scattering phase matrix:

- ***newPhaseFunctionPolarized***

  Creates a new phase function object that includes all components of the scattering phase matrix.

- ***newPhaseFunctionTablePolarized***

  Initiates a new table of scattering phase matrix values based upon the number of scattering angles and the corresponding scattering phase matrix values.

- ***getPhaseFunctionValuesPolarized_one***

  Retrieves the scattering phase matrix for a single scattering angle from the table of scattering phase matrix values.

- ***getPhaseFunctionValuesPolarized_table***

  Returns the values of the scattering phase matrices in a table given a series of scattering angles.

- ***storedAsPolarized***

  Distinguishes the use of the scattering phase matrix representation of the phase function within the module and resulting table.

Each function follows the same procedure as the scalar versions but utilizes the four arrays for a phase matrix instead of a singe value. In addition, the follow subroutines were extended to allow the polarized option:

- ***newPhaseFunctionTabulated***

  Initiates the creation of the phase function or matrix table by allocating arrays, setting logical statements, and checking inputted values for possible errors such as negative phase functions, array lengths, and bounds of the scattering angle.

- ***newPhaseFunctionExpansion***

  Creates a phase function table based upon legendre coefficients. Additions were added to this subroutine to ensure the phase matrix was defined using the tabular method.

- ***newPhaseFunctionTableTabulated***

  Creates a phase function table based upon the tabular technique. Additions insured this table represents all components of the scattering phase matrix instead of just a single value of the phase function.

- ***copy_PhaseFunction***

  Makes a copy of a single scattering phase function and now a single scattering phase matrix

- ***copy_PhaseFunctionTable***

  Makes a copy of the phase function table which can now include phase matrices.

- ***isReady_phaseFunction***

  Determines if a phase function object is ready to be used.

- ***getInfo_PhaseFunction***

  Retrives information regarding the phase function table such as whether the phase function is specified by legendre coefficients, tabulated scattering phase matrix values, or tabulated scattering phase matrix values.

- ***add_PhaseFunctionTable***

  This tool has the ability to add an additional phase function table to an external file. The polarized extension of the phase function is now included.

- ***read_PhaseFunctionTable***

  Reads a phase function table from an external file. This ability is extended to include variables and arrays associated to the scattering phase matrix.

- ***finalize_PhaseFunction***

  Used to free memory and pointers after the phase function object has been made.

- ***finalize_PhaseFunctionTable***

  Used to free memory and pointers after the phase function table has been made.

5.2 *Module InversePhaseFunction*

The selection of the scattering angle within the photon simulations is simplified by the *inverseScatteringAngle* module. As derived in the Section 5.4.7, the selection of a scattering angle is dependent on the cumulative distribution function derived from the scattering phase function $P(\Theta)$.

$$C = \int_0^{\Theta} \tilde{P}(\Theta)\, d\Theta \tag{5.3}$$

Instead of calculating the cumulative distribution function for every scattering event, *inversePhaseFunction* creates a table of cumulative distribution function based upon the

phase functions within the domain file. Whenever the integrator needs to select a scattering angle, the table calculated by*inversePhaseFunction* is referenced. Since polarization's selection of the scattering angle uses the same strategy as the unpolarized case, *inverseScatteringAngle* remains relatively the same. The main implementation uses the $P_{11}(\Theta)$ value of the scattering phase matrix instead of the scalar phase function in unpolarized cases.

5.3 *Driver*

The *Driver* program is fundamental to the radiative transfer simulations. The *Driver* is able to initiate the simulation by reading in information from the name list and thus organizes the simulation. Inputs can include solar directions, intensity directions, seed number, the number of photons or batches, output, and input files. The environment in which the model is to perform is defined by the user in the domain files. The Driver is able to access this information set up the atmosphere and surface accordingly. Prior to beginning calculations throughout this environment, arrays of radiative outputs and their corresponding statistical information must be created for both flux and intensity. These arrays are allocated and zeroed. The *Driver* finally spreads the number of photon batches across all processors.

After all the environments and settings are defined within the *Driver*, actual calculations can begin. The Driver calls computeRadiativeTransfer within the integrator module to begin computing the radiative quantities. While calculations occur within the integrator, the *Driver* organizes and processes the outputs by calculating statistical information such as mean and standard error. Results are then reported by the *Driver* in either a netcdf or ASCII file.

The addition of polarization requires the functions of the *Driver* to include polarized intensity calculations. The *name list* was expanded to included a *usePolarization* logical statement which activates all polarized calculations. Not only must this logical be read into the *Driver*, but once activated all *Driver* settings and calculations must represent polariza-

tion. Polarized output arrays such as intensityStokesI, intensityStokesQ, intensityStokesU, intensityStokesV, and their corresponding statistical calculations must be allocated and zeroed. These statistical arrays such as standard error and mean intensity representation of outputs must also include the four intensity components of polarization. Finally, output files were also expanded to incorporate polarized calculations.

5.4 Module *MonteCarloRadiativeTransfer*

Module *MonteCarloRadiativeTransfer* contains the majority of the computations required for intensity calculations. The step by step tracing of each photon is described within the model description chapter and the *computeRT* subroutine (Section 5.4.7). Several vital calculations must be changed to represent polarized radiative transfer including representation and rotation of the Stokes vector, implementation of the scattering, and angle selection via the rejection method. These changes are broken up into subroutines that are used to set up the integrator and subroutines utilized in the actual calculations.

5.4.1 Object Definitions

The integrator object stores the information about the atmosphere necessary for calculations. In order to calculate polarized radiative transfer, the integrator needed to extend its array declarations to account for polarization. This additional arrays include but are not limited to the additional components of the scattering phase matrix, intensity outputs for each variable of the Stokes vector, and excess storage variables. By not replacing the integrator type, only adding to it, much of the module *monteCarloRadiativeTransfer* can be kept intact for polarized calculations.

5.4.2 Subroutine *TabulateForwardPhaseMatrix*

Using tools developed in the module *scatteringPhaseFunction*, subroutine *tabulateForward-PhaseMatrix* retrieves scattering phase matrix values stored within the domain netcdf file. Stored as separate arrays of $P_{11}(\Theta)$, $P_{12}(\Theta)$, $P_{33}(\Theta)$, and $P_{34}(\Theta)$ values. From these arrays, tables and/or individual phase matrices can be compiled using the *lookUpPhaseMatrices* subroutines.

5.4.3 Subroutine *Copy_Integrator* and Subroutine *Finalize_Integrator*

The *copyIntegrator* and *finalizeIntegrator* subroutines are used to replicate the integrator object. Polarized arrays are added to these subroutines by including the tabulated scattering phase matrix arrays, tables created in the *inversePhaseFunction* subroutine to select the scattering angle based on the $P_{11}(\Theta)$ component of the scattering phase matrix, and the intensity arrays for the four different components of the Stokes vector.

5.4.4 Subroutine *SpecifyParameters*

Subroutine *specifyParameters* helps to set up the calculations that the integrator performs. Several logical statements are used to activate such calculation strategies such as the use of ray tracing or max cross section algorithms, whether the integrator will compute intensity, or whether the integrator will use the russian roulette technique. For more information regarding these calculations, refer to the programmers guide (*Pincus*, 2009). A logical statement is also defined so that the integrator knows to simulate polarization. If the user's simulation is polarized then this logical is set to true and the vector radiative transfer is calculated instead of scalar.

5.4.5 Function *Flatten*

Subroutine *Flatten* provides a powerful tool, not originally implemented in the I3RC, that protects the bounds of trigonometric functions used. Many of the calculations within the I3RC-POL require the use of the arc cosines often on numbers very close to 1. Due to the single precision nature of the I3RC-POL, numbers equal to 1 may actually be stored as a value slightly larger, such as 1.0000002. While this addition may seem insignificant, this value is outside the arc cosine function's limits and will stop computations. *Flatten* was implemented to insure these extra decimal points will not be added by setting values slightly greater than 1 or slightly less than -1 to exactly the value of $(+/-)$ 1 respectively. Each call to a trigonometric function will proceed through *flatten* first to ensure the user's computation may continue without any segmentation faults or NAN values.

5.4.6 Subroutine *ComputeRadiativeTransfer*

The subroutine *computeRadiativeTransfer* processes the radiative transfer calculations for a batch of photons. Necessary initiations include the allocation of variables such as intensity storage or phase function values, position of photons, and types of calculations such as flux or intensity. Once the photon is set up to proceed through the domain, *computeRT* is called to complete the ray tracing. Finally, within *computeRadiativeTransfer* the flux, absorption, and intensity results are normalized by number of photons per column.

Polarized calculations must be initiated in this subroutine. Once the subroutine recognizes that this simulation will be polarized, the computeIntensity logical statement is activated and polarized intensity arrays are allocated. These allocations include the zeroing of the intensity arrays for each stokes component and the tabulation of the inverse phase function and forward scattering phase matrix depending of the atmosphere. *ComputeRT* will then be called and intensity values will be calculated.

5.4.7 Subroutine *ComputeRT*

ComputeRT propagates the photon, calculates the flux, and passes the photon to the local estimator to determine intensity values. Depending on the user's preference, computations may either be completed by the ray-tracing Monte Carlo algorithm or the maximum cross-section algorithm (*Marchuk et al.*, 1980). Reference Chapter 4 for specific scalar photon treatment.

Polarization calculations require the photon to be treated as a Stokes vector instead of a single scalar value. When initiating a photon at the top of the domain, polarized calculations will assign an unpolarized Stokes vector to every photon. Due to the incoming solar radiation's unpolarized nature, each photon will be initiated with a value of:

$$\text{stokes}_0 = \begin{pmatrix} 1 \\ 0 \\ 0 \\ 0 \end{pmatrix} \tag{5.4}$$

As a photon travels it may experience a scattering event, where extinction due to scattering and absorption are considered. The absorption process is modeled using the single scattering albedo. This method is consistent between the polarized and unpolarized I3RC. Prior to propagating the photon into a new direction, the Stokes vector must be updated and the direction of propagation will be determined by the rejection method as seen in the following section. At each scattering event, the Stokes vector must represent the scattering that is occurring, which is represented by the phase matrix described in Section 2.3. It is important to note that photon extinction with *computeRT* only considers absorption using the photon weight (ω) and the single scattering albedo (ω_0).

$$\omega = (1 - \omega_0) * \omega \tag{5.5}$$

In the unpolarized version of the I3RC, the photon weight does not change due to scattering and the phase function value within computeRT. Instead, within computeRT, the only change in photon weight is due to absorption. To add contributions due to scattering, the local estimator in the subroutine *computeIntensityContribution* is used. The Stokes vector's radiance value or weight is then only influenced by absorption within *computeRT* which does include scattering events in which the polarization can be influenced. Therefore the phase matrix used within *computeRT* is normalized by $P_{11}(\Theta)$ to ignore the loss radiance but still represent the change in polarization:

$$\text{Normalized Scattering Phase Matrix} = \begin{pmatrix} 1 & \frac{P_{12}(\Theta)}{P_{11}(\Theta)} & 0 & 0 \\ \frac{P_{12}(\Theta)}{P_{11}(\Theta)} & 1 & 0 & 0 \\ 0 & 0 & \frac{P_{33}(\Theta)}{P_{11}(\Theta)} & \frac{P_{34}(\Theta)}{P_{11}(\Theta)} \\ 0 & 0 & \frac{-P_{34}(\Theta)}{P_{11}(\Theta)} & \frac{P_{34}(\Theta)}{P_{11}(\Theta)} \end{pmatrix} \tag{5.6}$$

For simplicity, the compilation of the scattering matrix including the computation of rotation angles and phase matrices are completed by a separate subroutine *makeScattMatrix*. Intensity values are also calculated through the local estimator. Instead of only supplying photon weight and direction of propagation, the polarization calculations will also provide the Stokes vector to the local estimator.

Selection of Scattering Angles

As described in the previous section, the photon arrives at the scattering event and experiences some extinction due to absorption then is scattered into the next direction. In order to determine the new direction of propagation, scattering and rotation angles must be determined. One of the most fundament changes due to polarization is the process of selecting these angles. This selection is based upon the phase function of polarized radiance determined by the rotation and scattering of a Stokes vector (*Tynes et al.*, 2001):

$$\begin{pmatrix} I \\ Q \\ U \\ V \end{pmatrix} = \begin{pmatrix} 1 & 0 & 0 & 0 \\ 0 & \cos(2i_2) & \sin(2i_2) & 0 \\ 0 & -\sin(2i_2) & \cos(2i_2) & 0 \\ 0 & 0 & 0 & 1 \end{pmatrix} \begin{pmatrix} P_{11}(\Theta) & P_{12}(\Theta) & P_{13}(\Theta) & P_{14}(\Theta) \\ P_{21}(\Theta) & P_{22}(\Theta) & P_{23}(\Theta) & P_{24}(\Theta) \\ P_{31}(\Theta) & P_{32}(\Theta) & P_{33}(\Theta) & P_{34}(\Theta) \\ P_{41}(\Theta) & P_{42}(\Theta) & P_{43}(\Theta) & P_{44}(\Theta) \end{pmatrix} \times \begin{pmatrix} 1 & 0 & 0 & 0 \\ 0 & \cos(2i_1) & \sin(2i_1) & 0 \\ 0 & -\sin(2i_1) & \cos(2i_1) & 0 \\ 0 & 0 & 0 & 1 \end{pmatrix} \begin{pmatrix} I_0 \\ Q_0 \\ U_0 \\ V_0 \end{pmatrix} \tag{5.7}$$

Note that the representation of i_1 and i_2 within the phase matrix are defined in equation 2.50. In this section, just the variables i_1 and i_2 are considered arbitrary rotation angles without a specific clockwise or counterclockwise direction. Given this scattering, the intensity component of the Stokes vector becomes:

$$\begin{aligned} I = P_{11}(\Theta)I_0 + P_{12}(\Theta)(Q_0\cos(2i_1) + U_0\sin(2i_1)) \\ + P_{13}(\Theta)(-Q_0\sin(2i_1) + U_0\cos(2i_1)) + P_{14}(\Theta)V_0 \end{aligned} \tag{5.8}$$

Using the proportionality relationship between the phase function and radiances, $I \propto P(\Theta, i_1)I_0$, the amount of intensity into a certain scattering angle (Θ) with a rotation (i_1) is represented as:

$$\begin{aligned} I_0P(\Theta, i_1) = P11(\Theta)I_0 + P12(\Theta)(Q_0\cos(2i_1) + U_0\sin(2i_1)) \\ + P13(\Theta)(-Q_0\sin(2i_1) + U_0\cos(2i_1)) + P14(\Theta)V_0 \end{aligned} \tag{5.9}$$

As seen in equation 5.9, the scattering of the incident, polarized, intensities is based upon the rotation angle (i_1), which is again the rotation angle from the incident meridian

plane into the scattered plane, and the scattering angle (Θ). Due to this bivariate nature, the selection of the scattering angle and associated rotation angle must be treated carefully. The following sections will use equation 5.9 to derive the method in which the scattering and rotation angles are selected.

Scattering Angle Selection

As previously discussed, the scattering of the polarized radiance values which is proportional to the polarized phase function $P(\Theta, i_1)$, is dependent on two angles. In order to randomly select both angles, the scattering angle must be selected using a univariate distribution and will then be utilized in the selection of the corresponding rotation angle. In doing so, a univariate distribution, $P(\Theta)$, must be derived where $i_1 : [0, 2\pi]$ and $\Theta : [0, \pi]$:

$$I_0 P(\Theta) = I_0 \int_0^{2\pi} P(\Theta, i_1) \partial i_1 \tag{5.10}$$

After completing the integral and dividing by I_0, the phase function becomes:

$$P(\Theta) = 2\pi (P_{11}(\Theta) + \frac{V_0}{I_0} P_{14}(\Theta)) \tag{5.11}$$

The scattering angle (Θ) is then selected from a cumulative distribution function based upon the normalized unconditional probability, the phase function $P(\Theta)$, so that $\int_0^{\pi} P(\Theta)\, d\Theta = 1$. It is important to note, that within the I3RC-POL, only spherical particles are considered, making $P_{14}(\Theta) = 0$. This simplifies equation 5.11 to the unpolarized phase function:

$$P(\Theta) = 2\pi P_{11}(\Theta) \tag{5.12}$$

In this case, since spherical particles are used, the manner in which the I3RC-POL selects the scattering angle is equivalent to the original I3RC's method. The cumulative distribution function for the selection of the scattering angle is again:

$$C(\Theta) = \int_0^{\Theta} \tilde{P}(\Theta)\, d\Theta = \frac{\int_0^{\Theta} P(\Theta)\, d\Theta}{\int_0^{\pi} P(\Theta)\, d\Theta} \tag{5.13}$$

where the normalized phase function is represented as:

$$\tilde{P}(\Theta) = \int_0^{\Theta} P(\Theta)\, d\Theta = 1 \tag{5.14}$$

This function, $C(\Theta)$, may be used in the unconditional probability of scattering to select a scattering angle (Θ) using a random number r $\in [0:1]$ so that $C(\Theta) = r$. The polarized version of the I3RC utilizes this method for the selection of the scattering angle (Θ).

Rotation Angle Selection and the Rejection Method

Given that the scattering angle (Θ) has been selected, the rotation angle can then be provided using a conditional probability and the rejection method. The derivation for this process begins with the definition of the condition probability $p(X|Y) = \frac{p(X,Y)}{p(Y)}$ (*Tynes et al.*, 2001). In this specific case, the conditional probability will be defined as:

$$P(i_1|\Theta) = \frac{P(\Theta, i_1)}{P(\Theta)} \tag{5.15}$$

where $P(\Theta, i_1)$ is given by 5.9 after normalizing by I_0. $P(\Theta)$ is also derived in the previous section, equation 5.11, making the conditional probability: .

$$\begin{aligned} P(i_1|\Theta) = \frac{1}{(2\pi(P_{11} + \frac{V_0}{I_0}P14))}(P_{11}(\Theta) + P_{12}(\Theta)(\frac{Q_0}{I_0}\cos(2i_1) + \frac{U_0}{I_0}\sin(2i_1)) \\ + P_{13}(\Theta)(-\frac{Q_0}{I_0}\sin(2i_1) + \frac{U_0}{I_0}\cos(2i_1)) + P_{14}(\Theta)\frac{V_0}{I_0}) \end{aligned} \tag{5.16}$$

This expression must also be normalized by the maximum value of P given a scattering angle (Θ). This prevents the rejection method to chose a value over 1. The normalization

factor can be computed by differentiating $P(i_1|\Theta)$ and setting it equal to zero.

$$\frac{\partial P(i_1|\Theta)}{\partial i_1} = 0 \tag{5.17}$$

When using equation 5.16, this becomes:

$$\begin{aligned}\frac{\partial}{\partial i_1}(\frac{1}{(2\pi(P_{11}+\frac{V_0}{I_0}P14))}(P_{11}(\Theta)+P_{12}(\Theta)(\frac{Q_0}{I_0}\cos(2i_1)+\frac{U_0}{I_0}\sin(2i_1)) \\ + P_{13}(\Theta)(-\frac{Q_0}{I_0}\sin(2i_1)+\frac{U_0}{I_0}\cos(2i_1))+P_{14}(\Theta)\frac{V_0}{I_0})) = 0\end{aligned} \tag{5.18}$$

Through this derivative and cancelation of terms, the normalization factor P_{max} can be derived as:

$$P_{max}(i_1|\Theta) = \frac{P11 + [(P11^2+P13^2)(U_0^2+V_0^2)]^{\frac{1}{2}}\frac{1}{I_0} + P14\frac{V_0}{I_0}}{2\pi(P11+P14)\frac{V_0}{I_0}} \tag{5.19}$$

Given this calculated normalization factor, the point rejection technique can be completed. The normalized conditional probability, $\tilde{P}$, can now be defined given $P(i_1|\Theta)$ and P_{max}, where $\tilde{P} \in [0:1]$.

$$\tilde{P}(i_1|\Theta) = \frac{P(i_1|\Theta)}{P_{max}} \tag{5.20}$$

$$\tilde{P}(i_1|\Theta) = \frac{1+\cos 2i_1(\frac{P12}{P11}\frac{Q_0}{I_0}+\frac{P13}{P11}\frac{U_0}{I_0})+\sin 2i_1(\frac{P12}{P11}\frac{U_0}{I_0}-\frac{P13}{P11}\frac{Q_0}{I_0})+\frac{P14}{P11}\frac{V_0}{I_0}}{1+\frac{\sqrt{(P11^2+P13^2)}\sqrt{Q_0^2+U_0^2}}{P_11I_0}+\frac{P14}{P11}\frac{V_0}{I_0}} \tag{5.21}$$

If the particles are randomly oriented, the particle orientation is distributed uniformly, and mirror-symmetric counterparts are presented in equal numbers then the scattering phase

matrix and the conditional probability both reduce to a simpler form.

$$P(\Theta) = \begin{pmatrix} P_{11}(\Theta) & P_{12}(\Theta) & 0 & 0 \\ P_{12}(\Theta) & P_{11}(\Theta) & 0 & 0 \\ 0 & 0 & P_{33}(\Theta) & P_{34}(\Theta) \\ 0 & 0 & -P_{34}(\Theta) & P_{34}(\Theta) \end{pmatrix} \tag{5.22}$$

$$\tilde{P}(i_1|\Theta) = \frac{1 + \frac{P12}{P11}\frac{Q_0}{I_0} cos2i_1 + \frac{P12}{P11}\frac{U_0}{I_0} sin2i_1}{1 + \sqrt{(Q_0^2 + U_0^2)^2}\frac{|P12|}{P11}} \tag{5.23}$$

Using this assumption within the I3RC-POL and equation 5.23, the rejection method can be utilized to determine rotation angle (i_1) using this conditional probability factor and a series of random numbers. First a random number is selected to determine a value from the normalized $\tilde{P}(i_1|\Theta)$. A second random number is then selected and if the second random number is larger than the value from $\tilde{P}(i_1|\Theta)$, then the selection is rejected. This process is repeated until a random number is smaller than that of the randomly selected $\tilde{P}(i_1|\Theta)$ value. Again prior to this step, the scattering angle must be correctly selected from the cumulative distribution function based upon unconditional probability previously derived. The scattering angle will then be used to determine the photons new direction while the rotation angle selected will become the rotation angle between the initial meridian plane and the scattering plane. This rotation angle will be utilized when computing the scattering matrix for the photon's scattering into its new direction of propagation.

5.4.8 Subroutine *ComputeIntensityContribution*

ComputeIntensityContribution utilizes the local estimator technique to determine intensity values at a certain direction. As previously discussed in Chapter 4, this technique reduces the number of photons necessary for raditative transfer calculations by adding the contributions

of an imaginary photon into a specified direction. The contribution calculation provides the main difference between the polarized and scalar version. The new contribution per photon is represented by:

$$contribution = \omega * exp(-\tau) * \frac{Z(\mu, \phi; \mu', \phi')}{4\pi\mu} * \begin{pmatrix} I \\ Q \\ U \\ V \end{pmatrix} \tag{5.24}$$

$$\omega = \text{Photon weight} \tag{5.25}$$

$$\exp(-\tau) = \text{Transmission between the photon and detector} \tag{5.26}$$

$$\frac{Z(\mu, \phi; \mu', \phi')}{4\pi} = \text{Normalized phase matrix} \tag{5.27}$$

$$\mu = \text{Cosine of the viewing zenith angle} \tag{5.28}$$

$$\begin{pmatrix} I \\ Q \\ U \\ V \end{pmatrix} = \text{Stokes vector} \tag{5.29}$$

The contributions are added, as seen in Section 4.2.2, after each photon by adding the four Stokes components of each photon. The contribution will be added together to calculate a final value for intensity. For polarization the result will be 4 separate contributions, one for each Stokes vector component. These contributions are outputted and processed within the *computeRadiativeTransfer* subroutine and the *Driver* program of the I3RC-POL.

5.4.9 Subroutine *LookupPolarizedPhaseMatFromTable*

The subroutine *lookupPolarizedPhaseMatFromTable* organizes the separate scattering phase matrix component arrays, P_{11}, P_{12}, P_{33}, and P_{34}, into a table of full scattering phase matrices. Originally these scattering phase matrix component arrays were supplied from the domain using the subroutine *TabulatedForwardPhaseMatrix*. The subroutine *lookupPolarizedPhase-MatFromTable* compiles the individual arrays and creates a scattering phase matrix for each scattering angle, (Θ) , supplied in the form of:

$$P(\Theta) = \begin{pmatrix} P_{11}(\Theta) & P_{12}(\Theta) & 0 & 0 \\ P_{12}(\Theta) & P_{11}(\Theta) & 0 & 0 \\ 0 & 0 & P_{33}(\Theta) & P_{34}(\Theta) \\ 0 & 0 & -P_{34}(\Theta) & P_{34}(\Theta) \end{pmatrix} \tag{5.30}$$

If the scattering angle required does not have a value originally supplied by the user, the corresponding scattering phase matrix values will be interpolated linearly. These scattering phase matrix values, for each scattering angle, are stored in a table.

5.4.10 Subroutine *LookUpSinglePhaseMatFromTable*

The phase matrices are now fully set up and stored as a function of angle, from the subroutine *lookupPolarizedPhaseMatFromTable*. A scattering angle is then supplied to the subroutine and the single corresponding phase matrix will be outputted.

5.4.11 Subroutine *MakeScattMatrix*

This subroutine calculates the phase matrix for a certain rotation angle in, rotation angle out, and the scattering phase matrix for a specific scattering angle. This single matrix is used when rotating the stokes vector at a scattering event or within the local estimator. The calculation is as follows:

$$Z = L(\pi - i_2)P(\Theta)L(-i_1) \tag{5.31}$$

$$\begin{pmatrix} I \\ Q \\ U \\ V \end{pmatrix} = \begin{pmatrix} 1 & 0 & 0 & 0 \\ 0 & \cos(2i_2) & \sin(2i_2) & 0 \\ 0 & -\sin(2i_2) & \cos(2i_2) & 0 \\ 0 & 0 & 0 & 1 \end{pmatrix} \begin{pmatrix} P_{11}(\Theta) & P_{12}(\Theta) & 0 & 0 \\ P_{12}(\Theta) & P_{11}(\Theta) & 0 & 0 \\ 0 & 0 & P_{33}(\Theta) & P_{34}(\Theta) \\ 0 & 0 & -P_{34}(\Theta) & P_{34}(\Theta) \end{pmatrix} \times \begin{pmatrix} 1 & 0 & 0 & 0 \\ 0 & \cos(2i_1) & \sin(2i_1) & 0 \\ 0 & -\sin(2i_1) & \cos(2i_1) & 0 \\ 0 & 0 & 0 & 1 \end{pmatrix} \tag{5.32}$$

The rotation angles (i_1) and (i_2) are initially computed in terms of $\cos(i)$ within subroutines *rotationAnglein* and *rotationAngleOut*. Prior to entering subroutine *makeScattMatrix*, the inverse cosine of these values are taken so they may be properly supplied and used within the phase matrix.

5.4.12 Subroutine *RotationAnglein*

The first rotation angle for each scattering event is computed within this subroutine. This angle represents the rotation between the initial meridian plane and the scattering plane. The equation for this angle, derived in Section 2.2.3, is again dependent on the incoming (θ', ϕ') and outgoing direction (θ, ϕ) of propagation.

$$\cos(i_1) = \frac{\mu - \mu' \cos(\Theta)}{\pm\sqrt{1-\mu^2}\sqrt{1 - cos(\Theta)^2}} \tag{5.33}$$

Note that this subroutine is only called within the *computeIntensityContributions* sub-

routine, and not in the *computeRT* subroutine. In the actual scattering of the photon, represented within the computeRT subroutine, the rotation angle between the meridian plane and the scattering plane is selected using the rejection method. Within the *computeIntensityContributions*, the incoming and outgoing directions are provided thus the scattering and rotation angles are not selected. The rotation angle needs to then be calculated by the subroutine *rotationAnglein*.

5.4.13 Subroutine *RotationAngleOut*

The subroutine *rotationAngleOut* supplies the final rotation angle between the scattering plane into the new meridian plane. The rotation angle is also dependent on the incoming (θ', ϕ') and outgoing direction (θ, ϕ) and as seen in Section 2.2.3, the sign of the angle is directly related to the difference in the incoming and outgoing azimuth angles.

$$\cos(i_2) = \frac{\mu' - \mu\cos(\Theta)}{\pm\sqrt{1-\mu'^2}\sqrt{1-cos(\Theta)^2}} \tag{5.34}$$

5.4.14 Subroutine *ReportResults*

Subroutine *reportResults* describes the final results of the simulation done by the I3RC-POL. Prior to reporting the results, this subroutine checks that outputs have been associated and are the correct size. A user's simulation may require different outputs therefore the subroutine *reportResults* must contain all possible results. In order to supply the user the option of polarized outputs, *reportResults* must be updated to report the different calculated components of the Stokes vector.

Chapter 6

Results

6.1 Benchmarking Strategy

There are several different types of tests that can be used to benchmark a polarized radiative transfer model. These strategies include a comparison of:

- Energy conservation
- Reciprocity relationships
- Analytical solutions
- Alternate code comparison

When benchmarking a 1D radiative transfer model, energy conservation, reciprocity, and code inter comparison can all be used. Analytical solutions though are limited to very simple, single scattering dominated cases. Yet this limitation does not effect the ability to benchmark one dimensional radiative transfer models due to the large amount of available benchmarking tools (*Kokhanovsky et al.*, 2009). The initial benchmarking of the I3RC-POL concentrates on unpolarized and polarized one dimensional simulations. In an unpolarized simulation, reciprocity and alternate code comparison is emphasized when benchmarking against the I3RC-POL. In polarized benchmarking, the analytical strategy is used. Coulson's tabulated results provides an analytical solution for 1D, polarized radiative transfer in a Rayleigh atmosphere over different optical depths and angles (*Coulson et al.*, 1960). These tables

have further been updated by Natraj (2009). While these preliminary benchmarking tests are limited, the results have thus far given an accurate representation of the I3RC-POL's current state of validity.

Benchmarking a three dimensional polarized model has its challenges. Returning to the list of possible benchmark strategies, the selection that may be used in this 3D polarized case is limited. Energy conservation is the only strategy that can be utilized. While reciprocity has been proven to work in 3D radiative transfer cases (*Girolamo*, 2002), this relationship has yet to be developed for polarized 3D radiative transfer. Also, there are no analytical solutions or available models to benchmark against. Therefore more resources for the benchmarking of 3D polarized radiative transfer must be developed. One suggestion includes the organization of a community inter comparison of three dimensional polarized radiative transfer models similar to the original I3RC concept. This may provide the necessary missing tool in the three dimensional benchmark process.

6.2 Main Types of Benchmark Testing

6.2.1 Envelope Testing

The first type of benchmarking performed on the I3RC-POL is envelope testing. Monte Carlo's dependency on random samples creates outputs that are often very noisy. This noise may become insignificant though after a large number of iterations. By using envelope testing, not only are the number of samples required to ignore this noise determined but also the validity of benchmarking results as seen using a simplified cartoon in figures 6.1 and 6.2

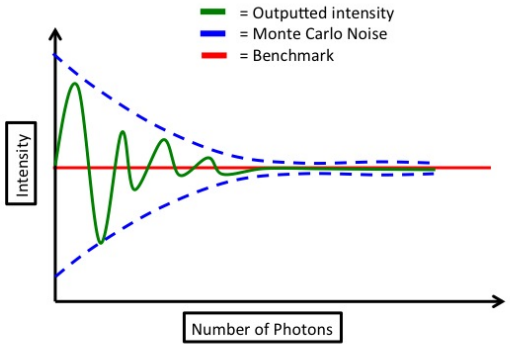

Figure 6.1: Expected Envelope Testing

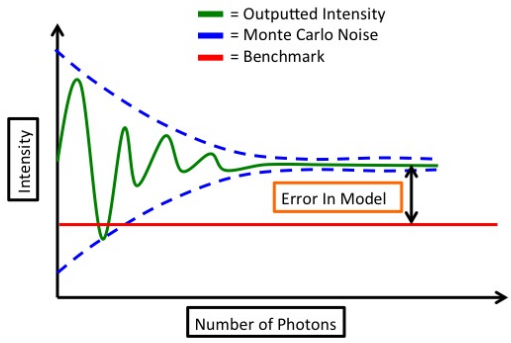

Figure 6.2: Envelope Testing with Model Error

These cartoon schematics show outputted intensity values and their corresponding standard error over a number of photons. As the I3RC-POL outputs intensity values, it also supplies the corresponding standard error associated with the calculation as seen in Section 4.2.3. Using this information, the overall expected uncertainty may be computed by adding and subtracting the standard error to the outputted intensity results. This uncertainty can be seen in figures 6.1 and 6.2 as the dashed blue envelopes, also known as the Monte Carlo noise.

Intensity values initially have a large variability when the samples are small. This can be attributed to the large amount of noise seen in the Monte Carlo envelopes (Figures 6.1, 6.2). When the number of samples of photons increases, intensity values can be better resolved and the amount of noise decreases to a small amount as seen in the decreasing size of the envelopes (Figure 6.1, 6.2). Analyzing when the intensity values approaches a certain number and standard deviation is small can help diagnose the number of photons necessary to simulate accurate results with very little noise.

Envelope testing may also determine the validity of benchmarked results. When the I3RC-POL's envelope overlaps benchmarked intensity values the validity of this calculation is confirmed. This scenario can be seen in figure 6.1. The red expected results are within

the outputted result's envelope meaning any small change in results is within the expected uncertainty due to Monte Carlo noise and not the accuracy of the model. Figure 6.2 shows results for a case in which the model is no longer valid. Note, the expected results do not lie within the outputted envelope. In this case, there is some error in results that can not be explained by Monte Carlo noise. The magnitude of this error can be represented as the difference between the I3RC-POL envelope and the expected value.

6.2.2 Viewing Zenith Angle Testing

The next type of testing used for the benchmarking of the I3RC-POL is the viewing zenith angle comparison. After envelope results have determined the number of photons needed to resolve outputted values, I3RC-POL's results may be analyzed as a function of view angle without concern of noise impacting results. As the angle in which intensity is calculated changes from nadir to oblique, the value of polarized Stokes components and unpolarized intensity values will change. Analyzing I3RC-POL's outputs as a function of viewing angle can help to determine if the magnitude of results and the angular shapes are behaving as expected.

6.2.3 Percent Error

Finally, percent error comparisons were completed. When examining errors within the model, it is important to understand their magnitude. In doing so, percent error was calculated using:

$$\frac{|\text{I3RC-POL Results} - \text{Expected Results}|}{|\text{Expected Results}|} \times 100\% \tag{6.1}$$

If the standard error of radiance is calculated, standard error of the percent error may also be determined using the outputted intensity and error provided. As in outputted standard

error values, the smaller the error value the higher the confidence in the I3RC-POL.

$$\sigma = \sqrt{\frac{\text{Expected Error}}{\text{I3RC-POL Intensity}} + \frac{\text{Expected Intensity * I3RC-POL Error}}{\text{I3RC-POL Intensity}^2}} \tag{6.2}$$

6.3 Unpolarized One Dimensional Results

Initial benchmarking of the I3RC-POL was performed in an unpolarized one dimensional domain against the original, benchmarked I3RC. To simulate an unpolarized event, the phase matrix within the I3RC-POL domain will contain zeros except for $P_{11}(\Theta)$, representing the I3RC phase function:

$$P(\Theta) = \begin{pmatrix} P_{11}(\Theta) & 0 & 0 & 0 \\ 0 & 0 & 0 & 0 \\ 0 & 0 & 0 & 0 \\ 0 & 0 & 0 & 0 \end{pmatrix} \tag{6.3}$$

Both the I3RC-POL and I3RC plane parallel simulations utilize a Rayleigh phase function, solar flux $F_0 = 1$, surface albedo = 0, single scattering albedo $\omega_0 = 1$, the cosine of the solar zenith angle $\mu_0 = 1$, and two different optical depths $\tau = 0.02$ and $\tau = 10$. In addition to the benchmarking tests described in Section 6.3, a reciprocity analysis was also completed.

6.3.1 Envelope Analysis

The first step in benchmarking the I3RC-POL's unpolarized results to the original I3RC was envelope testing. This analysis was performed over two different optical depths $\tau = 0.02$ and $\tau = 10$. Two different viewing zenith angles were also used, $\mu = 1$ and $\mu = 0.02$.

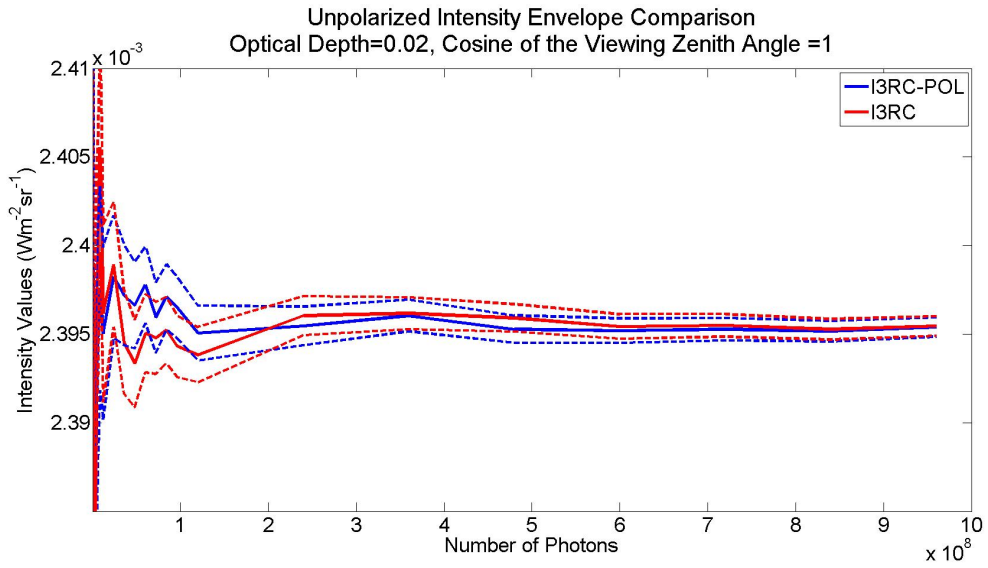

Figure 6.3: Unpolarized envelope intensity comparison between I3RC and I3RC-POL for $\mu = 1$ and $\tau = 0.02$

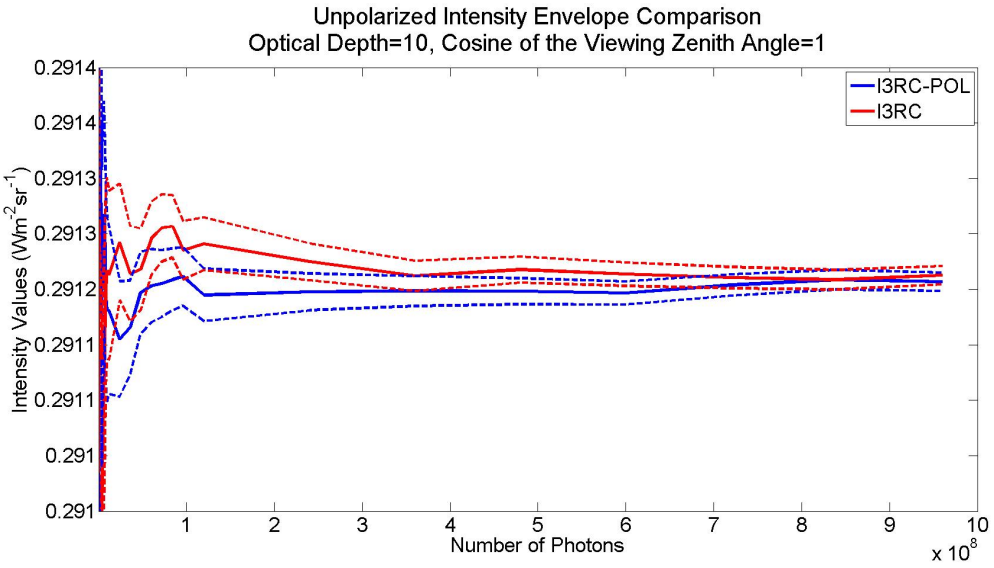

Figure 6.4: Unpolarized envelope intensity comparison between I3RC and I3RC-POL for $\mu = 1$ and $\tau = 10$

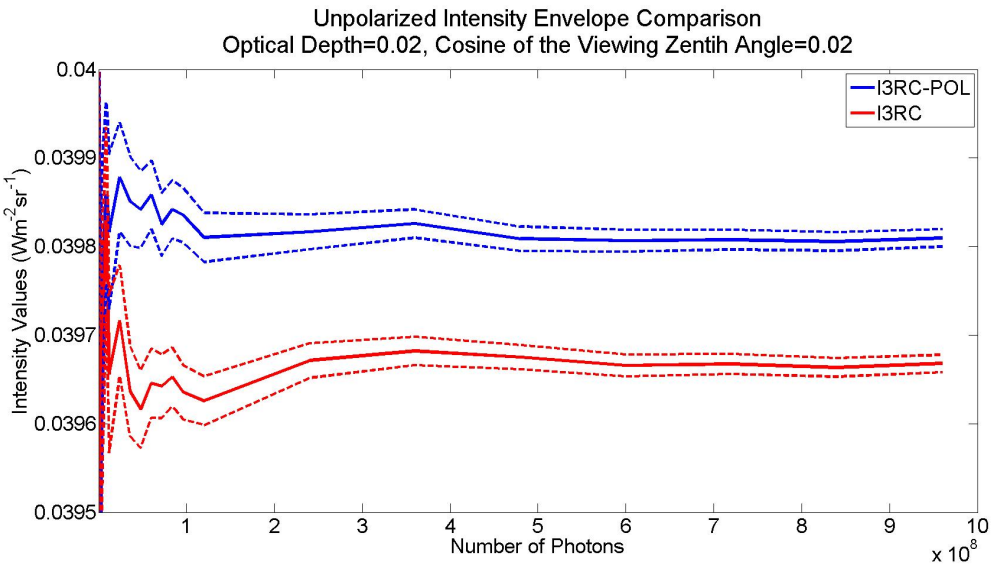

Figure 6.5: Unpolarized envelope intensity comparison between I3RC and I3RC-POL for $\mu = 0.02$ and $\tau = 0.02$

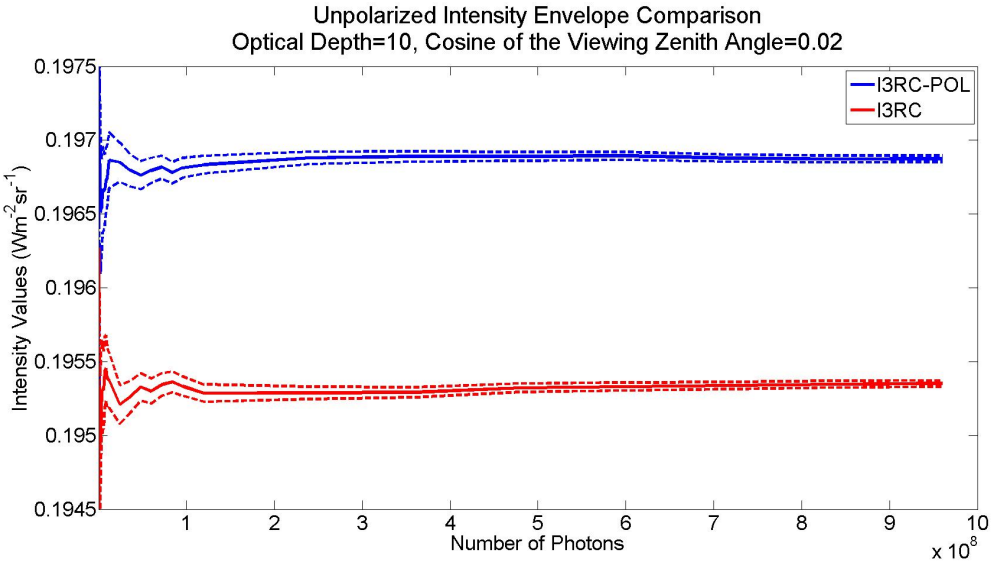

Figure 6.6: Unpolarized envelope intensity comparison between I3RC and I3RC-POL for $\mu = 0.02$ and $\tau = 10$

Unpolarized results resolve to their final value after about 10^8 photons. When $\tau = 10$, the number of photons appeared to be smallest, especially when $\mu = 0.02$ (Figure 6.6) where only $2 * 10^8$ photons were sampled. When $\mu = 1$ the intensity value resolved after about $8 * 10^8$ photons (Figure 6.4). Using an optical depth of $\tau = 0.02$, the results for both $\mu = 0.02$ (Figure 6.5) and $\mu = 1$ (Figure 6.3) resolved near $6 * 10^8$ photons. This analysis shows that the unpolarized intensity values for the I3RC-POL can be considered consistent after a threshold of about $6 * 10^8$ photons with an associated uncertainty of 10^{-5} for $\tau = 1$ and 10^{-6} for $\tau = 0.02$. This knowledge will be used when selecting the number of photons in Section 6.3.2.

Benchmarking results can also be analyzed using the envelope testing. First by examining envelope results when $\mu = 1$, it can be seen that the unpolarized intensity values are consistent with the I3RC. In all optical depths, both the I3RC-POL and the I3RC have intensity values within each other's envelopes. This suggests that when the viewing zenith angle is close to nadir, the I3RC-POL is able to replicate the I3RC's unpolarized results. Any small variation is caused by the expected error in the Monte Carlo model.

While these results are promising, some variation can be seen when calculating intensities at $\mu = 0.02$. In both optical depths, the I3RC-POL's intensity envelope fails to converge to I3RC's values. The differences are small, about 0.00015 $\mathrm{Wm^{-2}sr^{-1}}$ when $\tau = 0.02$ and 0.0017 $\mathrm{Wm^{-2}sr^{-1}}$ for $\tau = 10$. This increase in error over optical depth may be due to the increase number of calculations that must occur when more scattering is introduced. Due to the fact that the I3RC has already been benchmarked, it appears that the source of this error must reside in the I3RC-POL. These conclusions will be seen throughout benchmarking results for the I3RC-POL.

6.3.2 View Zenith Angle Comparisons

The next benchmarking test performed on the I3RC-POL's unpolarized results was a viewing zenith angle comparison. Prior to simulations, it is necessary to select the number of photons

to sample. The previous envelope testing section showed that the I3RC-POL's intensity result converge to its final value after 10^8 photons. To perform this analysis, $9.6{*}10^8$ photons were sampled yielding a maximum magnitude in standard error of 10^{-5} in all unpolarized viewing zenith angle calculations. In doing so, none of the standard error results can be seen in the figure due to this small error. Viewing zenith angle comparisons were performed for two different optical depths, $\tau = 0.02$ and $\tau = 10$. In both figures, the cosine of the solar zenith angle was kept constant $\mu_0 = 1$.

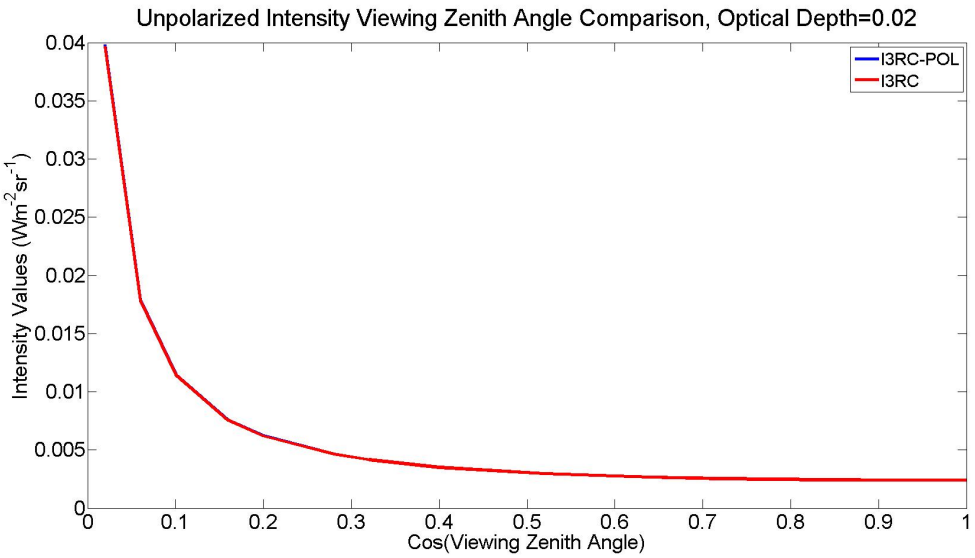

Figure 6.7: Unpolarized viewing zenith angle intensity comparison between I3RC and I3RC-POL for $\tau = 0.02$ and $\mu_0 = 1$. $9.6 * 10^8$ photons were sampled with all standard error values of 10^{-6}.

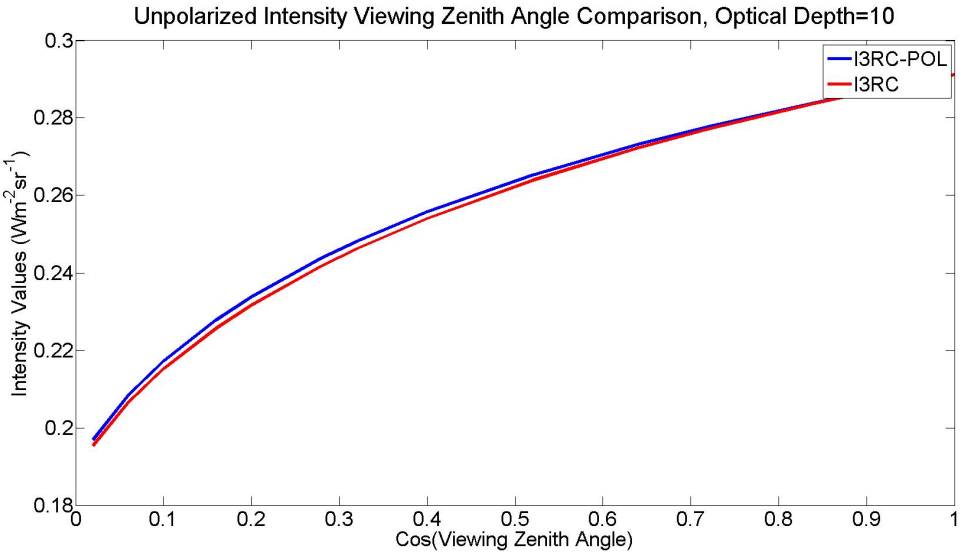

Figure 6.8: Unpolarized viewing zenith angle intensity comparison between I3RC and I3RC-POL for $\tau = 10$ and $\mu_0 = 1$. $9.6 * 10^8$ photons were sampled with all standard error values having of 10^{-5}.

As seen in figure 6.7 when $\tau = 0.02$, the I3RC-POL appears to replicate the original I3RC's unpolarized intensity results. Both the magnitude of intensity values and the shape over viewing zenith angles appear consistent. Although the envelope testing did reveal that when the viewing zenith angle was more oblique there was a slight error, this difference can not be seen in figure 6.7 due to its small magnitude. When comparing to results calculated in an optical depth of 10 (Figure 6.8), a small error can be seen in the I3RC-POL. The I3RC-POL replicates I3RC's intensity values best when μ approaches 1 but is less accurate when μ approaches 0. The overall shape of I3RC-POL follows that of the I3RC but again there is some small error that appears more prevalent when the viewing zenith angle is more oblique.

6.3.3 Percent Error

Benchmark testing has revealed that there is a small error within the I3RC-POL. In order to determine it's influence, it is necessary to examine the magnitude in this possible bug. In doing so, a percent error comparison between the I3RC-POL and the I3RC was used. This calculation is performed using equation 6.1 with the I3RC providing the expected results . In figure 6.9, the percent error over the cosine of the viewing azimuth angles are provided for $\tau = 0.02$ and $\tau = 10$. In both calculations, $9.6 * 10^8$ photons were used. Using equation 6.2, the calculated standard errors were all within a magnitude of 10^{-4}.

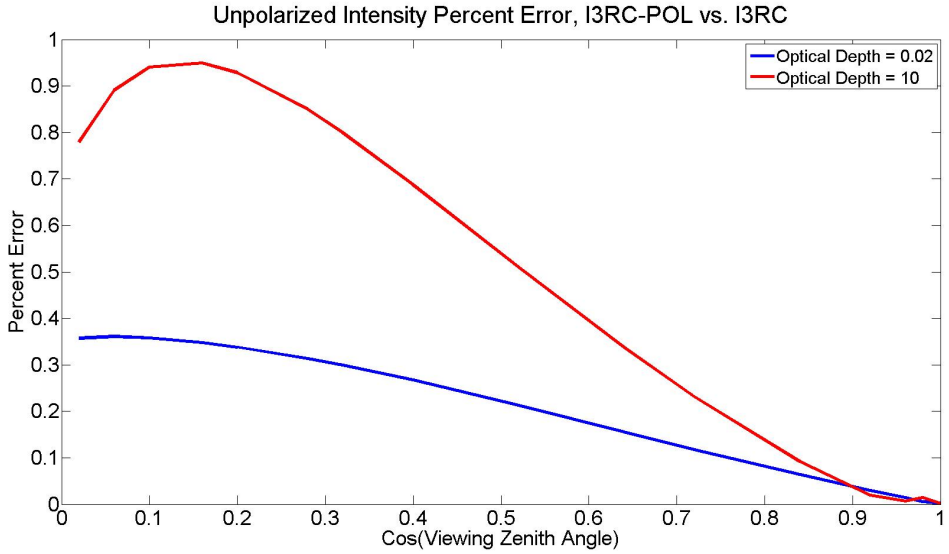

Figure 6.9: Unpolarized intensity percent error comparisons for $\tau = 0.02$ and $\tau = 10$. The number of photons simulated were $9.6 * 10^8$ with all calculated standard error values having a magnitude of less than 10^{-4}.

As can be seen in figure 6.9, all of I3RC-POL's results were within 1% percent error regardless of optical depth or viewing zenith angle. As suggested in Sections 6.3.1 and 6.3.2, the error within the I3RC-POL increases when the optical depth is larger and when the cosine of the viewing zenith angle approaches 0. For $\mu = 1$, the percent error is very small and appears to be even approaching 0 for both $\tau = 0.02$ and $\tau = 10$. This may suggest that this bug within the I3RC-POL is highly dependent on the viewing zenith angle. There is an additional odd angular behavior in percent error values, specifically when $\tau = 10$. A

maximum in error appears when the cosine of the viewing zenith angle is about 0.15. This behavior is not present when $\tau = 0.02$ therefore it must appear when more scattering occurs. Additionally when $\mu = 0.92$, the percent error for $\tau = 10$ case is less than that of $\tau = 0.02$. This is odd due to the fact that our hypothesis suggests that error should be larger in a more optically thick atmosphere. Currently a physical explanation of this behaviors have not been determined but it may be a clue in resolving the angular error within the I3RC-POL. It is also important to again preface that although an error is present, having initial benchmarking results within 1% error is promising.

6.3.4 Reciprocity

The final analysis performed on the unpolarized, plane parallel, Rayleigh scattering simulation was a reciprocity comparison. The theory of reciprocity may be expressed mathematically as seen in equation 6.4:

$$\frac{I(\theta_0, \phi_0; \theta, \phi)}{F_0 \cos(\theta_0)} = \frac{I(\theta, \phi; \theta_0, \phi_0)}{F_0 \cos(\theta)} \tag{6.4}$$

Physically, reciprocity states that an intensity calculation given solar angles (μ_0, ϕ_0) with viewing angles of (μ, ϕ) will be equivalent to the same intensity calculation if the solar angles and viewing angles were interchanged. For a full explanation of this this theory, see Di Girolamo (1998). I3RC-POL reciprocity simulations were completed over the optical depths of $\tau = 0.02$ and $\tau = 10$. While ϕ values for both solar and viewing angles must also be interchanged, our simulations were kept constant and equal to zero. The number of photons used was $9.6 * 10^8$. Standard error was also calculated using equation 6.2 with all values of about 10^{-4}. The angles combinations examined can be seen in table 6.1.

	μ_1	μ_2
Case #1	0.02	1
Case #2	0.02	0.52
Case #2	0.52	1

Table 6.1: μ combinations used in reciprocity testing

Using these three cases, simulations were made using μ_1 as the cosine of the solar zenith angle and μ_2 as the cosine of viewing zenith angle. Again note that only zenith angle are interchanged since the azimuth angle in all calculations is equal to zero. Next, the simulations were recalculated switching the angles between solar and viewing μ. To analyze the accuracy in I3RC-POL results, the ratio of the two simulations were taken for each angular combinations. If the ratio was close to one, the theory of reciprocity is met because both calculations yielded the same results. In table 6.2, the reciprocity ratios can be see for the three different μ scenarios.

Optical Depth	**Case #1**	**Case #2**	**Case #3**
0.02	0.99992	0.99675	0.99866
1	1.01243	0.99212	0.99503

Table 6.2: I3RC-POL reciprocity ratio comparison's for the different μ cases with error values of 10^{-4}

Overall, the reciprocity comparison yields results that are close but not equal to the expected ratio of 1. Over all optical depths, the reciprocity ratio results are consistent with findings in unpolarized benchmarking thus far. When $\tau = 10$ the ratios diverge further from 1 with a maximum difference of 0.012 at more oblique μ values. When $\tau = 0.02$ this behavior is not present. The I3RC-POL is able to best replicate the reciprocity theory when $\mu = 0.02$ and $\mu = 0.52$. In previous benchmarking results, Sections 6.3.1, 6.3.2, and 6.3.3, the most accurate results all occurred when $\mu = 1$. This strange behavior further confirms that there is some angular error within the I3RC-POL that must be considered.

6.4 Polarized One Dimensional Results

Although there appears to be a small bug within the unpolarized I3RC-POL results that must still be resolved, obtaining results within 1% error motivated our continuation of the benchmark process. The next benchmark task was to determine the validity of the I3RC-POL using a fully polarized calculation. Results were compared against Coulson's tabulated values as provided in "Tables Related to Radiation Emerging From a Planetary Atmosphere with Rayleigh Scattering" (*Coulson et al.*, 1960). Ranging from optical depths $\tau = 0.02$ to $\tau = 1$ over different viewing and solar zenith angles, Coulson's work provides solutions for the intensity, Q, U, and V portion of the Stokes vector in a Rayleigh atmosphere. Although this benchmarking resource is commonly used in polarized radiative transfer, improvements to Coulson's results have been made (*Natraj et al.*, 2009).

Polarized simulations were calculated for solar flux $F_0 = 1$, surface albedo = 0, single scattering albedo $\omega_0 = 1$, and two different optical depths, $\tau = 0.02$ and $\tau = 10$. Consistent with Coulson's results, all scattering was represented by the Rayleigh scattering phase matrix as seen in equation 6.5:

$$P(\Theta)_{rayleigh} = \frac{3}{4}\begin{pmatrix} 1+\cos(\Theta)^2 & 1-\cos(\Theta)^2 & 0 & 0 \\ 1-\cos(\Theta)^2 & 1+\cos(\Theta)^2 & 0 & 0 \\ 0 & 0 & 2\cos(\Theta) & 0 \\ 0 & 0 & 0 & 2\cos(\Theta) \end{pmatrix} \tag{6.5}$$

The cosine of the solar zenith angle utilized in all calculations, $\mu_0 = 1$, provides a useful physical simplification. When the solar zenith angle is at nadir, viewing azimuth angle should not influence results. When they do, additional information may be provided to help deduce the error within the I3RC-POL. The same benchmarking strategy was performed; first envelope testing results were analyzed, next the analysis was expanded over all viewing

zenith angles, and finally we used percent error when possible to determine the overall accuracy of our findings.

6.4.1 Intensity Comparison

Envelope Analysis

As in Section 6.3.1, it is important to determine if polarized intensity results are converging to a value containing a small amount of Monte Carlo noise. In doing so, the number of photons necessary to sample accurate results is also determined. Envelope results were calculated for optical depths of $\tau = 0.02$ and $\tau = 1$. To examine this angular issue seen in the unpolarized benchmarking results, envelope comparisons were completed for viewing zenith angles of $\mu = 0.02$ and $\mu = 1$ with 6 different viewing azimuth angles $\phi = 0°, 60°, 90°, 120°,$ and $180°$.

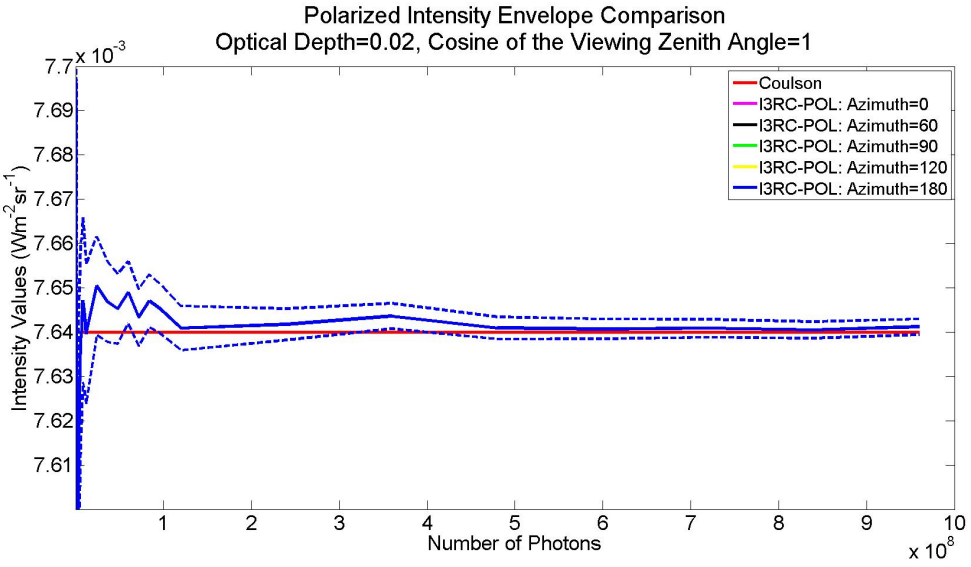

Figure 6.10: Polarized envelope intensity (I) comparison between the I3RC-POL and Coulson for $\mu = 1$ and $\tau = 0.02$.

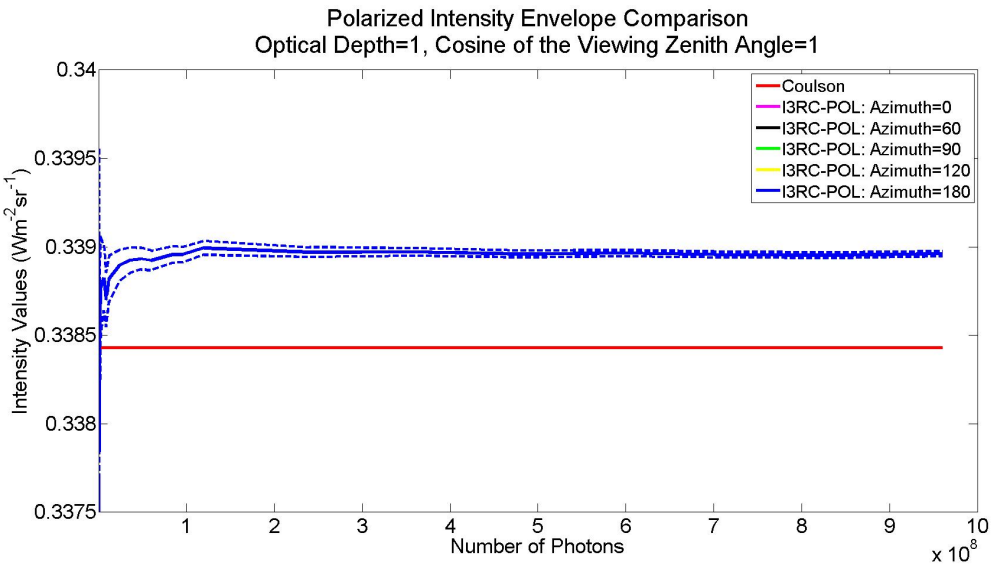

Figure 6.11: Polarized envelope intensity (I) comparison between the I3RC-POL and Coulson for $\mu = 1$ and $\tau = 1$.

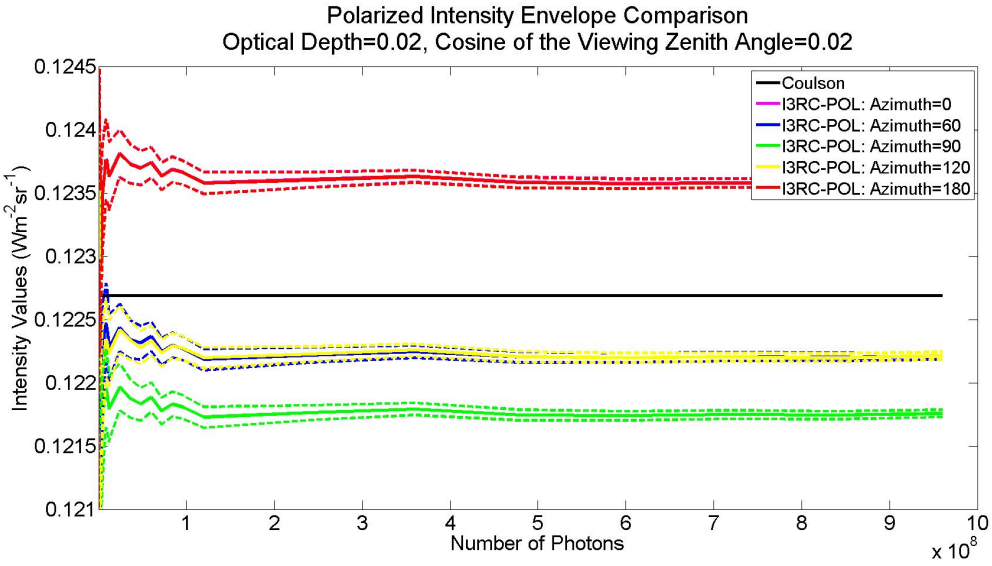

Figure 6.12: Polarized envelope intensity (I) comparison between the I3RC-POL and Coulson for $\mu = 0.02$ and $\tau = 0.02$.

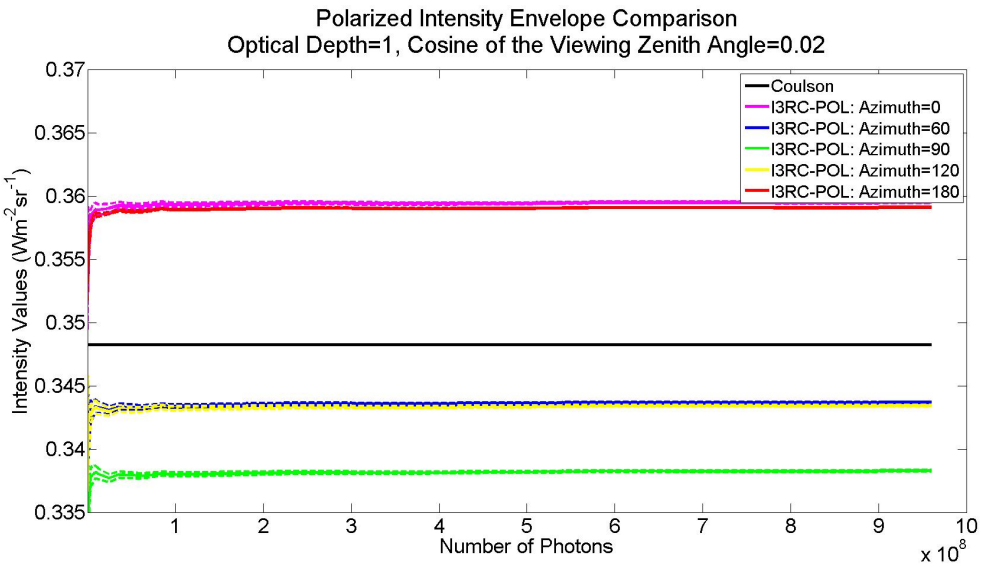

Figure 6.13: Polarized envelope intensity (I) comparison between the I3RC-POL and Coulson for $\mu = 0.02$ and $\tau = 1$.

Similar to the unpolarized envelope testing results (Section 6.3.1), the intensity component of the Stokes vector also converged to an intensity value after 10^8 photons. The smallest number of photons were required when $\tau = 1$ and $\mu = 0.02$ with just less than 10^{-8} photons (Figures 6.13). Using the same optical depth but $\mu = 1$ (Figure 6.11), the number of photons required for convergence was increased slightly to $2 * 10^8$ photons. Finally, examining figures 6.10 and 6.12, $\tau = 0.02$ had consistent results as both viewing zenith angle combinations required around $5 * 10^8$ photons to yield a convergence of intensity values. It is important to note that as the photon sample increases, the standard error decreases significantly leading to a value of around 10^{-7} for $\tau = 0.02$ and 10^{-6} for $\tau = 1$. Considering these results, it is safe to say that using a sample of photons larger than $5 * 10^8$ should yield results with low influence from Monte Carlo noise.

Examining the convergence of the I3RC-POL's results to Coulson, several observations may be made. When $\mu = 1$ the I3RC-POL is consistent with Coulson's results as different azimuth angles do not appear to influence the intensity values computed. As seen in the unpolarized results, when the optical depth is thin $\tau = 0.02$ Coulson's tabulated value is exactly within the I3RC-POL's envelope meaning any variance in outputted value can be

explained by the noise within the model. When the optical depth increases though, results are not consistent. The I3RC-POL fails to converge to Coulson's results even when $\mu = 1$. Although this separation is small, 0.0004 $\mathrm{Wm^{-2}sr^{-1}}$, the noise due to the Monte Carlo is not the source of this error. The lack of convergence when $\mu = 1$ is not seen in unpolarized results which suggests that the error within the I3RC-POL may be more prevalent when polarization is included.

Another important observation can be made when examining envelope results for $\tau = 0.02$ and $\mu = 0.02$, (Figure 6.12). First, intensity results have many of the same behaviors as unpolarized results. When the viewing zenith angle becomes more oblique, $\mu = 0.02$, the I3RC-POL fails to resolve to expected benchmarked values and experiences a variance in intensity results due to viewing azimuth angle in an observable pattern. The viewing azimuth angles create a lack of envelope convergence but they do so in an observable pattern as certain viewing azimuth angles produce the same results. For example the viewing azimuth angle pairs of ($\phi = 0°$ and $\phi = 180°$) and ($\phi = 60°$ and $\phi = 120°$) have intensity values that are virtually the same. When the viewing azimuth angle equals 90°, the I3RC-POL's envelope also does not converge to Coulson's result but it does not have a reciprocal azimuth pair as the other angles. This forms a hypothesis that the angular difference in intensity values may be due to a $\cos(\phi)$. This pattern may be explained by a simple cosine function. For example, cos(0) and cos(180) have the exact same value but different sign. This can also be seen for cos(60) and cos(120). This forms a hypothesis that the angular difference in intensity values may be due to a $\cos(\phi)$. It is also important to note that these azimuth angle pairs will be referenced throughout the duration of the benchmarking results. When $\tau = 1$, this angular dependence is also present (Figure 6.15). The different azimuth angles appear to have similar results, but have more variance with each other compared to the same pattern seen in the thinner optical depth. This may also add to the hypothesis that as more scattering occurs within a thicker optical depth, the error compounds.

Viewing Zenith Angle

An examination of polarized intensity values over viewing zenith angle may also help to confirm the angular error within the I3RC-POL. Calculations included optical depths of $\tau = 0.02$ and $\tau = 1$ and viewing zenith angles of $\mu = 0.02$ and $\mu = 1$ with 6 different viewing azimuth angles $\phi = 0°, 60°, 90°, 120°,$ and $180°$. The number of photon's calculated were consistent with the envelope testing's results and $9.6 * 10^8$ photons were used in order to minimize Monte Carlo noise. The resulting standard errors were all within a value of 10^{-6} therefore the standard error can not be seen in any of the viewing zenith angle comparisons.

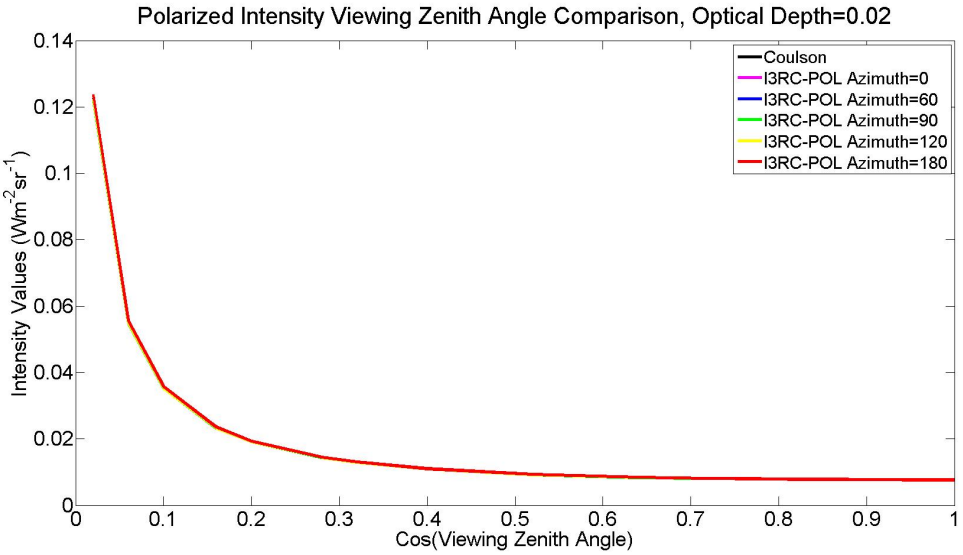

Figure 6.14: Viewing zenith angle intensity (I) comparison between the I3RC-POL and Coulson for $\tau = 0.02$ and $\mu_0 = 1$. $9.6 * 10^8$ photons were sampled with all standard error values of 10^{-7}.

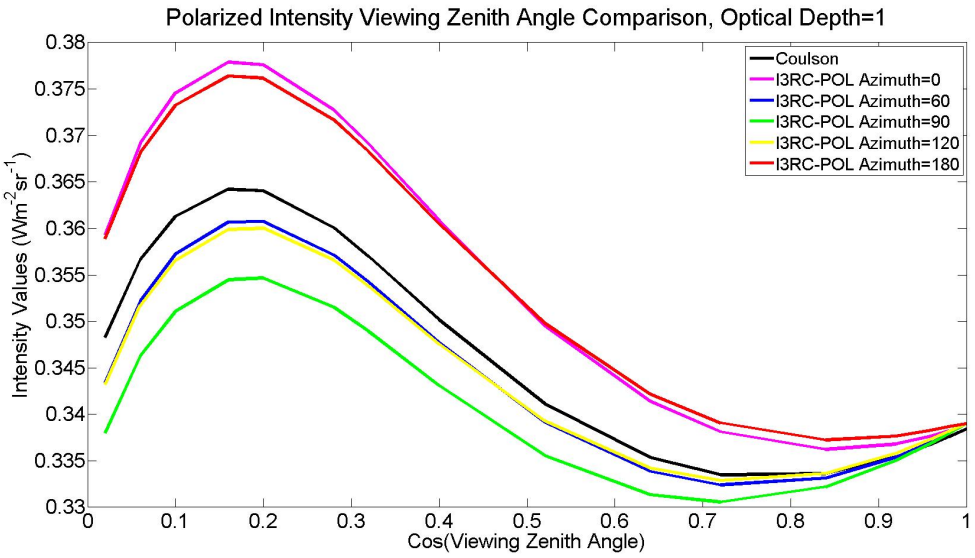

Figure 6.15: Viewing zenith angle intensity (I) comparison between the I3RC-POL and Coulson for $\tau = 1$ and $\mu_0 = 1$. $9.6 * 10^8$ photons were sampled with all standard error values of 10^{-6}.

The I3RC-POL is able to replicate Coulson's expected results quite well. I3RC-POL's results are consistent to Coulson's expected results in both magnitude and shape. Although there is an error seen as in envelope testing over different azimuth angles that can not be attributed to Monte Carlo noise, this error is small enough to not be differentiable on figure 6.14.

When the optical depth is thicker, in this case $\tau = 1$, the I3RC-POL is less accurate over different viewing zenith angles (Figure 6.15). This angular dependence is not new though and this lack of consistency as μ approaches 0.02 has also been seen in other models (*Evans and Stephens*, 1990). Not only is there a difference in value across viewing zenith angle, but the influence of viewing azimuth angle become even more apparent. Again, the pairing of intensity results due to viewing azimuth pairs ($\phi = 0°$ and $\phi = 180°$) and ($\phi = 60°$ and $\phi = 120°$) are no longer as exact as seen in $\tau = 0.02$. This can especially be seen when comparing viewing azimuth angles $\phi = 0°$ and $\phi = 180°$. Notice a spike in their difference near $\mu = 0.15$. This spike of inaccuracy around this μ was also seen in the percent error analysis for the unpolarized case, Section 6.3.3. This confirms the hypothesis that there is not only the same error seen in the unpolarized cases, but also a cosine angle error that

effects the polarized calculations.

Percent Error

In order to understand the magnitude of this angular error within the I3RC-POL, a percent error analysis was performed. Using equation 6.1 with Coulson's results providing the expected results, percent error was calculated for $\tau = 0.02$ and $\tau = 1$ when $\mu_0 = 1$. In both cases, $9.6 * 10^8$ photons were used with an uncertainty values of 10^{-6}.

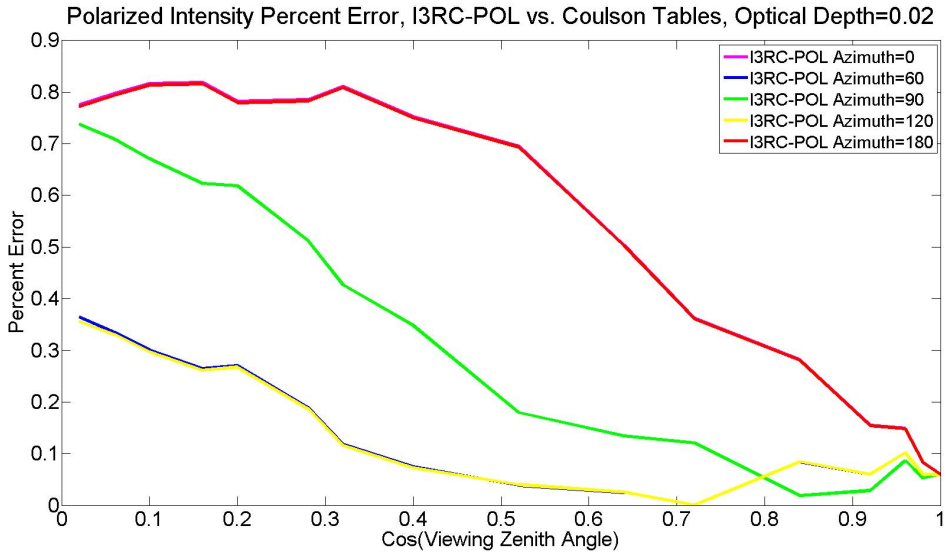

Figure 6.16: Polarized intensity percent error comparisons over the cosine of the viewing zenith angle for $\tau = 0.02$ and $\mu_0 = 1$. The number of photons simulated were $9.6 * 10^8$ with all standard error values less than 10^{-7}.

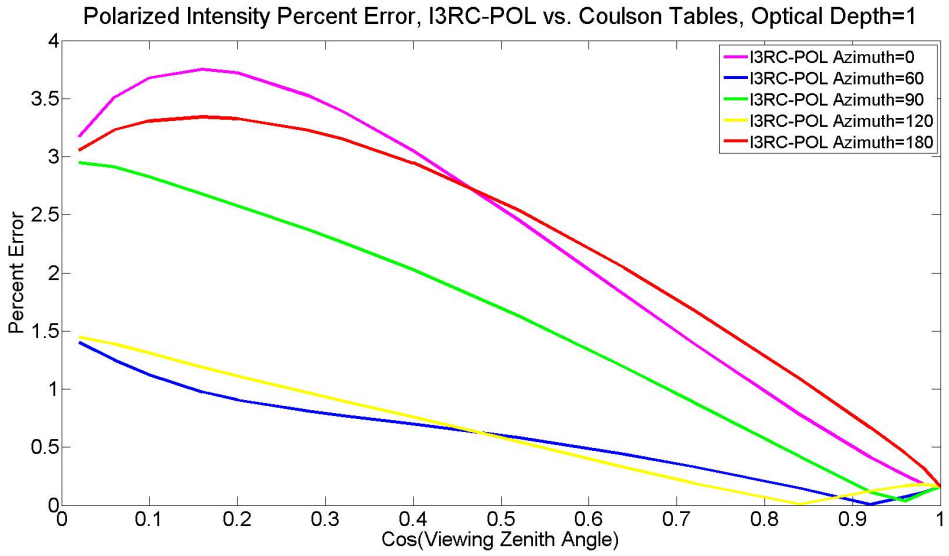

Figure 6.17: Polarized intensity percent error comparisons over the cosine of the viewing zenith angle for $\tau = 1$ and $\mu_0 = 1$. The number of photons simulated were $9.6 * 10^8$ with all standard error values less than 10^{-6}.

All of the I3RC-POL's results are within 1% error for an optical depth of 0.02 (Figure 6.16). When μ approaches 1, I3RC-POL's results are consistent with Coulson's expected values as the percent error is about 0.1% regardless of azimuth angle. Even though this lack of large percent error suggest's highly accurate results, envelope testing has previously proven that when $\mu = 0.02$, I3RC-POL's results contain an error outside the certainty range that may occur due to Monte Carlo noise. This can be seen as the percent error increases and produces different results for different viewing azimuth angles when $\mu = 0.02$. The same azimuthal behavior was seen in Figure 6.12. Although this odd behavior is due to an error within the I3RC-POL, percent error results of less than 1% is still achieved.

When $\tau = 1$ the percent error increases to values under 4% error (Figure 6.17). The behavior in these percent error findings are again similar to findings previously discussed. When $\mu = 1$, all values converge to a percent error less than 0.5% error regardless of viewing azimuth angle. When the viewing zenith angle becomes more oblique, not only does the percent error change but the shape of the percent error also changes. For example, both $\phi = 0°$ and $\phi = 120°$ initially have percent errors larger than their respective viewing

azimuth pairs but when $\mu = 0.45$ both the results from these viewing azimuth angles cross their respective alternate viewing azimuth angles. This odd behavior may be a clue to the angular error within the I3RC-POL.

6.4.2 Q Comparison

The next section of benchmarking test examines the Q component of the Stokes vector. Physically Q represents linear polarization. In determining the accuracy of I3RC-POL's Q values, the same three benchmarking analysis were examined.

Envelope Analysis

As in the polarized envelope calculations, Q envelope results were calculated for optical depths of $\tau = 0.02$ and $\tau = 1$ over $\mu = 0.02$ and $\mu = 1$ for 6 different viewing azimuth angles $\phi = 0°, 60°, 90°, 120°,$ and $180°$.

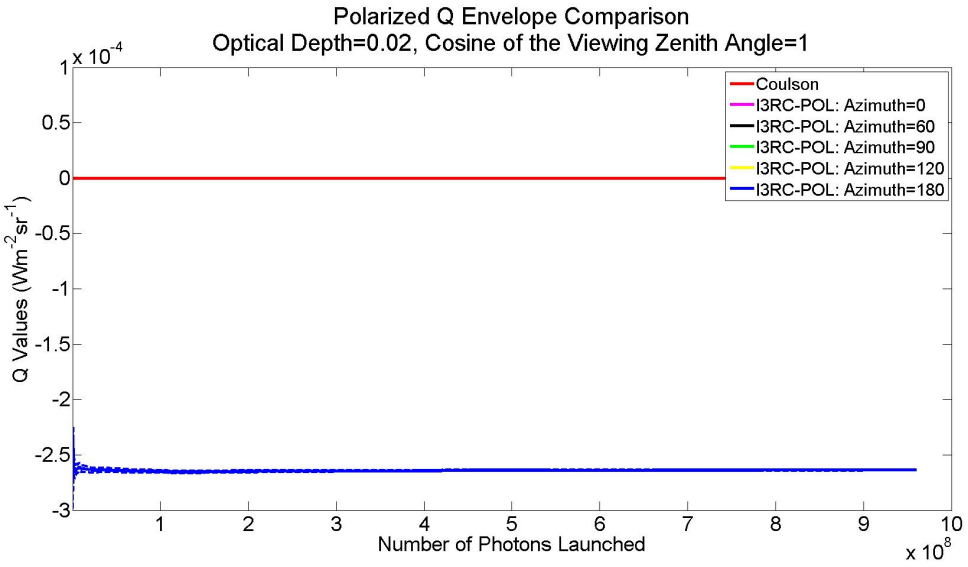

Figure 6.18: Polarized Q envelope comparison between the I3RC-POL and Coulson for $\tau = 0.02$ and $\mu = 1$.

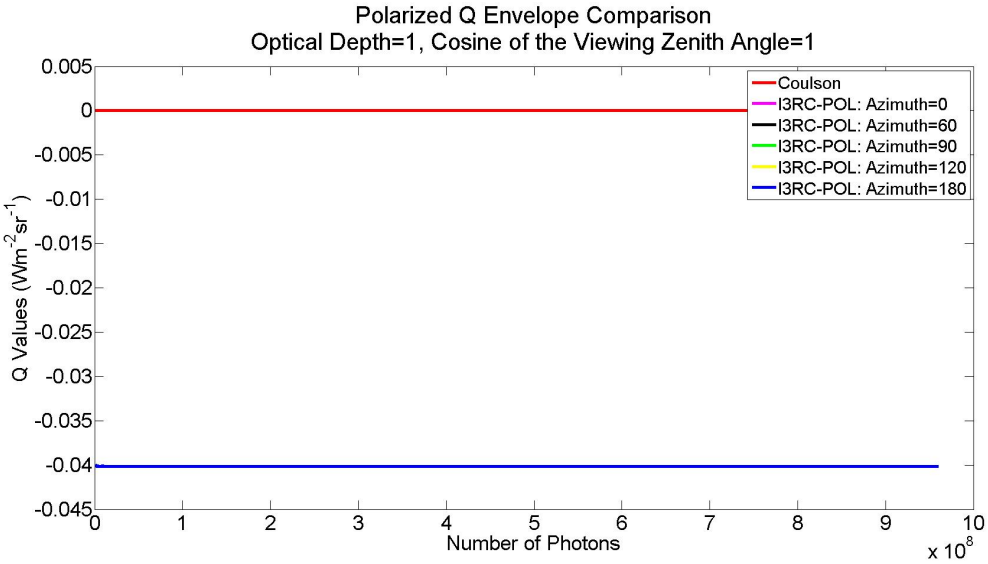

Figure 6.19: Polarized Q envelope comparison between the I3RC-POL and Coulson for $\tau = 1$ and $\mu = 1$.

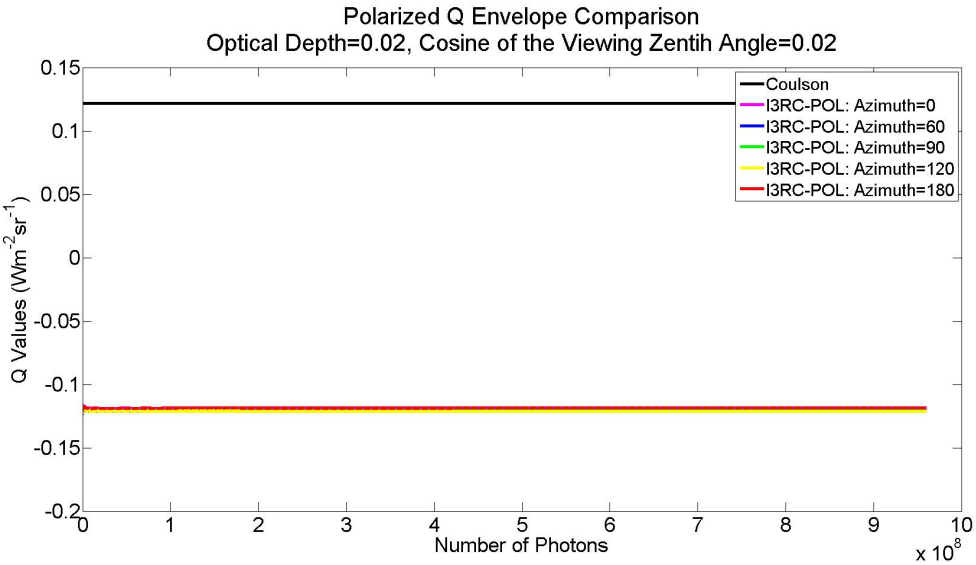

Figure 6.20: Polarized Q envelope comparison between I3RC-POL and Coulson for $\tau = 0.02$ and $\mu = 0.02$.

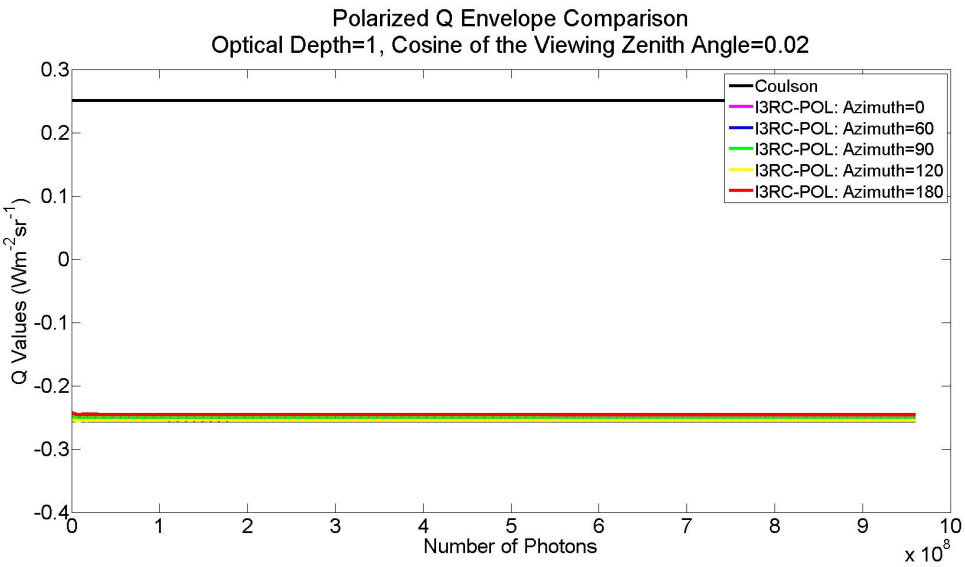

Figure 6.21: Polarized Q envelope intensity comparison between the I3RC-POL and Coulson for $\tau = 1$ and $\mu = 0.02$.

In all optical depths and viewing zenith angle combinations, both Q values and standard error values converge over fewer photons less than 10^8 photons with standard error values of 10^{-5} (Figures 6.18-6.21). Specific number of photons may be difficult to determine due to the lack of detail in these figures. To be consistent with previous benchmarking, using any photon value over a magnitude over 10^8 should result in Q values converging on it's expected values.

Unfortunately, envelope testing for Q values were not as informative as the previous unpolarized and polarized intensity envelope analysis. Although the magnitude of the Q results appear to be similar all fails to converge to the same value as Coulson due to the change in sign. Although this is odd behavior, it has also been seen in other models benchmarking results (*Evans and Stephens*, 1990). A physical explanation to this problem is directly related to the opposite reference frame conventions of the I3RC-POL and Coulson. This observation, along with additional Q behavior will be more apparent in the following viewing zenith angle analysis.

Viewing Zenith Angle

Viewing zenith angle testing yielded far more information to the behavior of I3RC-POL's Q results. Calculations occurred over the same optical depths $\tau = 0.02$ and $\tau = 1$ for $\mu = 0.02$ and $\mu = 1$. Again, the cosine of the solar zenith angle was equal to 1. The number of photons simulated was again $9.6 * 10^8$ with an uncertainty magnitude of 10−5. This small value limited the standard error plots to appear on the following figures.

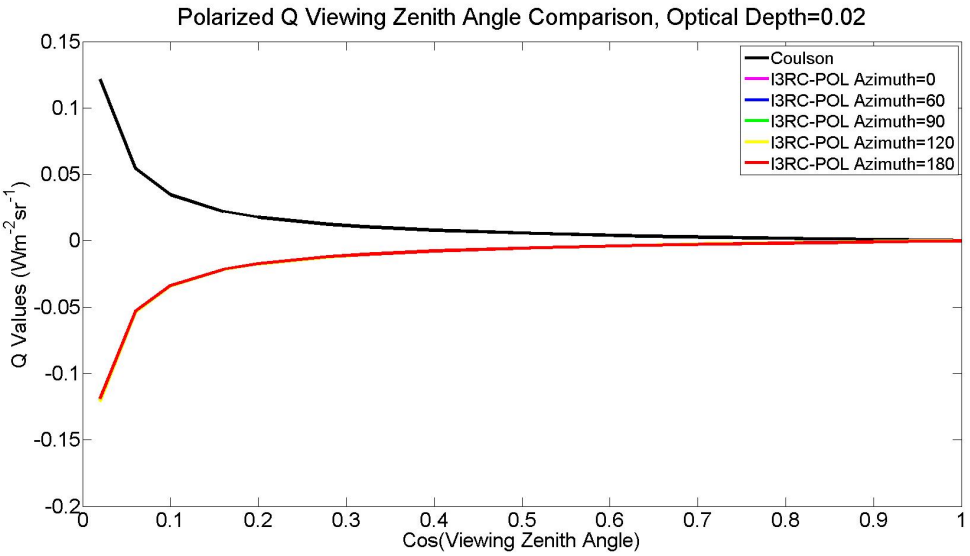

Figure 6.22: Viewing zenith angle Q comparison between I3RC and I3RC-POL for $\tau = 0.02$ and $\mu_0 = 1$. $9.6 * 10^8$ photons were sampled with all standard error values having a magnitude of 10^{-5}.

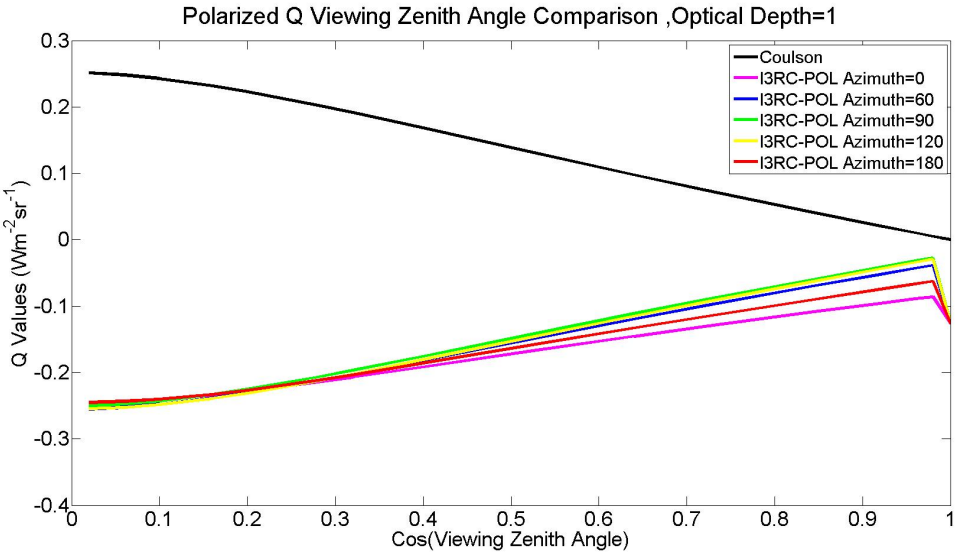

Figure 6.23: Viewing zenith angle Q comparison between I3RC and I3RC-POL for $\tau = 1$ and $\mu_0 = 1$. $9.6 * 10^8$ photons were sampled with all standard error values having a magnitude of 10^{-5}.

As seen in figures 6.22 and 6.23, the most obvious difference in the I3RC-POL's and Coulson's Q results is the opposite sign. Examining the values of Q when $\tau = 0.02$, the I3RC-POL matches the shape and expected magnitude of Coulson's expected results in magnitude and in shape (Figure 6.22). Additionally, the apparent difference due to viewing azimuth angle is not present due to its small value. When more scattering is introduced within an optical depth of $\tau = 1$ (Figure 6.23), there also appears to be a slight change of magnitude in Q values. As μ approaches 1, the Q results for different azimuth angles begin to diverge which is inconsistent to unpolarized and polarized intensity conclusion which at more accurate results at more nadir angles. Additionally, when μ is exactly 1, all of I3RC-POL's Q results spike to a lower number instead of approaching the expected value of 0. Physical explanation for this behavior has yet to be confirmed but this strange angular behavior must be considered with examining the I3RC-POL's bug.

Percent Error

Finally, percent error analysis was performed for I3RC-POL's Q results. In this case, a table is used to present this information for two reasons. First, Coulson's Q value of zero when

$\tau = 0.02$ for $\mu = 1$ prevents percent errors to be calculated. Secondly, the large spike in I3RC-POL Q values for $\tau = 1$ with $\mu = 1$ creates a figure in which little information can be extracted. These percent error results were calculated with $\tau = 0.02$ and $\tau = 1$ and when the cosine of the viewing zenith angle is equivalent to 0.02, 0.52, and 1 over the same six azimuth angles. Finally, the number of photons sampled, $9.6 * 10^8$ yielded uncertainty values of 10^{-5}.

Viewing μ	**$\phi = 0°$**	**$\phi = 60°$**	**$\phi = 90°$**	**$\phi = 120°$**	**$\phi = 180°$**
0.02	2.2524%	0.4655%	0.8119%	0.4084%	2.2489%
0.52	1.1649%	0.3927%	1.0539%	0.3919%	1.0774%
1	-	-	-	-	-

Table 6.3: Percent error comparison using Coulson's tabulated Q values and I3RC-POL Q values at an optical depth of 0.02. I3RC-POL outputs are categorized using the viewing azimuth angle.

Viewing μ	**$\phi = 0°$**	**$\phi = 60°$**	**$\phi = 90°$**	**$\phi = 120°$**	**$\phi = 180°$**
0.02	0.3144%	1.6290%	0.3051%	1.4382%	2.3265%
0.52	27.213%	12.584%	8.252%	11.676%	20.469%
1	210328%	210328%	210328%	210328%	210328%

Table 6.4: Percent Error comparison using Coulson's tabulated Q values and I3RC-POL Q values at an optical depth of 1. I3RC-POL outputs are categorized using the viewing azimuth angle.

When the optical depth is thin, $\tau = 0.02$, the I3RC-POL replicates Coulson's tabulated Q values much more accurately than an optically thicker atmosphere. Percent error results in this case were all within 2.5% (Table 6.3). When the optical depth increase to $\tau = 1$, the percent error struggled to match a reasonable value. As discussed in the envelope testing, there is a large spike in Q values which can also be seen in the percent error table (Table 6.4). When $\mu = 1$, I3RC-POL had a percent error of $210,328\%$. Keep in mind, Coulson's results were equal to 0.00006 $\mathrm{Wm^{-2}sr^{-1}}$ while the I3RC-POL produced values

around 0.126 $\mathrm{Wm}^{-2}\mathrm{sr}^{-1}$. This may seem like a large percent but in reality the difference is only a magnitude of 10^{-2} $\mathrm{Wm}^{-2}\mathrm{sr}^{-1}$.

6.4.3 U Comparison

The U component of the Stokes vector also describes the amount of linear polarization. It is important to note that in Rayleigh scattering for $\mu_0 = 1$, all of Coulson's tabulated results were equivalent to zero. This limits our benchmarking tests to just the viewing zenith angle and envelope comparisons.

Envelope Analysis

Envelope analysis of the U component of the Stokes vector provided more information than the same comparison of Q results. Calculations were performed again for the optical depths of $\tau = 0.02$ and $\tau = 1$ with $\mu = 0.02$ and $\mu = 1$ over different viewing azimuth angles.

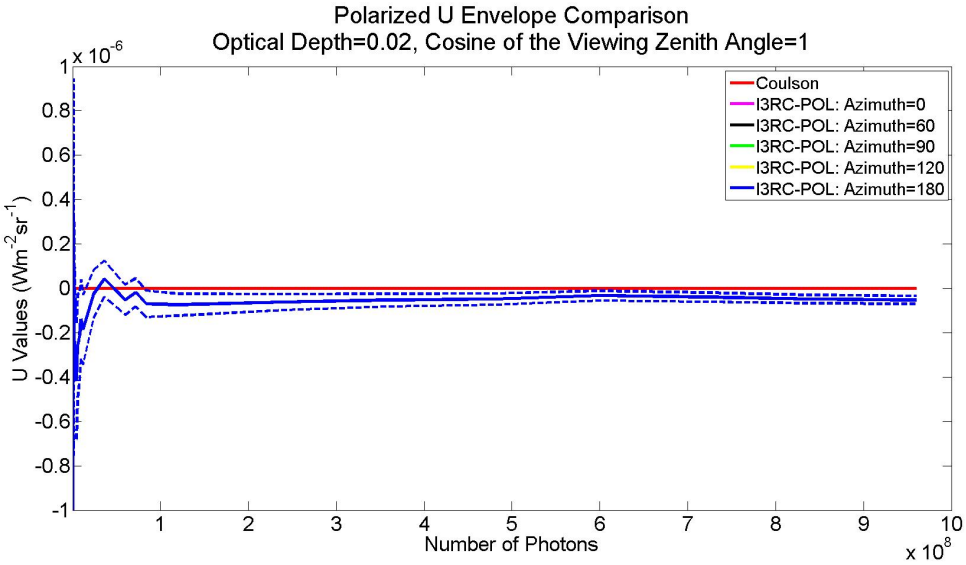

Figure 6.24: Polarized U envelope comparison between the I3RC-POL and Coulson for $\tau = 0.02$ and $\mu = 1$.

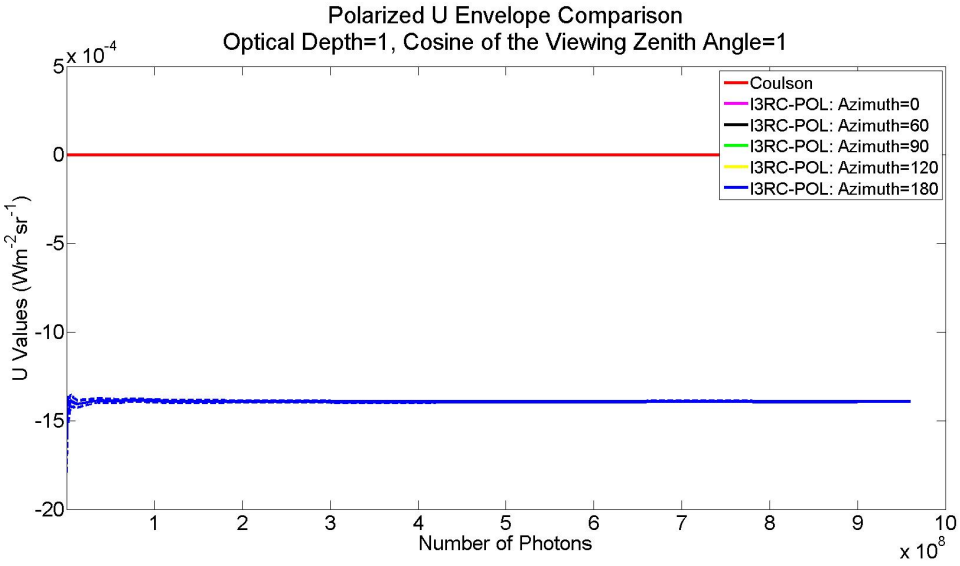

Figure 6.25: Polarized U envelope comparison between I3RC-POL and Coulson for $\tau = 1$ and $\mu = 1$.

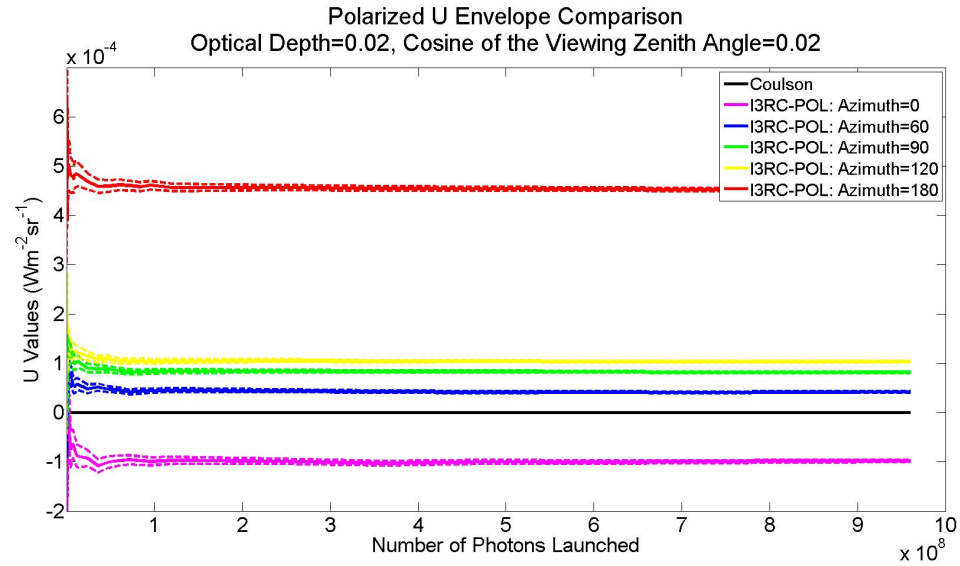

Figure 6.26: Polarized U envelope comparison between I3RC and Coulson for $\tau = 0.02$ and $\mu = 0.02$.

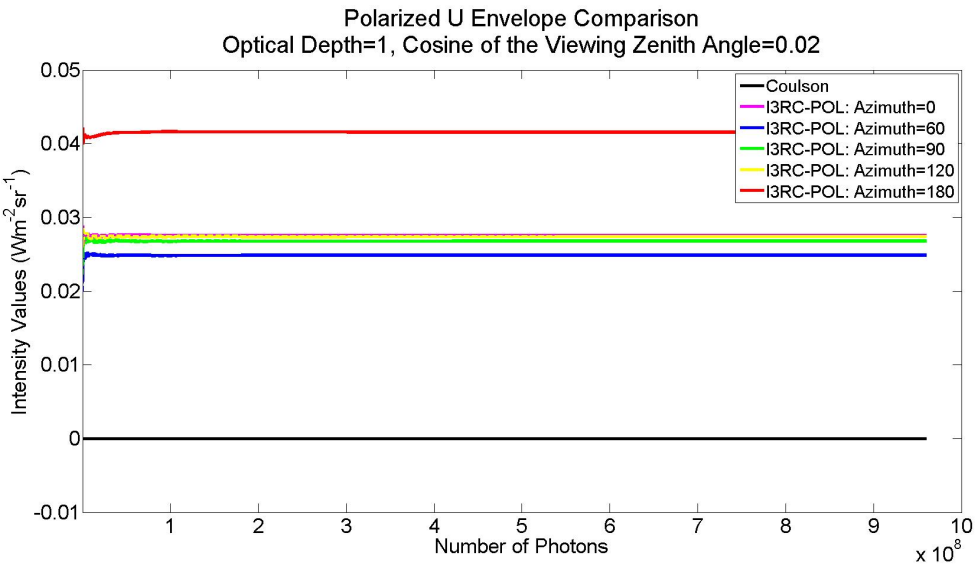

Figure 6.27: Polarized U envelope intensity comparison between I3RC and Coulson for $\tau = 1$ and $\mu = 0.02$.

As in all envelope analysis performed on the I3RC-POL, U values and a minimum uncertainty have been achieved when the magnitude of the photons sampled reached 10^8. In some optical depth and viewing zenith angle combinations, the U values and standard error may have converged even sooner. When the optical depth is equal to 1, as seen in figures 6.25 and 6.27, there is very little variation in U values even before 10^8 photons. This can also be seen for when $\tau = 0.02$ and $\mu = 0.02$ (Figure 6.24). Again when the optical depth is thin, slight more variation in U values occur when the cosine of the viewing zenith angle approaches 1 as the number of photons necessary to resolve expected values jumps to $6 * 10^8$ photons (Figure 6.26). It is our recommendation in this case to use $6 * 10^8$ photons to insure accurate results with an uncertainty magnitude of 10^{-7}.

Envelope comparison to the expected Coulson results have shown that although I3RC-POL does not converge to the exact expected U values, often the magnitude in this difference is very small. This becomes very apparent when $\mu = 1$. In the case of $\tau = 0.02$ as seen in Figure 6.26, I3RC-POL's enveloped is very close to Coulson's value. Although the difference in value is very small about 10^{-6}, the error can not be attributed to expected Monte Carlo noise. When the optical depth increases, the magnitude in this error increases. When $\tau = 1$

and $\mu = 1$ (Figure 6.27), I3RC-POL's envelope again does not include Coulson's expected results with errors about 10^{-3}. In both figures 6.26 and 6.27, all azimuth angles resolved to the same U value which again is consistent with expected results.

Carefully analyzing the envelope benchmark comparison when $\mu = 0.02$, U values exhibit some of the similar behavior seen in previous testing. Both figures 6.26 and 6.27 do not have U values that resolve to Coulson's expected values. When $\tau = 0.02$ this error's magnitude is quite small, 0^{-4}, but as the optical depth increase to $\tau = 1$ the error increases to a magnitude of 10^{-2}. This direct relationship between error and optical depth increasing again can not be attributed to expected Monte Carlo uncertainty due to the standard error's small value and the lack of envelope convergence. Also examining Figure 6.30 and 6.31, the influence of viewing azimuth angle on U results can again be seen. Where as intensity results had a clear pattern and relationship in difference in results due to viewing azimuth angle, this relationship in U results are not as clear using envelope testing. In both $\tau = 0.02$ and $\tau = 1$, U results using a viewing azimuth angle $\phi = 180^\circ$ appears to have the largest error. Additional azimuthal relationships may be better analyzed using the viewing zenith angle testing seen in the following section.

Viewing Zenith Angle

Examining the viewing zenith angle testing, the pattern in U result's dependency on viewing azimuth angle becomes more apparent. As in all simulations performed in I3RC-POL benchmarking, calculations were completed again for the optical depths of $\tau = 0.02$ and $\tau = 1$ for a range of different μ values for $\mu_0 = 1$. The number of photons simulated were $9.6 * 10^8$ which in turn produced an uncertainty with a magnitude of 10^{-7}.

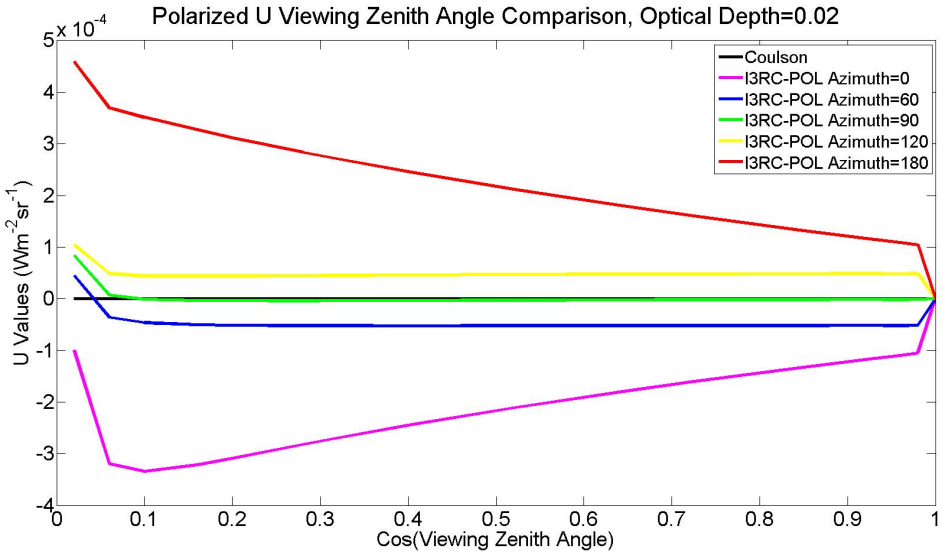

Figure 6.28: Polarized U view angle comparison between the I3RC-POL and Coulson for an optical depth of $\tau = 0.02$ and $\mu_0 = 1$.

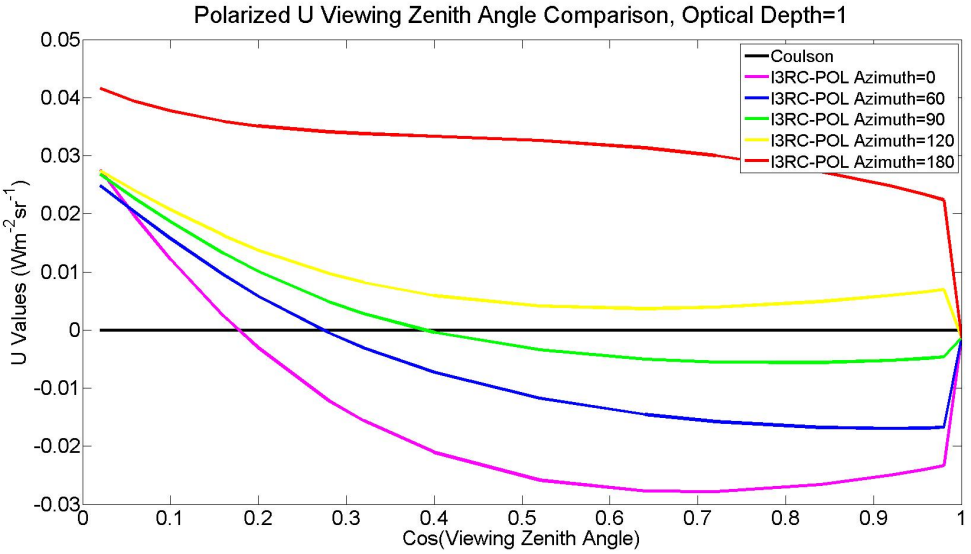

Figure 6.29: Polarized U view angle comparison between I3RC and I3RC-POL for an optical depth of $\tau = 1$ and $\mu_0 = 1$.

When analyzing U results for $\tau = 0.02$ and $\mu_0 = 1$ (Figure 6.28), the same dependency on viewing azimuth angle becomes apparent. The viewing azimuth angle pairs of ($\phi = 0°$ and $\phi = 180°$) and ($\phi = 60°$ and $\phi = 120°$) have the same magnitude but different signs in U results. Where $\phi = 0°$ is producing negative U values, the corresponding viewing azimuth angle of $\phi = 180°$ calculates positive U values. This behavior is also seen in the viewing

azimuth pair ($\phi = 60°$ and $\phi = 120°$) and finally $\phi = 190°$ calculates U values very similar to Coulson's results of 0. Adding sign information to the consistent relationship between azimuth angles over all polarized testing may add an extra clue that can help to resolve the bug within the I3RC-POL.

There is additional odd behavior in I3RC-POL results over all viewing azimuth angles. When $\tau - 0.02$, there is a large spike in U values between $\mu = 0$ and $\mu = 0.1$ over all viewing azimuth angles regardless. Another spike is seen when μ approaches 1, but in this case the values rapidly approach the expected value of U. While this behavior can be seen in most U values, when $\phi = 90$ this spike is not present because it's U results are mostly consistent with Coulson's expected value. There is currently no physical explanation of why this occurring but hopefully resolving the error within the I3RC-POL may address this issue.

Finally examining a $\tau = 1$ figure 6.29, the same consistent behavior can again be seen. The viewing azimuth angle pair of $\phi = 0°$ and $\phi = 180°$ have the largest error compared to expected Coulson results of zero. Next the viewing azimuth angle pair of $\phi = 60°$ and $\phi = 120°$ result in a smaller error of U results. Finally, the viewing azimuth angle of $\phi = 90$ calculates U values most similar to Coulson's U value of zero. As in the $\tau = 0.02$ results, when μ approaches 1, there is a rapid convergence to Coulson's values over all I3RC-POL outputs. A unique behavior in these results include the shape of I3RC-POL results. U results initially are largest when $\mu = 1$ and then slope down to a certain value until they spike towards the expected result of zero. This shape though is not consistent over all I3RC-POL outputs. When $\phi = 0°$ the U results decreases more rapidly which can be seen on figure 6.29 as the line corresponding to this azimuth angle crosses different I3RC-POL U values. Also, when $\phi = 180°$, the shape is not consistent to the other outputs as it does not curve to smaller values in the same manner. Additionally when calculating U values using viewing azimuth angles of $\phi = 0°, 60°, \text{and } 90°$, the results change signs. Although a physical explanation has yet to be examined, this odd behavior must be better understood.

6.4.4 V Comparison

Normally the same three benchmarking tests would be performed on the V component of the Stokes vector. This is not necessary though because Coulson's tabulated results in these calculations are all equal to zero. I3RC-POL V values were equivalent to zero over all viewing angles when the solar mu μ_0. Since the value's were zero, no additional tests were needed performed.

Chapter 7

Conclusions

7.1 Model Validity

Although the I3RC-POL's unpolarized results are able to replicate the original I3RC's unpolarized results within 1% percent error, there appears to be an error outside the expected uncertainty. This difference can be seen when the cosine of the viewing angle (μ) becomes more oblique. In these cases, the I3RC-POL fails to converge to the expected results. Also, when the optical depth is increased the error also increases suggesting there must be a compounding of error over scattering events. Although, this error only produces a percent error of less than 1%, it is still present in all unpolarized and polarized results. The current hypothesis is that by fixing the unpolarized bug, much of the error seen in the polarized benchmarking tests will also be resolved.

The same error seen in I3RC-POL's unpolarized results are also present if not amplified in all polarized benchmarking comparisons. Again, an error larger than the Monte Carlo noise is seen when the viewing zenith angle is more oblique and the optical depth is thicker. Not only does the percent error range up to 3% for an optical depth of $\tau = 1$, the physical process also appear to have problems. When $\mu_0 = 1$, the viewing azimuth angle should not influence intensity results, yet there is a variation in intensity values over different azimuth angles. A specific pattern in the variance due to azimuth angle has been found and is

directly related to an additional cosine term. Additionally, the I3RC-POL struggles with the polarized components of the Stokes vector. Q value signs and magnitude were often large than expected results while the I3RC-POL produced nonzero U values which is not consistent to Coulson's findings. Prior to any use or additional benchmarking of the I3RC-POL, these errors must be resolved.

7.2 Possible Cosine Error Sources

One of the possible sources for this key additional cosine function is due to the development strategy of the I3RC-POL. Much of the model's development concerned the derivation of the rotation angles for the phase matrix. As seen in Section 2.3.2, these rotation angles are derived in terms of cosine. Originally when creating the I3RC-POL, the initial method was to keep these cosines in tack to reduce error that may occur when using inverse trigonometric functions. In doing so, as many angles as possible were forced to be defined in terms of a cosine function. This coding strategy must be the source of the additional cosine value.

More specifically, this cosine may be found within the rejection method. As discussed in Chapter 5, the way in which the new scattering angles are selected is altered, specifically the rotation angle is selected using the rejection method. Within this subroutine, the new resulting azimuth angle was set in terms of a cosine, yet this is not consistent with how the azimuth angle should be defined. Since the error is seen in both unpolarized and polarized results, the location of this error must be in a portion of the code that is used no matter the polarization. The rejection method is a used in both cases adding to the strength of this theory.

7.3 Possible Phase Matrix Errors

In addition, careful consideration of possible polarized errors must also be considered in order to solve the errors in the Stokes vector. The phase matrix provides one of the most important changes regarding polarized radiative transfer calculations. When examining the errors that the I3RC-POL produces, it is clear that there is a strong angular influence. Since the phase matrix is very dependent on angle combinations, this may be one of the sources of error. Also the phase matrix contributes to both intensity and polarized components of the Stokes vector. Since there are apparent problems in these quantities, examination of possible phase matrix errors is necessary.

7.3.1 Reference Frame

Prior to even considering the phase matrix, it is necessary to understand the orientation of the model. The I3RC-POL uses the coordinate system described in Section 4.1.3. This is not always the case though as different literature can describes the scattering matrix using an alternative coordinate system definition. For example, the orientation in Hovenier's description of the scattering matrix has opposite signs for μ and ϕ (*Hovenier*, 1969). This coordinate system may change the sign of scattering matrix elements which can contribute to differences in Q and U results. The treatment of the scattering matrix within an alternative reference frame became the most apparent confusion while benchmarking the I3RC-POL. When trying to debug the model, this is the most important place to start.

7.3.2 Phase Matrix Symmetries

Certain azimuth and zenith angle combinations may also change the sign of some of the elements of the phase matrix. Hovenier explores this by examining how the phase matrix changes when the incoming or outgoing angles are interchanged and how changing the sign of μ will also alter the phase matrix values (*Hovenier*, 1969). Using eight different combi-

nations, Hovenier was able to fully describe these scenarios. Since interchanging ϕ and ϕ', μ and μ', and changing the signs of μ and μ' are all possible within the I3RC-POL, these additional changes to the phase matrix must be considered. Currently this paper's findings are not implemented with the I3RC-POL. This may cause the phase matrix to be wrong in some scattering combinations. Considering there tends to be an angular dependent error within the I3RC-POL, implementations of this paper's finding may help to produce better phase matrix values and thus better overall outputs.

7.3.3 Rotation Matrix

The rotation matrices also have a strong angular dependence. Since the apparent problems within the I3RC-POL appear to be dependent on angles, determine the validity of the rotation matrix is crucial. There are several different aspects of the rotation matrix that must be considered: reference frame, direction of rotation, and the sign of the angle of rotation. Current implementation of the I3RC-POL rotates the Stokes vector in the clockwise direction while alternatively, the Stokes vector may be rotated in the opposite counterclockwise direction. Either type of rotation can be selected, but the rotation angles must reflect this direction. Combining the wrong sign of the rotation angle with the wrong direction of rotation matrices may produce values of the scattering matrix that are incorrect. The literature has such a wide array of combinations between reference frame, rotation matrix, and rotation angle that it often difficult to keep track of the correct approach. The inconsistency of the literature provided a large gap of understanding when implementing polarization within the original I3RC. Due to the lack of confidence within this portion, it is suggested that this possible error could very well be present within the I3RC-POL.

7.4 Normalization Within ComputeRT

The treatment of the Stokes vector and phase matrix is very important within the I3RC-POL. Within the model, the subroutine *computeRT* scatters and moves the photon while the subroutine *computeIntensityContributions* supplies the contributions as if an imaginary photon traveling into the specified intensity direction. One subroutine uses the real photon another treats it as imaginary; thus the treatment of the Stokes vector within these two subroutines are different. Concentrating on *computeRT*, the Stokes vector must be kept consistent between each scattering event. The only decrease in value occurs due to absorption, not scattering. This may also be seen in the original I3RC.

During the unpolarized simulations, this process was represented by normalizing the phase matrix by the $P_{11}(\Theta)$ value. If this normalization wasn't considered, I3RC-POL intensity values were thirteen thousand times the values calculated by the original I3RC. Examining how the original I3RC approached the physical scattering of each photon within the *computeRT* subroutine, it became apparent that this lack of normalization in I3RC-POL was adding an additional $P_{11}(\Theta)$ value at each scattering event. This error compounded over each scattering event and each photon resulting in excessively large intensity values. When the phase matrix was divided by $P_{11}(\Theta)$, the current unpolarized results were achieved.

Examining outputs of the I3RC-POL within the *computeRT subroutine*, it become apparent that the intensity component of the Stokes vector was equal to a wide range of numbers. Keep in mind that within the original I3RC, there was no such change in photon weight which may represent intensity due to scattering. Therefore, the I3RC-POL is adding an additional modification to the intensity component of the Stokes vector. This intensity component is defined as:

$$I = Z_{11}I' + Z_{12}Q' + Z_{12}U' + Z_{14}V' \tag{7.1}$$

Not only do the elements of the phase matrix influence the value of I but also the addi-

tional components of the Stokes vector may have an impact on intensity. When normalizing the phase matrix, the Z_{11} component becomes 1, but all the additional components still have contributing values. When using the unpolarized environment, normalizing the scattering phase matrix also made $Z_{11} = 1$ making the values with the *computeRT* consistent to the original I3RC so this normalization appeared correct. In order to represent this process in the polarized version of the I3RC, different normalization schemes should be considered. For example, dividing the Stokes vector by I within *computeRT* could be an alternative normalization for this problem. It would allow the scattered Stokes vector to have an I component of 1 which could keep intensities consistent, while Q, U, and V would represent a ratio of those components. Further exploration is necessary for this problem.

Chapter 8

Future Work

There is still a large amount of work to complete prior to the completion I3RC-POL. Once the possible corrections stated in Chapter 7 are completed, the I3RC-POL must be fully benchmarked. From there, the I3RC-POL may be used for analysis and simulations. There are also several extensions to the I3RC-POL that users may find advantageous.

8.1 Additional Benchmarking

8.1.1 Coulson Polarized Benchmarking

Similar to most polarized radiative transfer codes, benchmark work began with the analytical solutions provided by Coulson (1960). Intensity, Q values, and U values have been considered primarily in the solar nadir direction. There are a wide range of additional solar zenith angle values within Coulson that may be used for benchmarking. Additionally, these alternative solar zenith angle values provide more dependence on azimuth angle. Using benchmark results of these tables may be useful when making corrections specified in the Chapter 7.

8.1.2 Extended 1D Polarized Benchmarking

Coulson's main limitation is the small range of optical depths calculated and the use of only Rayleigh scattering. While Coulson's tabulated results provide an ideal initial benchmark,

testing the I3RC-POL's ability to handle more complex simulations, even if they are one dimensional, is necessary to determine its validity. Additional benchmarking can include simulations to explore validity in larger optical depths, more pixels within the domain, with multiple types of particles, and Mie scattering scenarios. In order to determine the validity of these simulations, identical simulations must be performed on alternative polarized plane parallel radiative transfer models (*Kokhanovsky et al.*, 2009). An additional benchmarking test that can be performed is the reciprocity technique.

8.1.3 Three Dimensional Benchmarking

Finally, benchmarking needs to be completed in three dimensional cases. Complex domains must be simulated using a wide range of cloud fields and aerosols. Not only would this evaluate the I3RC-POL's ability to simulate three dimensional radiative transfer calculations but it also checks how the model can handle different particle characteristics, more computationally expensive calculations, and overall model efficiency. This method may be somewhat difficult due to the lack of available three dimensional models yet it is vital to benchmark the I3RC-POL. Options to validate three dimensional results include the reciprocity technique and the collaboration of different model results similar to the original I3RC (*Cahalan et al.*, 2005). The types of simulations can be endless and this process will help set up the I3RC-POL's ability to handle different scientific questions.

8.2 Model Extensions

8.2.1 Phase Matrix Representation

Currently, the scattering phase matrix portion of the phase matrix is represented as a set of tabulated values. An alternative representation, not yet implemented within I3RC-POL, is the legendre coefficient version of the scattering phase matrix. This additional represen-

tation may be useful to Mie scattering simulations. This extension of a legendre coefficient scattering phase matrix would require modification of only the scattering phase matrix module. The original phase function has the option of being represented by legendre coefficients and this base code is already present in the *scatteringPhaseFunction* module. Using this as a base, the extension to a legendre coefficient phase matrix would be relatively straightforward to implement and useful.

8.2.2 Full Scattering Phase Matrix

The assumption that all particles within I3RC are spherical and randomly oriented allows for the phase matrix to be simplified. Instead of 16 unique elements of the scattering phase matrix, the I3RC-POL uses eight non-zero elements in which only four are unique. While this assumption is useful in many scenarios, it is not applicable to all complex environments include nonrandom orientation and non spherical particles. In order to represent every possible scattering scenario, the scattering phase matrix must be extended to 16 unique elements. This may be done by altering the I3CR-POL by extending the phase function object within the *scatteringPhaseFunction* module. This would also require changes to any subroutine or function that calls the scattering phase matrix within the integrator. Finally, the user would have to change how they set their scattering phase matrix within the domain creation. Although this addition requires a substantial amount of change, the implementation would not be very difficult and very advantageous to users requiring a complicated scattering phase matrix.

8.2.3 Extended Surface Representation

Currently, the I3RC-POL's surface is represented solely as a Lambertain surface. In the benchmarking so far, the surface albedo is equal to one limiting any interaction with the surface. This representation may be an over simplification for much of the surface's modeled.

There are a number of alternative representations that will provide more realistic environments. This may include but is not limited to BRDF values for each surface, ocean surfaces, topography, and fully polarized surfaces again using the BRDF method (*Flynn and Alexander*, 1995). Extending the I3RC-POL to also include a wide range of surfaces can help to provide more accurate calculations.

References

Alexandrov, M. D., B. Cairns, C. Emde, A. S. Ackerman, and B. van Diedenhoven (2012), Accuracy assessments of cloud droplet size retrievals from polarized reflectance measurements by the research scanning polarimeter, *Remote Sensing of Environment*, *125*, 92–111.

Barker, H., R. Goldstein, and D. Stevens (2003), Monte carlo simulation of solar reflectances for cloudy atmospheres, *Journal of the atmospheric sciences*, *60*(16), 1881–1894.

Bony, S., and J.-L. Dufresne (2005), Marine boundary layer clouds at the heart of tropical cloud feedback uncertainties in climate models, *Geophysical Research Letters*, *32*(20).

Bony, S., et al. (2006), How well do we understand and evaluate climate change feedback processes?, *Journal of Climate*, *19*(15).

Boucher, O., et al. (2013), *2013: Clouds and Aerosols. In: Climate Change 2013: The Physical Science Basis. Contribution of Working Group I to the Fifth Assessment Report of the Clouds and Aerosols. In: Climate Change 2013: The Physical Science Basis. Contribution of Working Group I to the Fifth Assessment Report of the Intergovernmental Panel on Climate Change*, Cambridge University Press, Cambridge, United Kingdom and New York, NY, USA.

Bréon, F.-M., and P. Goloub (1998), Cloud droplet effective radius from spaceborne polarization measurements, *Geophysical research letters*, *25*(11), 1879–1882.

Cahalan, R. F., et al. (2005), The i3rc: Bringing together the most advanced radiative transfer tools for cloudy atmospheres., *Bulletin of the American Meteorological Society*, *86*(9).

Chandrasekhar, S. (1960), *Radiative transfer*, Dover Publications, New York.

Cornet, C., et al. (2010), Three-dimensional polarized monte carlo atmospheric radiative transfer model (3dmcpol): 3d effects on polarized visible reflectances of a cirrus cloud, *Journal of Quantitative Spectroscopy and Radiative Transfer*, *111*(1), 174–186.

Coulson, K. L., J. V. Dave, and Z. Sckera (1960), Tables related to radiation emerging from a planetary atmosphere with rayleigh scattering.

Deschamps, P.-Y., F.-M. Bréon, M. Leroy, A. Podaire, A. Bricaud, J.-C. Buriez, and G. Seze (1994), The polder mission: Instrument characteristics and scientific objectives, *Geoscience and Remote Sensing, IEEE Transactions on*, *32*(3), 598–615.

Deuzé, J., F. Bréon, P. Deschamps, C. Devaux, M. Herman, A. Podaire, and J. Roujean (1993), Analysis of the polder (polarization and directionality of earth's reflectances) airborne instrument observations over land surfaces, *Remote sensing of environment*, *45*(2), 137–154.

Di Girolamo, L., T. Várnai, and R. Davies (1998), Apparent breakdown of reciprocity in reflected solar radiances, *Journal of Geophysical Research: Atmospheres (1984–2012)*, *103*(D8), 8795–8803.

Di Girolamo, L., L. Liang, and S. Platnick (2010), A global view of one-dimensional solar radiative transfer through oceanic water clouds, *Geophysical Research Letters*, *37*(18).

Diner, D., et al. (2013), The airborne multiangle spectropolarimetric imager (airmspi): a new tool for aerosol and cloud remote sensing., *Atmospheric Measurement Techniques Discussions*, *6*(1).

Diner, D. J., et al. (1998), Multi-angle imaging spectroradiometer (misr) instrument description and experiment overview, *Geoscience and Remote Sensing, IEEE Transactions on*, *36*(4), 1072–1087.

Emde, C., R. Buras, B. Mayer, and M. Blumthaler (2010), The impact of aerosols on polarized sky radiance: model development, validation, and applications, *Atmospheric Chemistry and Physics*, *10*(2), 383–396.

Evans, K., and G. Stephens (1991), A new polarized atmospheric radiative transfer model, *Journal of Quantitative Spectroscopy and Radiative Transfer*, *46*(5), 413–423.

Evans, K. F., and G. L. Stephens (1990), Polarized radiative transfer modeling: an application to microwave remote sensing of precipitation, Master's thesis, Colorado State University.

Flynn, D. S., and C. Alexander (1995), Polarized surface scattering expressed in terms of a bidirectional reflectance distribution function matrix, *Optical engineering*, *34*(6), 1646–1650.

Girolamo, L. D. (2002), Reciprocity principle for radiative transfer models that use periodic boundary conditions, *Journal of Quantitative Spectroscopy and Radiative Transfer*, *73*(1), 23–27.

Hall, L. (2013), Space technology roadmaps: The future brought to you by nasa, *image*.

Hovenier, J. (1969), Symmetry relationships for scattering of polarized light in a slab of randomly oriented particles, *Journal of the Atmospheric Sciences*, *26*(3), 488–499.

Hovenier, J., and C. Van der Mee (1983), Fundamental relationships relevant to the transfer of polarized light in a scattering atmosphere, *Astronomy and Astrophysics*, *128*, 1–16.

IPCC (2007), *IPCC, 2007: Climate Change 2007: The Physical Science Basis. Contribution of Working Group I to the Fourth Assessment Report of the Intergovernmental Panel on Climate Change*, Cambridge University Press, Cambridge, United Kingdom and New York, NY, USA.

Justice, C. O., et al. (1998), The moderate resolution imaging spectroradiometer (modis): Land remote sensing for global change research, *Geoscience and Remote Sensing, IEEE Transactions on*, *36*(4), 1228–1249.

Kokhanovsky, A. A., et al. (2009), Benchmark results in vector radiative transfer, *Quant Spectrosc Ra., doi*, *10*.

Liou, K.-N. (2002), *An introduction to atmospheric radiation*, vol. 84, Academic press.

Marchuk, G. I., G. A. Mikhailov, R. A. Darbinjan, B. S. Elepov, M. A. Nazaraliev, and B. A. Kargin (1980), *The Monte Carlo methods in atmospheric optics*, Springer.

Marshak, A., S. Platnick, T. Várnai, G. Wen, and R. F. Cahalan (2006), Impact of three-dimensional radiative effects on satellite retrievals of cloud droplet sizes, *Journal of Geophysical Research: Atmospheres (1984–2012)*, *111*(D9).

Mayer, B. (2009), Radiative transfer in the cloudy atmosphere, in *EPJ Web of Conferences*, vol. 1, pp. 75–99, EDP Sciences.

Mayer, B., , and A. Kylling (2005), Technical note: The libradtran software package for radiative transfer calculations-description and examples of use, *Atmospheric Chemistry and Physics*, *5*(7), 1855–1877.

Mayer, B., A. Kylling, C. Emde, U. Hamann, and R. Buras (2011), libradtran user's guide.

McMaster, W. H. (1961), Matrix representation of polarization, *Reviews of Modern Physics*, *33*(1), 8–27.

Min, Q., et al. (2010), A polarized radiative transfer model based on successive order of scattering, *Advances in Atmospheric Sciences*, *27*(4), 891–900.

Mishchenko, M. I., L. D. Travis, and A. A. Lacis (2002), *Scattering, absorption, and emission of light by small particles*, Cambridge university press.

Myhre, G., C. Myhre, B. Samset, and T. Storelvmo (2013), Aerosols and their relation to global climate and climate sensitivity, *Nature Education Knowledge*, *4*(5), 7.

National Research Council (US), C. o. E. S., A. from Space, R. A. Anthes, and B. Moore (2007), *Earth science and applications from space: National imperatives for the next decade and beyond*, National Academies Press.

Natraj, V., K.-F. Li, and Y. L. Yung (2009), Rayleigh scattering in planetary atmospheres: corrected tables through accurate computation of x and y functions, *The Astrophysical Journal*, *691*(2), 1909.

Ohring, G., B. Wielicki, R. Spencer, B. Emery, and R. Datla (2005), Satellite instrument calibration for measuring global climate change: Report of a workshop., b. am. meteorol. soc., 86, 1303–1313, doi: 10.1175, *Tech. rep.*, BAMS-86-9-1303.

Pincus, R. (2009), *Programmer's Guide to the I3RC Community Radiative Transfer Model*.

Pincus, R., and K. F. Evans (2009), Computational cost and accuracy in calculating three-dimensional radiative transfer: Results for new implementations of monte carlo and shdom., *Journal of the Atmospheric Sciences*, *66*(10).

Rozanov, V., A. Rozanov, A. Kokhanovsky, and J. Burrows (2014), Radiative transfer through terrestrial atmosphere and ocean: software package sciatran, *Journal of Quantitative Spectroscopy and Radiative Transfer*, *133*, 13–71.

Twomey, S. (1977), The influence of pollution on the shortwave albedo of clouds, *Journal of the atmospheric sciences*, *34*(7), 1149–1152.

Tynes, H. H., G. W. Kattawar, E. P. Zege, I. L. Katsev, A. S. Prikhach, and L. I. Chaikovskaya (2001), Monte carlo and multicomponent approximation methods for vector radiative transfer by use of effective mueller matrix calculations, *Applied Optics*, *40*(3), 400–412.

Van de Hulst, H. (1957), Scattering of light by small particles, *Moscow: Izd-vo inostr. lit. l96l*.